Auckland University of Technology

Masters (Thesis)

Analysis and Optimization of the AUT 30-metre Radio Telescope: Pointing and Surface

Author:

Asif R Rasha

Supervisors:

Tim Natusch

Prof. Sergei Gulyaev

School of Engineering, Computer and Mathematical Sciences

January 2017

Abstract

The purpose of this research is to analyze, evaluate and improve the current pointing performance of AUT's 30-metre radio telescope. The telescope currently uses the "fivept" pointing procedure of the NASA Field System (used for scheduling and operation of the 30-metre) to collect pointing offsets. "pdplt", another program in the Field System, is used to process, generate and apply a pointing model to correct for errors in pointing. The Field System pointing model allows up to 30 terms to account for various pointing errors, of which 8 terms are currently being used.

Previous research had identified a sinusoidal pattern in the residual pointing offsets that significantly reduces pointing accuracy [1]. We develop an alternative pointing methodology that significantly improves the pointing accuracy by (a) applying a source selection method, (b) applying an outlier removal procedure and (c) using additional terms to remove the sinusoidal pattern. The "fivept" pointing procedure is used to build the pointing database. A script written in Bash is used to preprocess the offsets and the R programming language is used to process, analyze and evaluate new pointing models. Three new terms are added to the existing model that effectively suppress the sinusoidal pattern. The end result improves the pointing accuracy significantly, with the RF axis being able to point within an error ellipse that is smaller than 10% of the FWHM.

We speculate about possible reasons for the origin of the sinusoidal pattern of the pointing offsets. A major speculation was gravitational deformation in Elevation of the primary reflector surface. We use the laser scanning method to study the surface of the primary reflector. A FARO Laser scanner is used for collecting data. SCENE, an industry standard program and Matlab are used for processing and analyzing the data. We conclude that the main reflector has a good quality of surface with rms of ~ 3 mm, and does not demonstrate any noticeable gravitational deformation when studied at different Elevation angles.

Acknowledgements

First and foremost, thanks to my supervisors Tim Natusch and Sergei Gulyaev for their invaluable help and guidance. Without their enduring patience, criticism and support, this thesis could not have been written.

Thanks to Jeremy Neilson from Synergy Positioning Systems Ltd for conducting the surface scan of the antenna and for lending the laptop for data processing. I also appreciate his help for introducing me to the FARO SCENE package.

Thanks to Stuart Weston for setting up the test Field System and providing me with additional information from time to time.

Last but not the least, thanks to my parents for supporting my studies, I would not be where I am without you.

Declaration of Authorship

"I hereby declare that this submission is my own work and that, to the best of my knowledge and belief, it contains no material previously published or written by another person (except where explicitly defined in the acknowledgements), nor materials which to a substantial extent has been submitted for the award of any other degree or diploma of a university or other institution of higher learning."

ASIF RAYHAN RASHA

Contents

List of Figures

List of Tables

Overview of Thesis Structure

The thesis has four chapters and three appendices. A summary of the content of each of the chapters including appendices are given below:

Chapter 1 (Introduction) starts with "A brief history of Astronomy", which was written to trace the road since the beginning of astronomy that eventually leads to my present day research. It puts a different perspective to my motivation for this research. We then briefly discuss and illustrate the causes of pointing inaccuracy and the use of pointing models to compensate and minimize pointing offsets. We explain the Gaussian nature of the telescope beam and describe the adverse affect of pointing errors in degrading the relative source intensity in relation to the Gaussian beam.

We then state the technical specification of the 30-metre antenna at Warkworth and briefly discuss the conversion process from a satellite antenna to a radio telescope. A previous study done on the accuracy of the primary reflector surface is discussed, along with the recent laser scanning done to investigate gravitational deformation of the primary reflector surface. We then explain the mathematical expressions used to compensate pointing errors. We finish the chapter by describing the current pointing procedure in NASA's Field System used by the 30-metre antenna.

Chapter 2 (30-metre telescope pointing) describes the tools and techniques used to process, analyze and evaluate the pointing model. The first section describes the pre-processing of the pointing offset log file using a script written in Bash. We then explain the new pointing procedure developed using the R programming language for processing, analyzing and applying a pointing model derived from the pointing data. Outlier removal and source selection methods for the pointing procedure are discussed. The new pointing procedure was rigorously tested using different pointing datasets. We conclude the chapter by discussing those results.

Chapter 3 (Analysis of the Surface Quality of the Main Reflector) starts by discussing the laser scanning process of the primary reflector's surface conducted by Synergy Positioning Systems limited. The discussion includes the techniques used for setting up and collecting data using the laser scanner, and cleaning the data using a point cloud processing software called SCENE. A program written in Matlab was then used to fit a theoretical surface to the point cloud and measure the surface accuracy in terms of rms of the residuals from the fitting. The process was repeated using surface scan data collected at different Elevations to search for gravitational deformation. No significant deformation was observed, we conclude the chapter by discussing those findings in detail.

Chapter 4 presents conclusions and summarizes the overall thesis and outlines the relevant works that can be undertaken in the future.

Appendices

Appendix A contains the commands used in the Field System to run pointing observations. It also includes a screenshot and explanation of the pointing log file and lists all the available terms in the Field System pointing model.

Appendix B contains additional plots related to the analysis in Chapter 2.

Appendix C contains the Bash and R code used for developing the new pointing procedure.

Chapter 1

Introduction

Astronomy is one of the oldest, or perhaps the oldest, amongst all natural sciences, with evidence of observations dating back to prehistoric times. The oldest observational record dates back to 30,000 BC, and comes from the engraved pattern of lines on animal bones used to keep track of the phases of the moon [2]. Our ancestors have looked up to the heavens, pondering about the motion of celestial objects and tried to relate it to natural phenomena such as rain, draught, seasons and tides. From spiritual salvation to daily living, astronomy played an essential role in early civilizations. Celestial objects were identified with gods, and calendars were set by the observation of the Sun and Moon. It was very important for agricultural societies, as harvesting was dependent on planting at the correct time of the year.

Figure 1.1: Astrolabe, an ancient navigation device, displayed at the Sharjah Maritime Museum. Astrolabes were used to identify stars, measure angles, find direction and tell time. [3]

Ancient astronomy was closely related to astrology and only separated a few centuries ago. Much of early astronomy was about timekeeping, and almost all civilizations since the Neolithic and Bronze Age could successfully apply mathematics to predict solar and lunar events. Apart from timekeeping, ancient Greeks, Chinese, Indians and later the Arabs contributed significantly to the growth of astronomy. Important quantities such as the radius of Earth were calculated by Greek philosopher Eratosthenes by observing the angles of shadows created at widely separated regions with high accuracy. Indian astronomer Aryabhatia (476-550 A.D) calculated many important astronomical quantities such as the periods of planets, instantaneous motion of the moon, and times of solar and lunar eclipses. Chinese astronomer Gan De (4th century B.C) compiled the first star catalogue, and Chinese astronomers also were the first to record a supernova in 185 A.D. The medieval Islamic world (8th to 13th Century) translated and revised many important works of astronomy by the Greeks, Chinese, Indians and other ancient civilizations, which otherwise would have been lost in time [4].

The first successful use of the telescope in the 17th century by Galileo started a new era in astronomy. Previously, Copernicus used geometric techniques to propose the heliocentric system which was later validated and expanded by Galileo and Johannes Kepler. The unification of physics and astronomy by Kepler (Kepler's Law of Planetary Motion) and Isaac Newton (Universal Law of Gravitation) followed after, laying many of the foundations of modern astronomy.

With the advent of spectroscopy (study of spectral lines) in the 20th century, astronomers began to successfully derive many chemical and physical properties of stars and galaxies such as their composition, mass and density. With the use of modern photography, fainter objects could be observed. Edwin Hubble (1889-1953) using previous observational data from Vesto Slipher and his own observations formulated Hubble's Law and played an important role in establishing the field of extragalactic astronomy. All of the developments mentioned so far were limited to optical astronomy.

The first astronomical observations at other wavelengths were made in 1931, when Karl Jansky accidentally discovered radio noise coming from the centre of the Milky Way while working at Bell Labs [5] . He was initially looking at potential sources of interference for transatlantic radio transmission using a purpose built antenna, but noticed that the signal was recurring and peaked every 23 hours 56 minutes, the exact length of one sidereal day. The discovery was later announced in 1933.

Scientists long before predicted that the Universe should be producing ultraviolet radiation, gamma rays and X-rays, however since these electromagnetic waves are blocked by the Earth's atmosphere, they were not detected until the advent of space technology. Currently, they are observed from space using satellite probes. Figure 1.2 shows the opacity of Earth's atmosphere to electromagnetic waves.

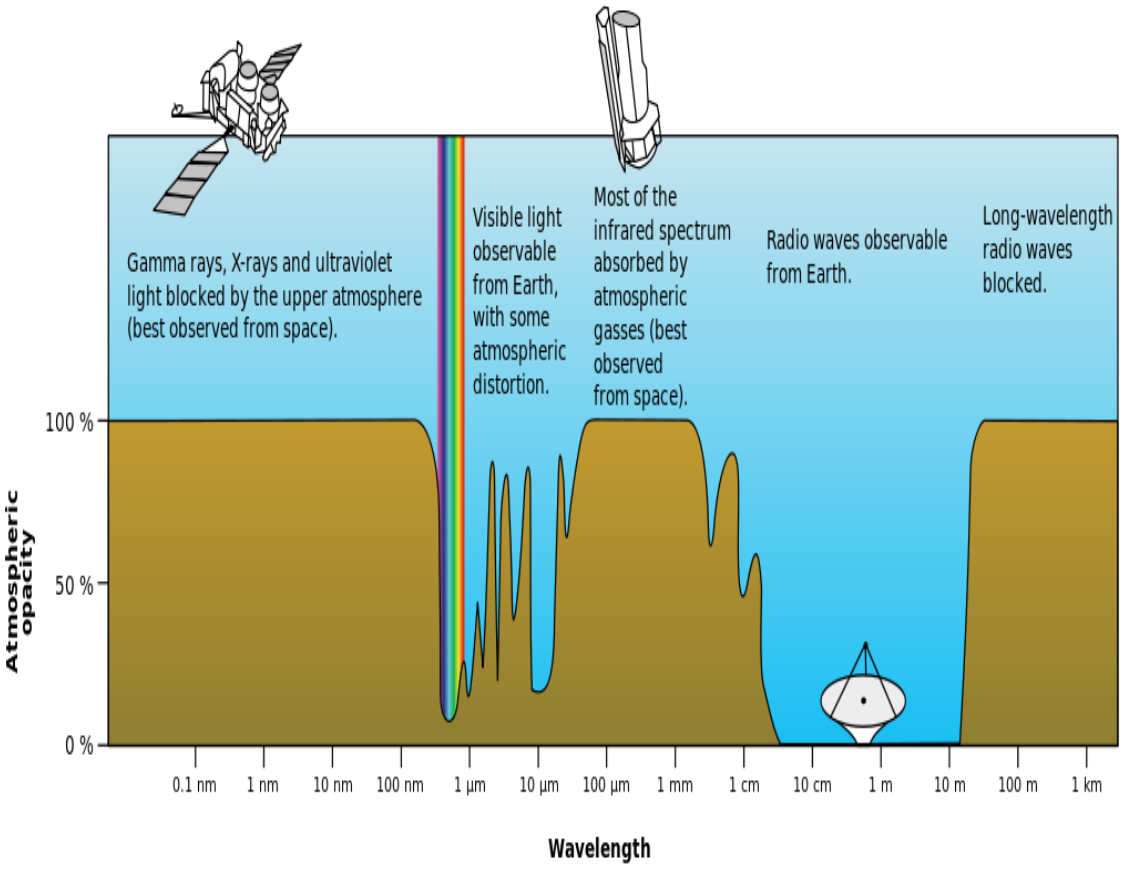

Figure 1.2: Earth's atmospheric opacity to electromagnetic waves – Gamma rays, UV and X-rays are blocked by Earth's ozone layer; therefore observations are carried out using satellite probes. [6]

As Figure 1.2 shows, radio waves have the least atmospheric attenuation compared to other EM waves. A wide bandwidth is available to ground based radio telescopes for observations, however low frequency transmission is limited by Earth's ionosphere, and water vapor significantly interferes at high frequency (over 30 GHz). Transmitting devices on Earth (cellphone, wireless internet technologies etc.) create interference as well, which is why radio telescopes are ideally built in remote locations.

Since angular resolution is a function of the diameter of the telescope and radio signals from space are extremely weak, radio telescopes are typically much larger than their optical counterparts. The practical limit on how large an individual telescope can be constructed led to the development of radio interferometry and the technique of aperture synthesis, where radio signals from a celestial source are collected and combined using a number of smaller radio telescopes. This virtually creates a combined telescope with resolving power equal to the spacing of the antennas furthest apart in the array.

The advancement in science, engineering and technology has resulted in extremely powerful and sophisticated telescopes. At the same time, many experimental approaches have been developed and applied to ensure accurate positioning and pointing of telescopes. The next section discusses the importance of accurate pointing and how it significantly affects observations. This thesis aims to develop a methodology for improving the pointing accuracy of the 30-metre radio telescope owned and operated by Auckland University of Technology.

1.1 Preface: Telescope Pointing

Accurate pointing and positioning has always been a major concern for radio telescopes, mainly due to their large structure. Telescopes always have pointing inaccuracy due to mechanical misalignment, surface deformation due to gravity (gravitational deformation onwards[1]), wind and thermal distortion, and always point slightly offset from the actual source. While pointing offsets due to wind are

unsystematic and little can be done about it, mathematical pointing models are used to compensate for systematic pointing inaccuracies. Currently AUT operates two radio telescopes of size 12 m and 30 m in diameter, located in Warkworth, New Zealand. Pointing errors are larger for the 30-metre Radio Telescope due to its larger mechanical structure and of greater importance due to its enhanced angular resolution. Angular resolution defines the ability of a telescope to resolve small details of a source and is given by the following expression:

$$Angular Resolution(\theta) = 1.22\frac{\lambda}{D} \tag{1.1}$$

Where λ is the observed wavelength of the source, D is the diameter of the dish and θ is in radians. The angular resolution of the 30-metre telescope at C-Band ($\sim$ 6.7 GHz) is 0.104° (6.3').

To observe a source, the antenna is instructed to point at a given coordinate known as the true coordinate. However, due to systematic and random pointing errors, the telescope will point slightly off the source, at the apparent coordinate. The difference in the coordinate (offset), can be defined by:

$$\text{offset} = \textit{True Coordinate - Apparent Coordinate}$$

A pointing model estimates the offset by taking account of the mechanical misalignment, gravitational deformation and other factors that contribute to the pointing inaccuracy. The offsets are then added to the apparent coordinate to point the telescope beam towards the true coordinate, as given in the above equation.

Electromagnetic radiation from a point source travelling through outer space will spread over an area by the time it arrives at the aperture of the telescope. The

[1]Surface deformation due to gravity could be temporary, permanent or both. Temporary deformation would occur due to mechanical stress induced by gravity that causes variable structural deformation as the telescope operates at different elevation angle. Permanent deformation could occur if a mechanism induces plastic creep of the material in the antenna. We speculate either or both may have affected the 30 m antenna and for simplicity, will use the term "gravitational deformation" throughout the report to refer to both temporary and permanent deformation.

response of the telescope aperture (or the imaging system in general) to this incoming radiation can be quantified by a PSF (point spread function), also known as the impulse response function. For radio telescopes, the response of the circular aperture to this impulse of radiation in the Fourier domain is expressed by the following 2D point spread function [7]:

$$PSF = \int\int A(x,y)e^{j(k_x x + k_y y)}dk_x dk_y \tag{1.2}$$

Where $A(x,y)$ is the aperture function. The response of the aperture to an arbitary source of radiation is a convolution of the telescope's beam (PSF) with the source's signal.

For a circular aperture (assumed to be uniform), the response is an Airy pattern in the image plane and can be given by the following Bessel function (τ-method):

$$J_n(x) = \frac{1}{2\pi}\int_{-\pi}^{\pi} e^{i(n\tau - xsin(\tau))}d\tau \tag{1.3}$$

where n represents the order of the Bessel function.

The intensity of the Airy pattern is given by the squared modulus of the Fourier transform of the circular aperture [9]:

$$I(\theta) = I_0\Big(\frac{2J_1(x)}{x}\Big)^2 \tag{1.4}$$

Where J_1 is the Bessel function of the first kind of order one, I_0 is the maximum intensity of the pattern at the disc centre. The Airy pattern includes relatively small amplitude outer ring(s) in respect to the main lobe. A conventional approach is to ignore the outer rings (side lobes) and approximate the main lobe with a Gaussian profile.

$$G(r) = Ae^{-ar^2} \tag{1.5}$$

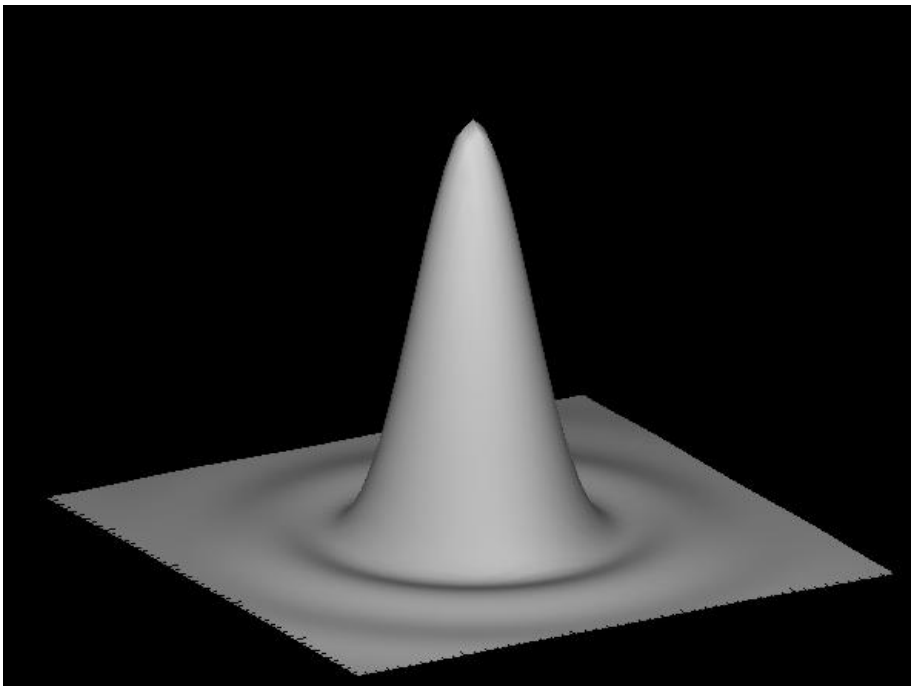

Figure 1.3: A computer plotted Airy pattern. The main lobe (beam in our case) contains the maximum power, with side rings (outer lobes) being observed [8].

where A is the amplitude of the Gaussian, r is the distance from the origin (in polar coordinates) and a is related to full width half maximum (FWHM) of the Gaussian. This is reasonable considering the side lobes have very small amplitude relative to the main lobe, and can easily get buried in the system noise.

Since the 2D Gaussian profile is rotationally symmetric, any radial slice of the Gaussian will have the same FWHM. Re-writing the equation in simple one dimensional form we have:

$$f(x) = ae^{\frac{(x-b)^2}{2c^2}} \tag{1.6}$$

Where a, b and c are the amplitude, mean and standard deviation of the function. The parameter c is also related to FWHM (FWHM = $2\sqrt{2ln2}$ c). In our research, we used c as the standard deviation.

Figure 1.4 shows a 13-point scan of Taurus A (in Elevation) using the 30-metre at 6.7 GHz. The x-axis represents the offsets (in degrees) and the y-axis represents

the relative intensity[2](r.i) of the source. As the telescope beam scans through the source in Elevation, signal intensity gradually increases to maximum (at the centre of the source), and then falls as the beam moves away. This results in an approximately Gaussian beam, and is modeled using the above Equation 1.6.

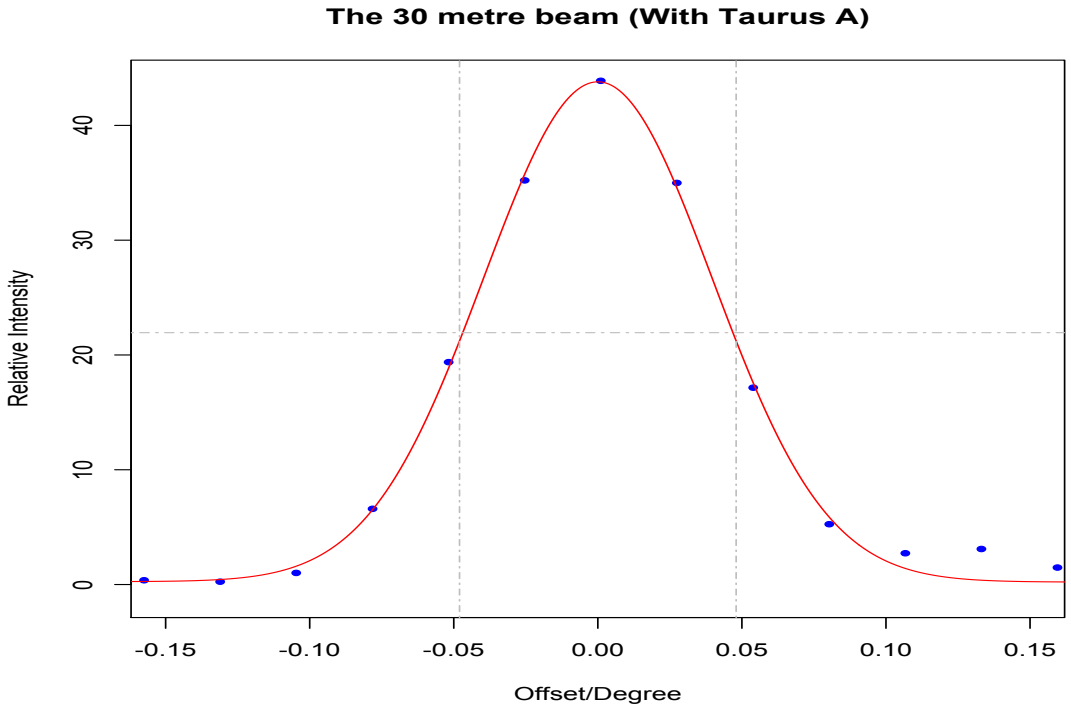

Figure 1.4: A 13-point Scan of Taurus A- The peak intensity (43.89 r.i) reduces to half of its initial value at 0.047°. So the FWHM is ∼0.047° × 2 = ∼0.094°. The dotted line in the x and y-axis shows the FWHM and the intensity at FWHM.

The angular resolution of the 30-metre antenna calculated previously using equation 1.1 was 0.104°. In Figure 1.4, the maximum relative intensity was 43.89 r.i. The angular resolution can be empirically calculated by taking the (FWHM) of the beam. The maximum relative intensity drops to half (21.94 r.i) at approximately 0.047°. So the FWHM is 0.047° × 2 =∼ 0.094°, close to the theoretically calculated beam (0.010°).

Table 1.1 is constructed using the fitting data used for the above Figure 1.4. The amplitude, mean and the sigma of the offsets were respectively 43.89, 0.025° and

[2]The 30-metre antenna is not equipped with a temperature calibration unit and therefore no absolute temperature or flux scale can be established. For further description, refer to page 18.

0.04°. Substituting the value of a, b and c in equation 1.6, and using offsets of 0.01°, 0.05° and 0.10°, the corresponding relative intensity were calculated (in Table 1.1). The intensity loss is calculated by taking the percentage difference of the relative intensity at every 0.05° (as in Table 1.1) with respect to the maximum value (the relative intensity at 0°).

Table 1.1: The following table shows how the relative intensity degrades with every 0.05 degrees of offset from the centre of the beam.

Offset (Degree)	**Relative Intensity**	**Intensity Loss(%)**
0.00	43.89	0.00
0.01	40.91	6.80
0.05	36.10	17.75
0.10	7.57	82.75

Table 1.1 gives a general idea as to why pointing accuracy is one of the most essential indicators for the performance of radio telescopes. As shown in Table 1.1, a typical offset of 0.1° can degrade the observation signal to noise by 82%. This will certainly be the case for observations where the observed source is smaller or the same size as the telescope beam. For observations where the source is larger than the telescope beam, the loss of signal to noise could be minimized with additional integration time. However, this in turn can reduce sensitivity to temporal variability and bury important information with the noise.

The offsets become more significant with bigger structures at higher frequency. Significant reduction of antenna sensitivity is to be expected if antenna pointing errors exceed 0.1 or 10% of the beam [10]. With the current receiver in the 30-metre telescope (C and X Band), the root mean square (rms onwards) of pointing offsets in C-Band and X-Band is ∼0.015° and ∼0.021°, roughly within 16% and 21% of the beam width [1]. This is significantly higher than the standard 10% of FWHM stated above.

Our research is concerned with the development of a tool/methodology for identifying causes of pointing error (for the 30-metre telescope) and use this to minimize the offset so the antenna RF-axis points within 10% of the FWHM, which is currently not the case.

1.2 The Warkworth 30-metre Radio Telescope

The Warkworth Radio Telescope was originally designed and built as a satellite communication dish in 1984 by NEC Corporation, Japan. It is a Cassegrain Alt-Azimuth mount antenna located in Warkworth, a small township 60 km north of Central Auckland. The New Zealand Post Office operated the satellite communication dish until 1987, before transferring it to Telecom NZ. It was used as a satellite communication dish until 2012, when the Institute of Radio Astronomy and Space Research (IRASR) acquired it for conversion to a radio telescope [11].

Figure 1.5: Warkworth 30-metre Radio Telescope

Significant work was involved in the conversion process which began in late 2012 and finished early 2014. The system had been cleaned, which required painting the structure, treatment of rust and replacing bolts. Old motors, cables, drives, control system and encoders were replaced to achieve desired mechanical performance [11].

The official "first light" took place in July 2014, observing a Methanol Maser at 6.7 GHz. Currently the telescope can operate in C-Band (6.7 GHz) and X-Band (8.2 GHz).

Table 1.2: Warkworth Telescope Specification according to the NEC manufacturers handbook. After the conversion, Azimuth working range is now ±270° relative to east\90°

Description	**Detail**
System	Alt-Azimuth, wheel-and-track, Cassagrain
Drive System	Electric-servo, dual train for antibacklash
Primary mirror diameter	30.48 m
Subreflector diameter	2.715 m
Transmission frequency band	C-Band
Reception frequency band	C-Band
Azimuth Maximum Speed	0.3 deg/sec or 18.0 deg/min
Elevation Maximum Speed	0.3 deg/sec or 18.0 deg/min
Azimuth Working Range (as defined by soft limits)	-170 to 170 deg
Elevation Working Range (as defined by soft limits)	0 to 90 deg
Surface accuracy (rms)	0.4 mm
Track diameter	16.97 m
Total Weight on track	268 tons
Wind speed in tracking operation	up to 40 m/s
Survive wind speed in stow position	up to 70 m/s

Synergy Positioning Systems Ltd conducted surface scans of the dish (at 6° Elevations) in late 2013 using a FARO laser scanner. Noticeable deformation was observed along the vertical cross-section of the main reflector [11]. The total rms of

the residuals at 6° Elevation was 3.5 mm, higher than stated in the manufacturer handbook (0.4 mm). Since the 30-metre was used for tracking geostationary satellites, it was speculated that constant tracking at a fixed Elevation over a period of 30 years may have caused a permanent deformation in the vertical cross-section.

In 2016, Synergy Positioning System repeated the surface scan, except this time the surface was scanned at increments of 10° between 10° and 90° Elevation. This was done to investigate whether there is any significant gravitational deformation of the surface depending on Elevation. The investigation was motivated by the speculation that the sinusoidal pattern observed in Elevation pointing offsets (discussed in Chapter 2) was due to gravitational deformation of the antenna surface. This investigation was also required to determine the feasibility of installing high frequency receivers in the future. Details about the surface analysis are discussed in Chapter 3.

1.3 Pointing Model: Glossary

Pointing offsets are mostly directed by instrumental flaws and are unique to individual telescopes, however most causes of pointing errors are common and will be present across all radio telescopes. The key systematic errors and the mathematical terms used to address them are discussed below. For further description refer to [4] & [10].

- **RF Collimation Error**: Ideally the RF beam should be orthogonal to the Elevation axis at 0° Elevation. However due to mechanical misalignment, there will be a slight tilt of the RF axis towards true Azimuth 90° at Elevation 0°. This offset (P_4) is called collimation Error. The offset is significant only in Azimuth and using spherical trigonometry (Figure 1.6), is given by the following term in Azimuth:

$$\Delta Az = -P_4 \sec(El) \tag{1.7}$$

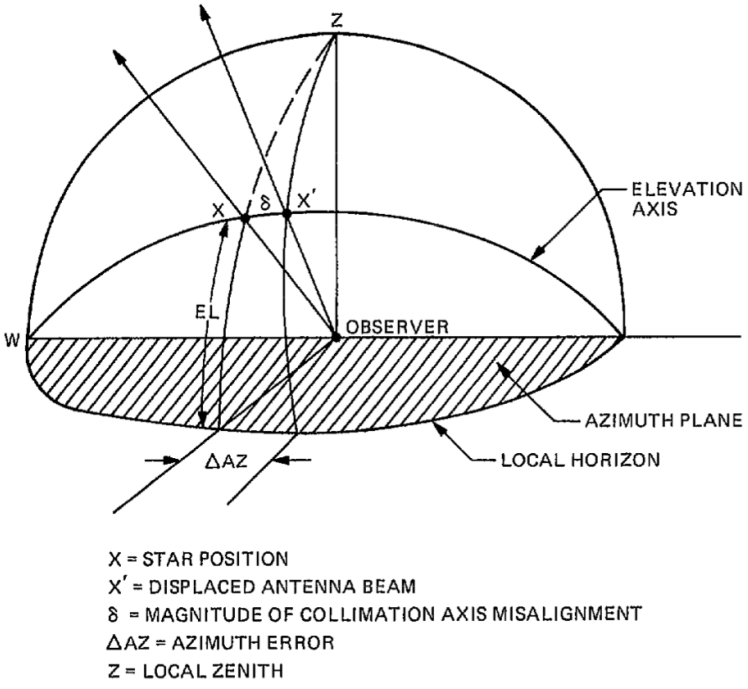

Figure 1.6: RF Collimation Error [10].

- **Encoder Fixed Offset:** The pointing offset due to the mechanical misalignment between the Azimuth encoder with the Azimuth axis and the Elevation encoder with the Elevation axis. The offsets are constant and independent of change in Azimuth and Elevation. Azimuth and Elevation encoder offsets are given by P_1 and P_7 respectively.

- **Axis Skew:** The pointing offset due to the nonorthogonality of the Elevation axis to the Azimuth axis. The Azimuth skew is very small and is neglected. The Elevation skew (P_3) affects Azimuth pointing and is given by the following term:

$$\Delta Az = P_3 \tan(El) \tag{1.8}$$

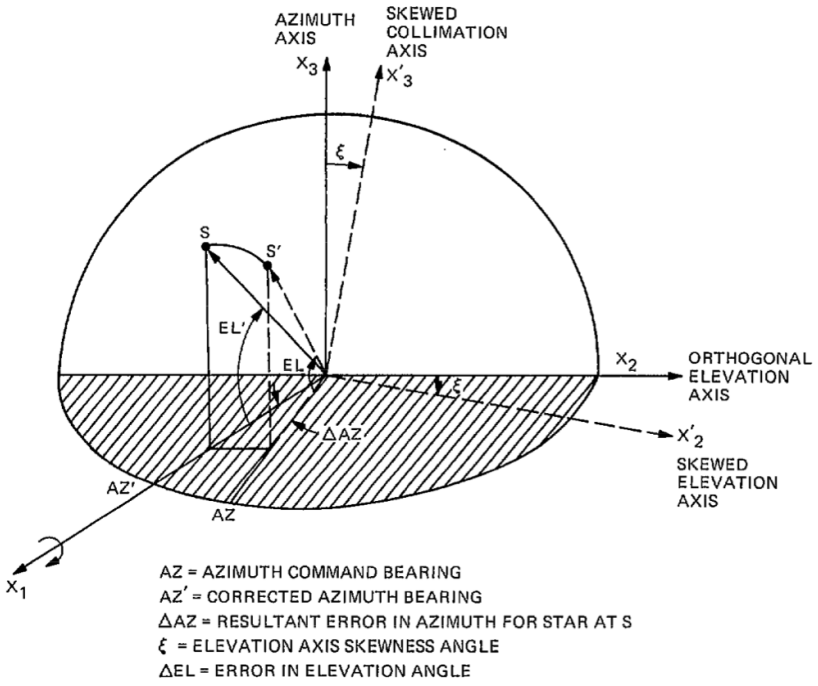

Figure 1.7: Elevation Axis Skew [10].

- **Azimuth Axis Tilt:** The pointing offset due to the deviation of the apparent Azimuth axis from the ideal Azimuth axis. The tilt affects pointing in both Azimuth and Elevation, and is given by the following terms in Azimuth:

$$\Delta Az = P_5 \sin(Az) \tan(El) - P_6 \cos(Az) \tan(El) \tag{1.9}$$

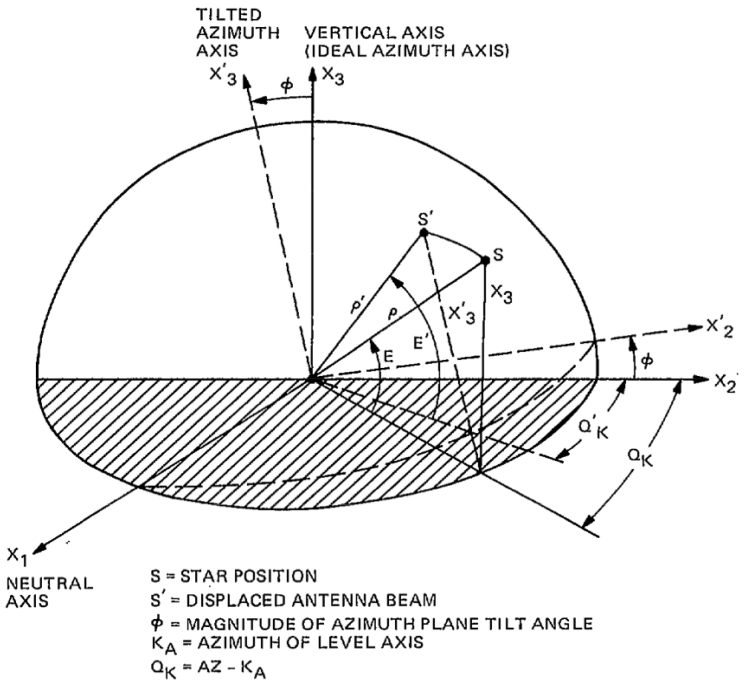

Figure 1.8: Azimuth Axis Tilt [10].

In Elevation:

$$\Delta El = P_5 \cos(Az) + P_6 \sin(Az) \tag{1.10}$$

- **Structural Flexure Due to Gravity:** Radio telescopes are susceptible to the effect of gravitational deformation due to their larger structure. Gravitational force exerts moments on the structure that are Elevation dependent, and thus changes the shape of the antenna at different Elevation angle. The effect of gravity on pointing (P_8) is compensated using the following term:

$$\Delta El = P_8 \cos(El) \tag{1.11}$$

- **Residual Error Due to Refraction:** Modern Radio Telescopes have refraction correction algorithms in the Antenna Control Sub-Assembly (ACS) that provides Elevation corrections based on humidity, pressure and temperature. The residual refraction error takes account of the pointing offset after the standard corrections are made by the refraction correction algorithm in the ACS, and is given by the following term:

$$\Delta El = P_{23} \cot(El) \tag{1.12}$$

Combining all the respective Azimuth and Elevation offsets from the equations above, we get the following pointing model:

$$\Delta Az = P_1 + P_3 \tan(El) - P_4 \sec(El) + P_5 \sin(Az) \tan(El) - P_6 \cos(Az) \tan(El) \quad (1.13)$$

$$\Delta El = P_5 \cos(Az) + P_6 \sin(Az) + P_7 + P_8 \cos(El) + P_{23} \cot(El) \quad (1.14)$$

Apart from the common errors described above, individual structures will have other systematic/random factors that affect pointing and are unique to the particular structure; those are generally corrected by analyzing pointing data and adding additional term(s) as necessary to the model. Currently AUT's 30-metre antenna uses the above model, although there is a sinusoidal pattern in Elevation pointing that cannot be removed using this current model. This is described in Chapter 2.

1.3.1 Field System and Pointing

The 12-metre and the 30-metre use the NASA Field System (FS onwards) for scheduling and controlling operations. The FS was developed in 1979 by NASA's Goddard Space Flight Center as a general platform for satellite tracking operations and provided a primitive programming environment with limited functionalities. However, the FS has significantly evolved over time and is now used by many Radio Observatories across the globe. It provides much functionality such as antenna pointing and gain calibration tools, semi-continuous system temperature monitoring, flagging, server functionality, remote and unattended operation, and many more [12]. For our research, we mostly used the antenna-pointing tool in the Field System.

The FS operator interface is based on the SNAP command/language (Standard Notation for Astronomical Procedures) and can be executed from the FS using a Unix shell. The SNAP commands used for the thesis are given in Appendix A.

The FS includes a program called “fivept” that builds a database of pointing offsets. “fivept” uses a procedure file “point.prc” that contains the pointing procedures/instructions along with the sources (including coordinates) to be observed for pointing. Currently, 16 sources are used for 30-metre antenna pointing, and are divided into Northern and Southern Hemisphere pointing sources in the proc file.

Once we initiate “fivept”, the following takes place [13]:

1. The first step is usually to measure the off source/background temperature using a noise diode. However, the 30-metre does not yet have a noise diode, so the diode noise temperature is manually set to a negative value in the relevant file. The absolute value of this is then taken as the system temperature by the pointing program and the antenna temperature due to the source is calculated based on this value. This procedure does not allow for absolute temperature flux/signal intensity to be established and as a consequence all further scan measurements are reported as "relative intensity".

2. The program then scans each source in both Azimuth and Elevation and continues until the program is stopped. The number of points/measurements, the integration period on each point and the size of the steps are specified in the “pointing.prc” file. For our research, we did a number of pointing observations varying the parameters, this is discussed in Chapter 2.

3. A five-parameter function is used to model temporal variation in the background power level and is seperately fitted to both the Azimuth and Elevation scan data. The function consists of a Gaussian peak superimposed on a sloped straight line, and is given as follows:

$$f(x) = mx + p + ae^{\frac{(x-b)^2}{2c^2}} \tag{1.15}$$

   Where a, b and c are the peak temperature, offset and the half-power beamwidth of the scanned source. "p" is the offset and m is the slope in time.

4. The above process is repeated if the fitting fails or the peak for either axis is off by more than half the measured steps. This ensures that the fitting is well centred in the dataset, which is also helpful in the case of a weak source. One disadvantage is that if the fitting fails for a scan after numerous iterations, the program still generates fitted parameters. Those parameters must then be detected and discarded from the analysis.

5. The program then reports the five parameter values at the end of each complete scan along with an additional parameter (integer) that tells the number of iterations required by the program to achieve the fit. In case of a nominally successful fitting, the number is positive. For unsuccessful fitting, the program still reports parameters but assigns a negative integer.

6. Finally at the end of each complete scan in Azimuth and Elevation, the offsets are recorded with source Azimuth, Elevation, the standard deviation of the offsets, and two integers (either 1 and 0). Two "1"'s means a successful fit in both Azimuth and Elevation. Sometimes the fit is successful in only Azimuth or Elevation, in which case the output has either "1 & 0" or "0 & 1". Only successful fits in both Azimuth and Elevation are taken for analysis.

7. The program also records the same information, but corrects the Azimuth offsets for cosine of the Elevation (cross-Elevation). Cross-Elevation (XElv) is given by the following formula:

$$\Delta XElv = \Delta Azimuth \times \cos(El) \tag{1.16}$$

   The standard deviation for Azimuth offsets are also corrected for the Elevation. For the analysis, Azimuth and Elevation offsets were used.

The Field System provides "pdplt", a Tcl/Tk application with a Graphical User Interface (GUI) for pointing data analysis. It provides a wide range of options that includes examining sky coverage, plotting pointing data, viewing individual sources, removing outliers, using different statistical measures, editing data and

applying a pointing model to the data. Apart from the 6 terms described in the beginning of the chapter to account for different pointing errors, "pdplt" includes an additional 24 terms to address other possible pointing errors. Appendix A includes all the additional terms taken from the FS manual.

However, "pdplt" lacks some functionality required for our analysis. We wanted to have the flexibility of plotting any given scan of a source in Azimuth and Elevation. Our initial study suggested that some of the observed sources are extended and relatively weak. Plotting the source scans would have helped us to get a better understanding of the source morphology and its effects on pointing offsets. It would also help us in estimating a suitable combination of input parameters of the scan; i.e. the number of steps to take for each scan, the integration time at each point and the relative size of each step.

I wrote a script in Bash and R programming Language for pre-processing and analysing the raw pointing data. The overall process is described in the next chapter.

Chapter 2

30-metre Telescope Pointing

2.1 Pointing Data Processing

Several pointing observations were conducted using the "fivpt" program in the Field System. The pointing observation log file contains various information, not all of which is relevant to pointing. A Bash script was written (Appendix C) that sorts and extracts data from a pointing observation log files and save it into six different files, each explained on the following page. A screenshot of the log file with explanation is included in Appendix A.

Bash is a Unix shell command language that comes by default with Unix/Linux based systems. It comes with a command line interface, and also provides options to run multiple instructions/scripts written in a text editor [14]. Like any other programming language, Bash provides programming functionality such as assigning variables, command substitution, control structures for condition testing and iterations. In addition, it provides numerous useful commands such as wildcard matching, pipes (output from one process can be directly fed into another process as input), grep (for searching and extracting information using keyword and regular expression matching) and many others.

Six different classes of information on pointing observations were extracted from the observation log file into six different text files. They are as follows:

1. Data for each Azimuth scan for all sources.
2. Data for each Elevation scan for all sources.
3. Five parameters obtained after fitting a function consisting of a Gaussian and a linear function in Azimuth.
4. Five parameters obtained after fitting a function consisting of a Gaussian and a linear function in Elevation.
5. The final measured offsets for all scans in both Azimuth and Elevation.
6. The final measured offsets for all scans in cross-Elevation and Elevation.

Details on the type of information are provided in Chapter 1.

R was used for processing and analyzing the files obtained from the Bash script. R is a popular open source programming language mainly designed for statistical computing and graphics. R has numerous libraries providing a wide variety of statistical and graphical techniques, including classical statistical tests, time series analysis, linear and non-linear modeling, clustering and many others. It supports all common types of data structures including matrices, vectors, arrays, lists and data frames. For this research, we used a number of packages in R, including RGL (for 3D graphics), and NLS for non-linear least square regression.

As mentioned in Chapter 1, the FS provides an inbuilt application called "pdplt" that can process the pointing database to generate a pointing model. However as previously stated, the software lacks some functionality required for our analysis. We wanted to have the flexibility of plotting any given scan of a source in Azimuth and Elevation. This would help our research in the following way:

- The source database currently has 17 sources to generate a pointing database. However, our initial study suggested that some of the sources are extended and relatively weak. This makes those sources unsuitable, as it would add more noise to the database. Plotting the source scans helps to get a better understanding of the source morphology and its effects on pointing offsets.

- It seems that sometimes the FS failed to fit the 5-parameter function to the data, although by just looking at the source intensity (which rises and falls gradually) during the scan, it appeared that the data should be fitted. Plotting the scans would help us to understand whether the FS was actually failing to fit in some cases when it should have.

- Before running "fivept", we need to specify the scanning parameters in the proc file, which includes the number of steps to be taken for each scan, the integration time at each point and the relative size of each step. Visual inspection of the scan helps in estimating a suitable combination of input parameters for the scan.

Using R, a script was written that allows to enter source name and scan number (i.e. any particular scan we want to look for that source) and plot the desired scan. The following steps describe how the script works:

1. The script uses 5 out of the 6 output files (1 to 5 on previous page) generated from the Bash script. First it provides the option to import the Azimuth (denoted as "Longitude" in the FS) and Elevation (denoted as "latitude" in the FS) scan files and run a validation check to see if both contain the same number and steps of scans. Often, the log file contain incomplete scans, i.e. the scan(s) failed on one of the axis (Azimuth or Elevation) after a certain number of steps, although it completes the scan for the other axis. The script flags the index of the incomplete scan(s). These along with the corresponding scan(s) for the other axis (either broken or complete) are then removed. Both the tables are concatenated into a single table. Figure 2.1 shows the first 5 rows of a 31-step scan.

2. The FS parameter fit files (Azimuth and Elevation) are imported using the script. It then flags and removes the parameters generated for the incomplete scan(s) detected in the previous step. The Azimuth and Elevation parameter tables are then concatenated into a single table. Figure 2.2 shows the FS estimated parameters from 5 different scans of Taurus A.

	LonPointNo	LonTime	LonOffset	LonTemp	LonRMS	LatPointNo	LatTime	LatOffset	LatTemp	LatRMS	Source4Scan	Azimuth	Elevation	LonGoodFit	LatGoodFit
6495	1	31847	-0.4045	-0.409	0.514	1	31473	-0.3963	1.215	0.455	taurusa	50.0624	12.5436	5	5
6496	2	31859	-0.3775	1.255	0.488	2	31485	-0.3699	-0.054	0.590	taurusa	50.0624	12.5436	5	5
6497	3	31871	-0.3506	1.193	0.384	3	31497	-0.3434	-0.148	0.687	taurusa	50.0624	12.5436	5	5
6498	4	31883	-0.3236	1.156	0.364	4	31509	-0.3170	0.043	0.366	taurusa	50.0624	12.5436	5	5
6499	5	31895	-0.2966	0.692	0.780	5	31521	-0.2906	0.315	0.602	taurusa	50.0624	12.5436	5	5

Figure 2.1: The table (first 5 rows) produced using R script after processing and concatenating the Azimuth and Elevation scan files.

	LonGPeakOffset	LonFWHM	LonPeakTemp	LonOffset	LonSlope	LonGoodFit	LatGPeakOffset	LatFWHM	LatPeakTemp	Latoffset	LatSlope	LatGoodFit	Source
211	0.01079	0.1051	45.3805	0.1739	-0.0035	5	0.02538	0.0935	43.5739	0.2360	-0.0002	5	taurusa
215	0.00210	0.1017	48.0813	-0.4248	0.0002	4	-0.01259	0.0974	46.5060	0.5755	0.0018	5	taurusa
219	0.00331	0.1023	50.4962	1.1734	0.0015	5	-0.03278	0.0946	51.1270	1.5012	0.0018	5	taurusa
223	-0.00339	0.1017	51.5347	0.3677	0.0023	4	-0.04255	0.0936	49.9235	-0.3195	-0.0021	5	taurusa
226	-0.01319	0.0983	52.1281	-0.0054	-0.0027	5	-0.05023	0.0944	50.2779	0.4973	-0.0010	4	taurusa

Figure 2.2: The table (first 5 rows) created using R script after processing and concatenating the Azimuth and Elevation FS parameter files.

3. Using the first of the above two tables, the script plots the scans in Azimuth (top) and Elevation (bottom), with the offsets in the axis and the relative intensity in the y-axis. It then fits the function (Gaussian + straight line) using the FS parameters from the second table. We also derived parameters for the fitting function using a second method[3] (non-linear least square regression) [15] to compare it with the FS generated parameters. This was done to see whether the FS generated offsets (from FS fitting) are any different to the ones we estimated and whether the "Fivept" program requires any improvement.

   Figure 2.3 shows a typical scan of the Orion A plotted with the R-script.

4. It is clear from Figure 2.3 that a 31-step scan was not necessary as the source can be well acquired with fewer steps. Also, the centre (offset) estimated by

[3]Although the FS uses the 5-parameter function (as described above) to model the scan, it subtracts the background intensity (modelled by the straight line) from the y-values (relative intensity). For strong sources, the change is not noticeable (Figure 2.2, the fits are near identical). However for weak sources, the background intensity is significant relative to the source intensity, so the slope can be noticeable (check plot of Pictora in Appendix B). To check, the script again plots the fitting function using the second method (as described above) but subtracts the background intensity [R-Fit (No Slope) in Figure 2.2].

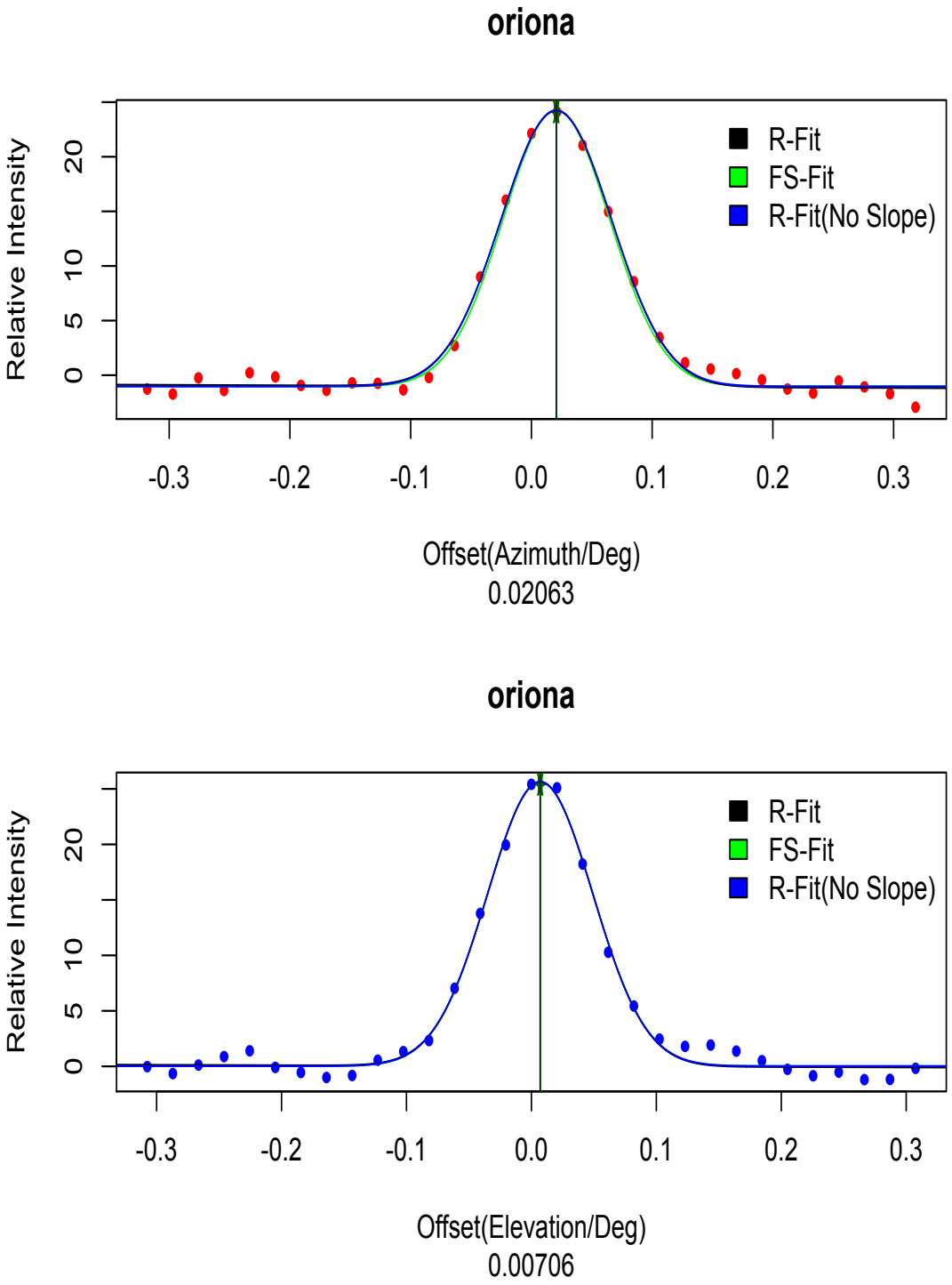

Figure 2.3: A complete scan of Orion A in Azimuth and Elevation. The x-axis represents the offset (in Degrees) and the Y-axis represents the relative intensity. The offsets obtained by fitting the 5 parameter function(FS) is reported in the plot. There is an error bar (in σ) on the centred line, however, as Orion A is a strong source, the error associated with the offset is negligible; 0.0003° for Azimuth and 0.0012° for Elevation. So the error bar (in arrow) appears squashed.

the FS parameters (green) is almost identical to the offset generated using the second method (black). Several scans from various pointing databases were evaluated using the above procedure. Our results concluded that a 13-step scan, with a step size being 0.2 of the beam is sufficient to completely acquire a source (including extended sources). Appendix C includes a "31-step scan-plot" for all 17 sources currently used for pointing. These plots gives an idea about the morphology of the sources used for pointing at 6.7 GHz.

5. The script then performs a data cleansing process. As mentioned in Chapter 1, the FS generates offsets even if it fails to fit the 5-parameter function, and assigns "1" for successful and "0" for unsuccessful fitting. The script only includes offsets that are generated by successful fitting in both Azimuth and Elevation and discards the rest.

6. The pointing data collection process can be influenced by various external factors (RFI, abrupt rise in system temperature etc.) and will generate corrupt data (outliers). This will happen even though successful fitting of the 5-parameter function by the FS occurs. To visualize the current distribution of the offsets, the script generates a histogram for the Azimuth and Elevation offsets, followed by boxplots to show potential outliers and possible skew in the distribution (Figure 2.4).

7. The histogram of the Azimuth in Figure 2.4 has significant outliers, which is also confirmed by the following boxplot. The Elevation distribution also has some potential outliers, with one confirmed by the boxplot.

8. We used the interquartile outlier rule that uses the median value to estimate the centre of the distribution to remove the outliers. The median generally gives a better estimation of the central tendency than mean for skewed distributons [16]. It is also evident in Figure 2.5 where median (red) fits the distribution slightly better than the mean (green).

9. The script also generates Normal probability plots (normal qq plots, Figure 2.6) to check the normality of the distributions with outliers removed. If a

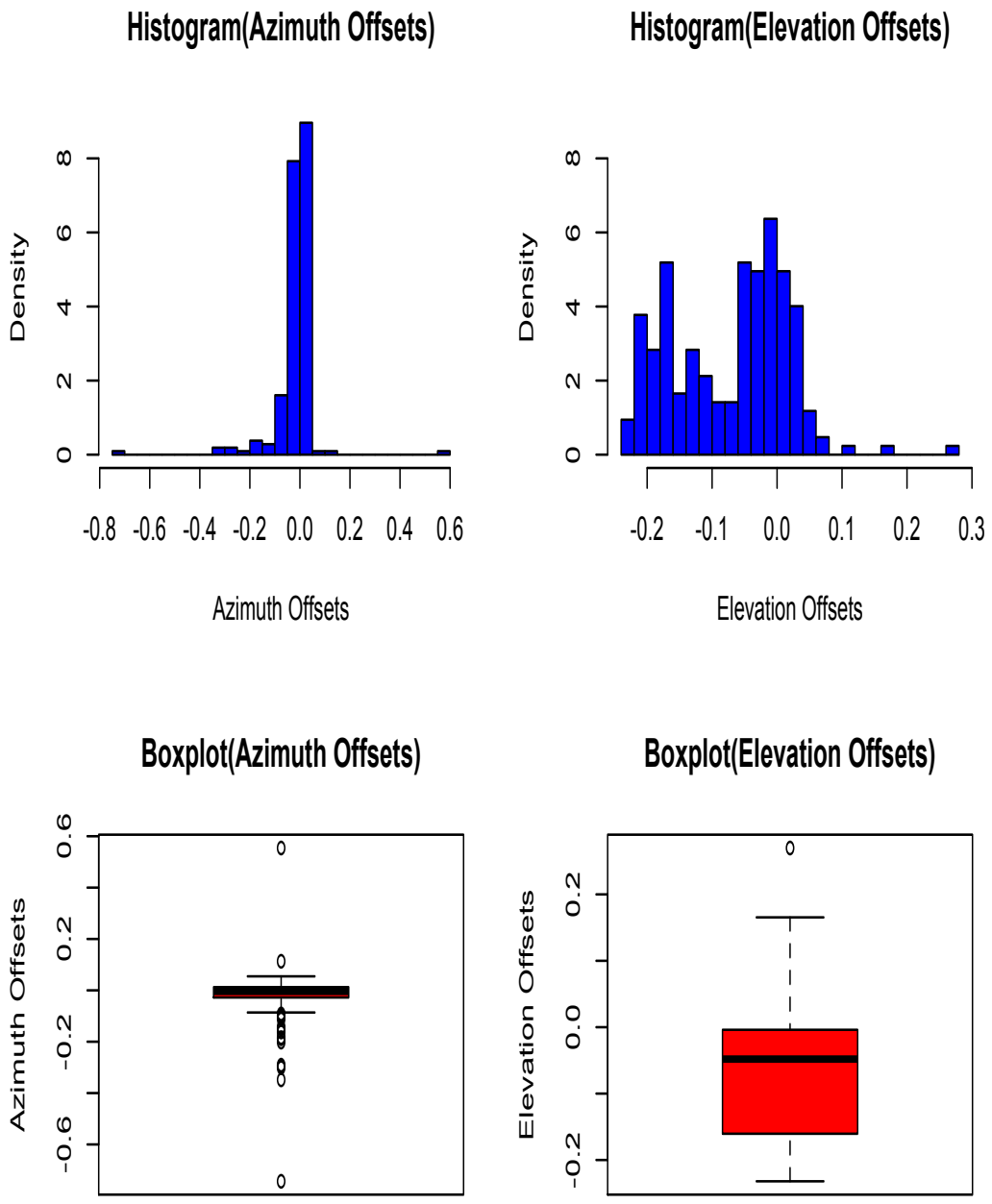

Figure 2.4: The distribution of Azimuth (top-left) and Elevation (top-right) offsets. Even after removing data that FS failed to fit, a significant number of outliers are observed in the distribution of the Azimuth offsets. The outliers are clearly visible from boxlpot of Azimuth (bottom left) and Elevation (bottom right) offsets. The Elevation offset distribution is bimodal and has a negative skew, with only one visible outlier.

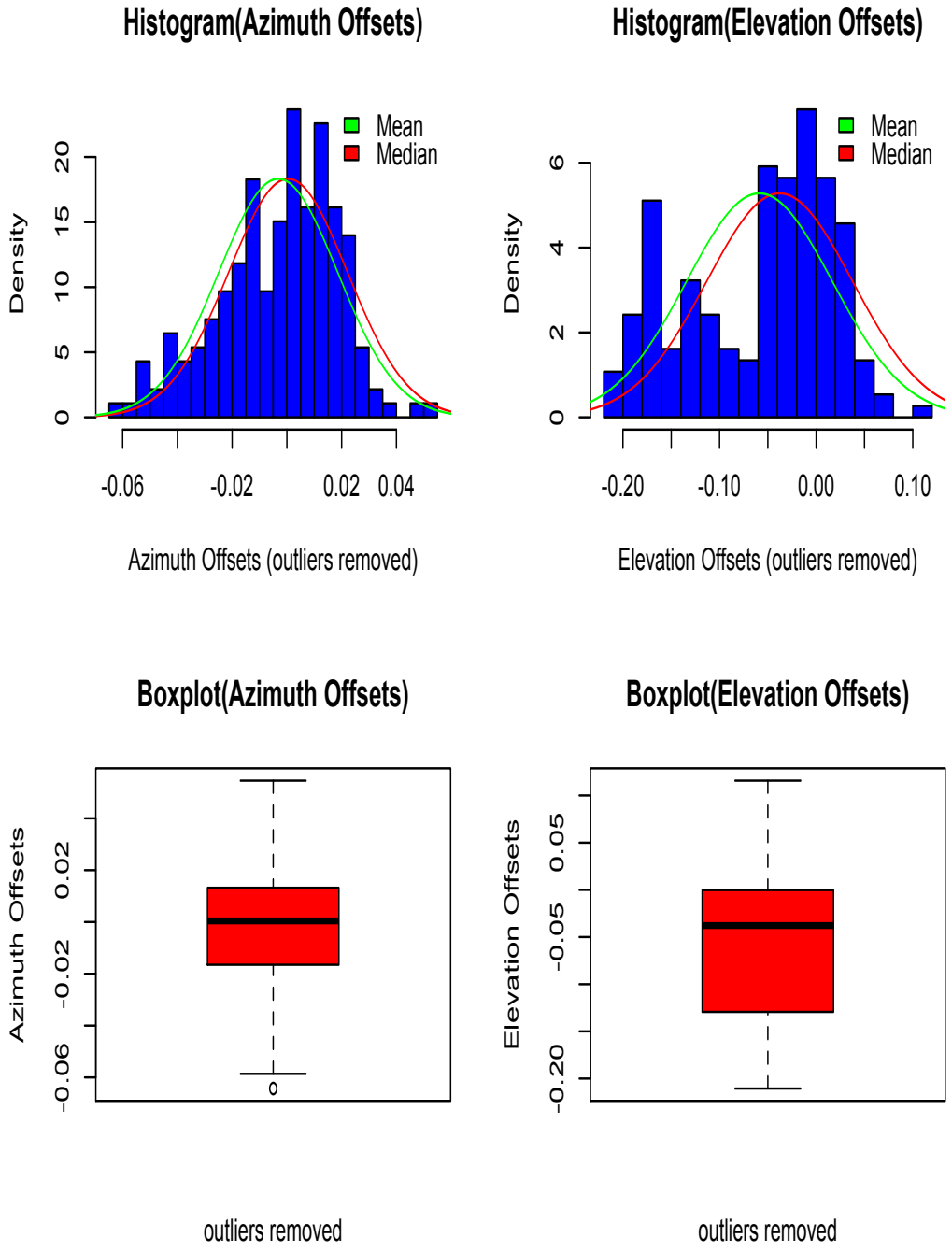

Figure 2.5: Histogram and boxplot of Azimuth and Elevation offsets with the outliers removed. While the Azimuth-offset distribution appears to be a skewed Gaussian (top-left), the Elevation-offset distribution appears to be bimodal. In both cases, the Gaussian fit with median as centre (red) gives a better estimate of the centre than mean (green). The boxplots (bottom left for Azimuth and bottom right for Elevation) shows the outliers removed, although one probable outlier is still present in Azimuth. The rms of the Azimuth and Elevation offsets decreases to 0.047° and 0.0677° from 0.087° and 0.114° after applying the outlier removal process.

distribution is perfectly normal with no skew, the theoretical quantiles will all lie on the line y=x (blue). However this is not the case, as the offsets are not normally distributed but some non-linear functions of the geometric orientation between the dish and source. This is reflected in Figure 2.6 as the weak correlation (especially in elevation) suggests the lack of normality and a high skew in the distributions. The normal probability plot (Figure 2.6) is more appropriate and useful to check the Gaussianity of the residuals after post fitting. The script will produce plots (like Figure 2.4 and 2.5) every time a new pointing database is processed and can be used for visualizing the distribution of the offsets and also the residuals (after post fitting).

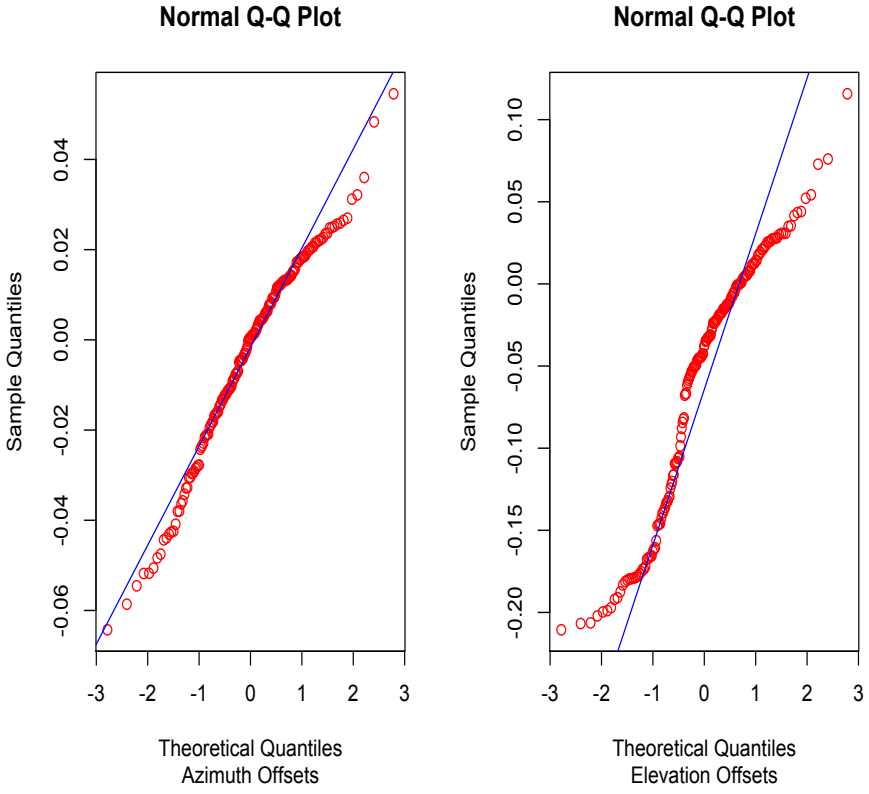

Figure 2.6: A normal probability plot (normal Q-Q Plot) of the Azimuth and Elevation offsets. The plots are used to visually check whether the data are approximately normally distributed. The data are plotted in such a way against a theoretical normal distribution that it should fall approximately along y=x line. The Azimuth offset (left) plot deviates at the edge, showing lack of normality. The Elevation offsets shows a bimodal pattern.

One might question the use of the interquartile outlier rule to address the above problem, as the distributions, particularly Elevation offsets does not appear to be normally distributed. Other approaches like the Gamma distribution (which is closely related to Exponential, Erlang and Chi-Square) could have been used to model the offsets and to identify the potential outliers. For a random variable x, where x $\sim$ Gamma(α, λ), it has probability density function, for some $\alpha > 0$ and $\lambda > 0$:

$$f(x) = \begin{cases} \frac{x^{\alpha-1}\lambda^{\alpha}e^{-\lambda x}}{\Gamma(\alpha)}, & \text{if } x \geq 0 \\ 0, & \text{otherwise} \end{cases}$$

Note how the probability density function is 0 for negative random variable (i.e. for x $<$ 0). The same condition applies for Exponential, Erlang and Chi-Squared distribution, i.e. x cannot be negative. In our case, almost half of the pointing offsets were negative. Although the modulus of the offsets can be taken to counter the negative offsets, there was no additional advantage in using the process. So we decided to use the IQR outlier rule as is was simple and effective to address the outlier problem with the pointing data. More robust outlier removal techniques could be explored in the future.

10. The script then uses the processed data to generate a pointing model. The current pointing model uses 9 terms and is given by the following equations:

$$\Delta Az = P_1 + P_3 \tan(El) - P_4 \sec(El) + P_5 \sin(Az) \tan(El) - P_6 \cos(Az) \tan(El) \quad (2.1)$$

$$\Delta El = P_5 \cos(Az) + P_6 \sin(Az) + P_7 + P_8 \cos(El) + P_{23} \cot(El) \quad (2.2)$$

The script creates matrices for the two systems of equations using the actual Azimuth, Elevation and their corresponding offsets. The equations are given as follows:

For Azimuth:

$$\begin{matrix} P_1 & P_3 & P_4 & P_5 & P_6 \end{matrix} \quad Az_{Offset}$$
$$\begin{pmatrix} 1 & tanEl_1 & secEl_1 & sinAz_1tanEl_1 & cosAz_1tanEl_1 \\ 1 & tanEl_2 & secEl_2 & sinAz_2tanEl_2 & cosAz_2tanEl_2 \\ 1 & tanEl_3 & secEl_3 & sinAz_3tanEl_3 & cosAz_3tanEl_3 \\ .. & .. & .. & .. & .. \\ .. & .. & .. & .. & .. \\ 1 & tanEl_n & secEl_n & sinAz_ntanEl_n & cosAz_ntanEl_n \end{pmatrix} = \begin{pmatrix} \delta Az_1 \\ \delta Az_2 \\ \delta Az_3 \\ .. \\ .. \\ \delta Az_n \end{pmatrix}$$

For Elevation:

$$\begin{matrix} P_5 & P_6 & P_7 & P_8 & P_{23} \end{matrix} \quad El_{Offset}$$
$$\begin{pmatrix} cosAz_1 & sinAz_1 & 1 & cosEl_1 & cotEl_1 \\ cosAz_1 & sinAz_1 & 1 & cosEl_1 & cotEl_1 \\ cosAz_1 & sinAz_1 & 1 & cosEl_1 & cotEl_1 \\ .. & .. & .. & .. & \\ .. & .. & .. & .. & \\ cosAz_n & sinAz_n & 1 & cosEl_n & cotEl_n \end{pmatrix} = \begin{pmatrix} \delta El_1 \\ \delta El_2 \\ \delta El_3 \\ .. \\ .. \\ \delta El_n \end{pmatrix}$$

For the dataset used to demonstrate the outlier removal process (explained above), there were 186 observations (n=186) after removing the outliers. Since the two sets of equations have common terms (P_5 and P_6), the script combines them to create a Vandermonde Matrix [17].

$$\begin{matrix} P_1 & P_3 & P_4 & P_5 & P_6 & P_7 & P_8 & P_9 \end{matrix} \quad Offsets$$
$$\begin{pmatrix} 1 & tanEl_1 & secEl_1 & sinAz_1tanEl_1 & cosAz_1tanEl_1 & 0 & 0 & 0 \\ 1 & tanEl_2 & secEl_2 & sinAz_2tanEl_2 & cosAz_2tanEl_2 & 0 & 0 & 0 \\ .. & .. & .. & .. & .. & .. & .. & .. \\ .. & .. & .. & .. & .. & .. & .. & .. \\ 1 & tanEl_n & secEl_n & sinAz_ntanEl_n & cosAz_ntanEl_n & 0 & 0 & 0 \\ 0 & 0 & 0 & cosAz_1 & sinAz_1 & 1 & cosEl_1 & cotEl_1 \\ 0 & 0 & 0 & cosAz_1 & sinAz_1 & 1 & cosEl_1 & cotEl_1 \\ .. & .. & .. & .. & .. & .. & .. & .. \\ .. & .. & .. & .. & .. & .. & .. & .. \\ 0 & 0 & 0 & cosAz_n & sinAz_n & 1 & cosEl_n & cotEl_n \end{pmatrix} = \begin{pmatrix} \delta Az_1 \\ \delta Az_2 \\ .. \\ .. \\ \delta Az_n \\ \delta El_1 \\ \delta El_2 \\ .. \\ .. \\ \delta El_n \end{pmatrix}$$

11. Using the built in Linear Least Square regression function in R, the script solves the above equation to estimate the coefficients P_1,P_3 toP_8 and P_{23}.

Least squares is widely used for data fitting and the goodness of a fit depends on how much the model can minimize the sum of squared residuals (the residuals being the difference between the observed value and the fitted value from the model) [15].

12. The script then outputs the value of the terms/parameters estimated using least square regression. The values obtained for the dataset are given in Table 2.1.

Table 2.1: The table shows the values of the terms/coefficients estimated using Least Square Fitting by our script. A brief description of the terms are provided, more details can be found in Chapter 1: Literature Review

Terms	**Coefficient(FS)**	**Standard Error(±)**	**Description**
P_1	-0.042	0.017	Azimuth angle offset
P_3	-0.073	0.015	Elevation axis skew angle
P_4	-0.072	0.022	the magnitude of the collimation axis misalignment
P_5	-0.005	0.002	Tilt out
P_6	-0.002	0.001	Tilt over
P_7	-0.342	0.009	difference of the Elevation angle encoder bias
P_8	0.312	0.015	effect of gravity on the Elevation
P_{23}	0.015	0.002	residual refraction error

Using the estimated terms/parameters and the actual Azimuth and Elevation, we generate offsets using the model. We call these offsets modelled offsets. If the pointing model were near perfect, the modelled offsets would be nearly identical to the actual offsets generated by FS for the same Azimuth and Elevation.

13. The script then plots the actual (red) and the modelled (blue) Azimuth offsets against Azimuth. The residuals from the model ($actual_{offsets} - modelled_{offsets}$) are plotted as well (Figure 2.7). It does the same for Elevation (Figure 2.8).

As mentioned in Chapter 1, for the telescope to operate effectively, we should be able to point the RF axis within 10% of the FWHM. For the 30-metre at 6.7 GHz, 10% of the FWHM (0.104°) is approximately 0.01°. However, this is not

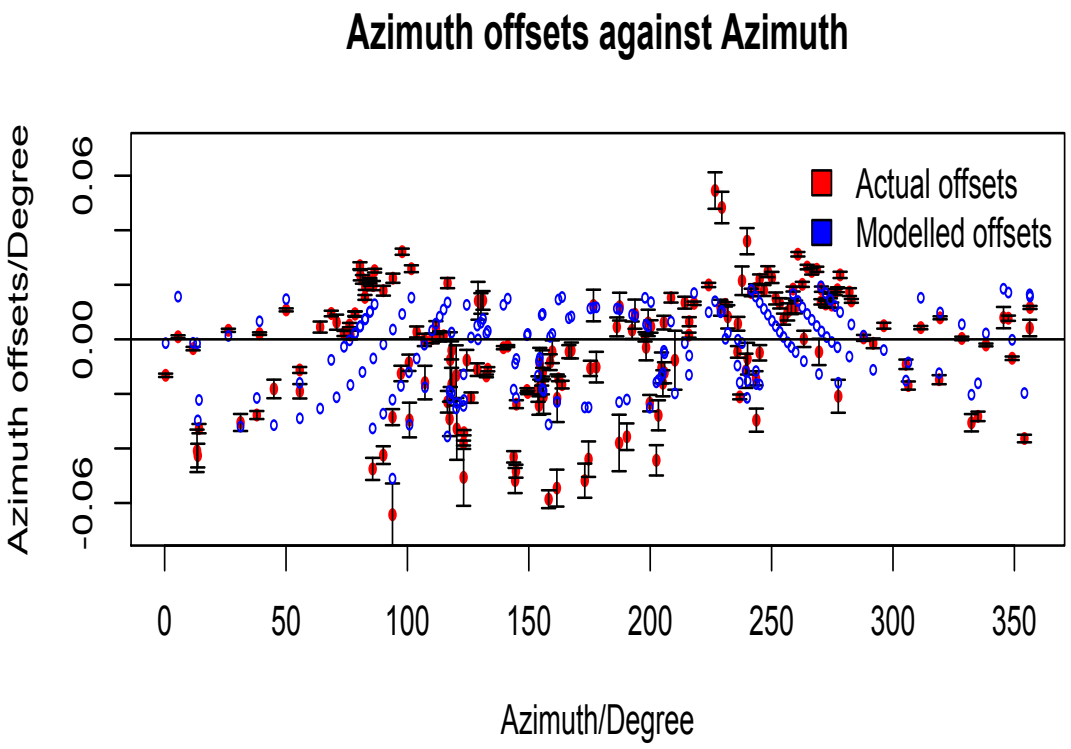

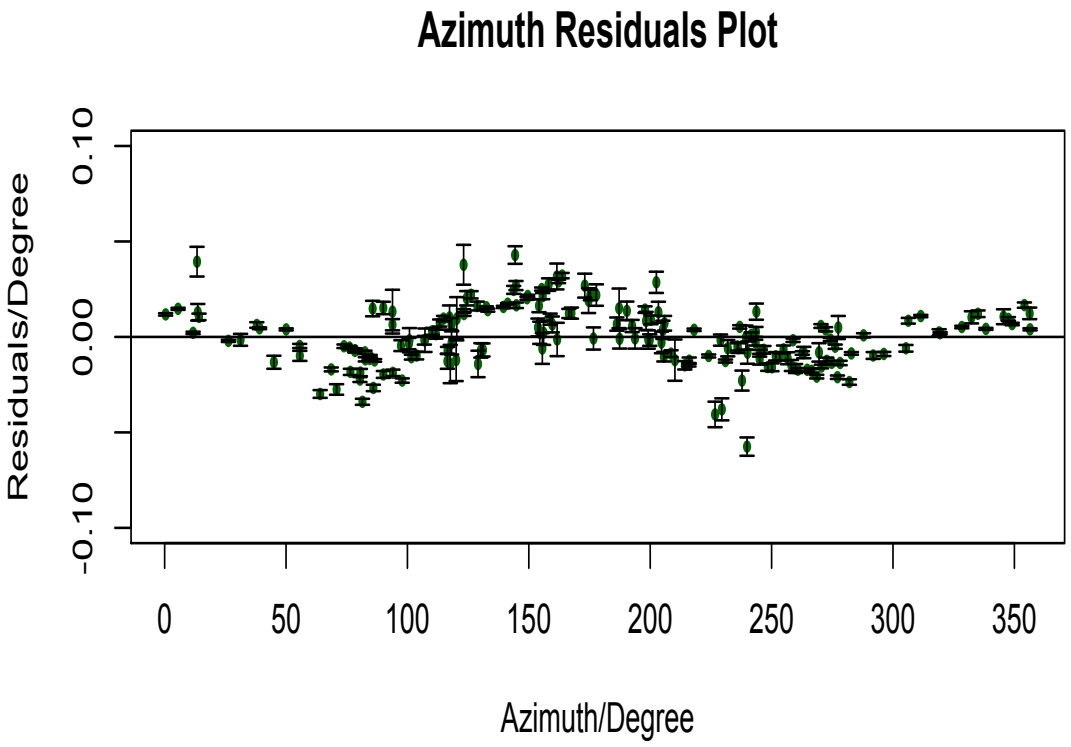

Figure 2.7: Plot of the actual (red) and modelled(blue) Azimuth offsets against Azimuth. The model seems to somewhat predict the actual offsets. A sinusoidal pattern is observed in the residuals. The rms of the actual offsets is $\sim 0.0229°$ and the residuals is $\sim 0.0155°$, also indicating the model theoretically minimizes the error. The error bars are the standard deviation associated in estimating each offset.

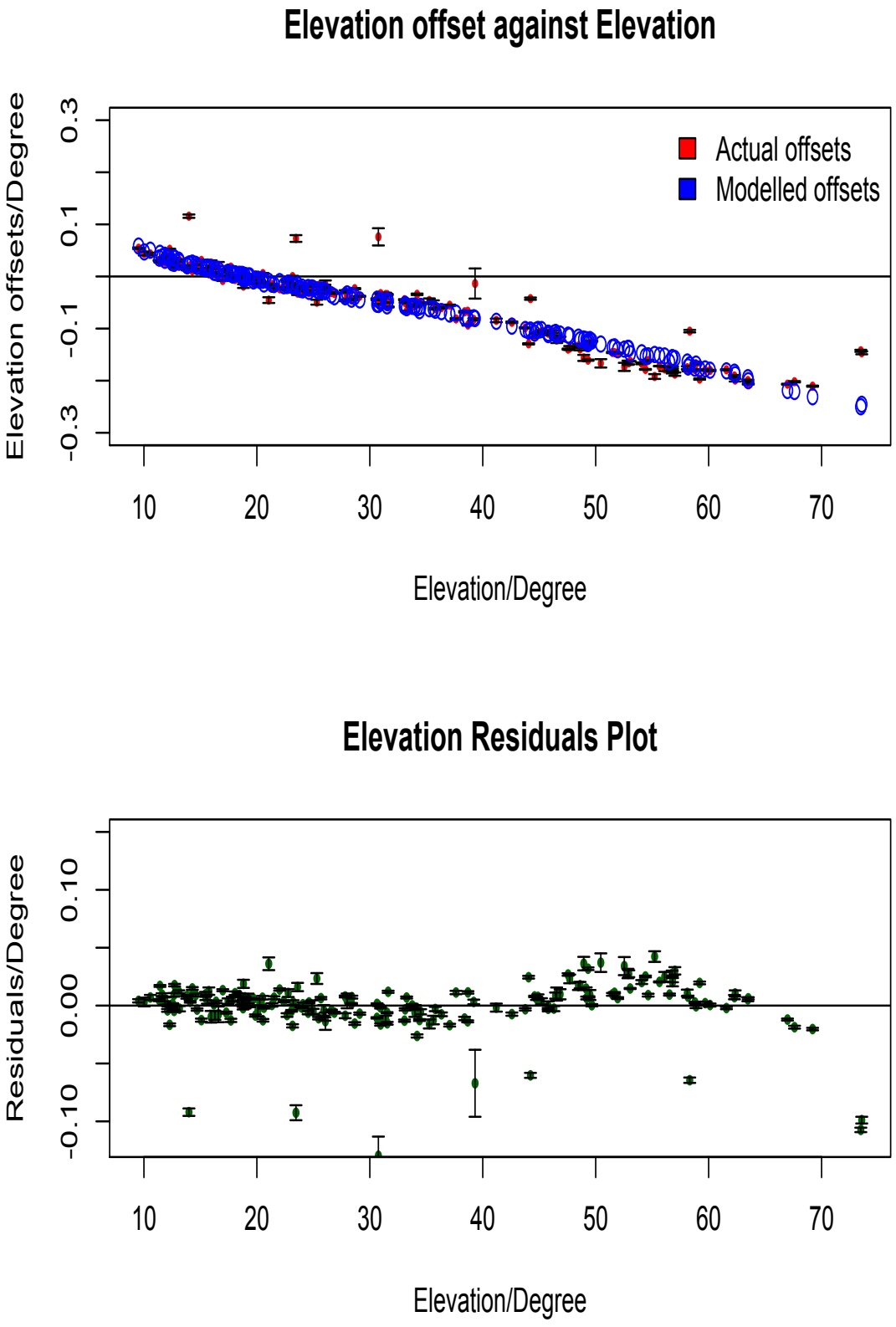

Figure 2.8: Plot of the actual (red) and modelled (blue) Elevation offsets against Elevation. A sinusoidal pattern is observed in the actual offsets. The model seems to reasonably predict the actual offsets. The rms of the actual offsets is $\sim 0.0955°$ and the residuals is $\sim 0.0229°$, also indicating the model significantly minimizes the error. However, it is far from the pointing accuracy we would like to achieve. A few outliers are also observed.

the case for the above dataset. The rms of the actual offsets in Azimuth and Elevation was 0.0219° and 0.0955°. After applying the model, the rms of the residuals for Azimuth and Elevation offset was 0.015° and 0.0229°. While the model significantly lowers the rms, it is still over the prescribed 10%. The scatter in the offsets (especially in Elevation) are significantly high (even after removing outliers), and a sinusoidal pattern is observed in the residuals of both Azimuth (Figure 2.7) and Elevation plot (Figure 2.8). The pattern and the scatter in the offsets significantly contributes to the high rms of the residuals. Later in the chapter, we try to minimize the scatter by choosing good pointing sources, and address the sinusoidal pattern by adding new terms to the model. An ideal/good pointing source should be radio bright and have an angular size much smaller than the size of the beam. However, in practice there are not enough point sources that can be used to get a good coverage of sky. So we try to find and use sources that are radio bright and minimally resolved by the beam. We call these sources "good pointing sources".

It is important to note that generally the estimated offsets by the “fivept” program in the FS are actually residual offsets, i.e. the offsets generated are relative to the current active pointing model in the FS. So to find actual offsets, all the terms need to be zeroed in both the antenna controller and the FS mdlpo.ctl file before new data are acquired. The offsets processed above are the actual offsets, which is why the magnitude of the offsets and the scatter in the offsets are relatively large.

Throughout the research, we carried out numerous pointing observations using the FS. Results from three pointing observations (actual offset in C-Band, and relative offset in C and X band) are discussed in this chapter. The offsets were processed using my script and the results were compared.

2.2 Actual Offsets (C-Band): Source Analysis

We start by analyzing the database processed in the previous section that contains true/actual offsets as explained in Section 2.1. While in principal our script improves the quality of the database by removing outliers, the quality of the sources used for pointing is very important and needs to be taken into consideration before commencing any pointing observation. Selecting good pointing sources for observation will help the overall pointing process by:

- Reducing the observation time needed for a pointing solution.
- Reducing overall noise in the pointing database.

Seventeen sources were used for the above pointing database. Appendix B includes plots of a single scan (Azimuth and Elevation) for all seventeen sources, produced with our script. Just by looking at the scans, we can comment on the relative strength of the source. However, a more comprehensive approach was required.

As mentioned earlier in Chapter 1, the standard deviation associated with the offsets (Azimuth and Elevation) from the five parameter function fitting for each individual scan of the sources were also recorded in the log file. Strong pointing sources such as Taurus A will have small standard deviation in the offsets compared to Centaurus A, which is weaker than Taurus A. Using R, we separated the standard deviation for Azimuth and Elevation offsets by each source. We assume the offsets in Azimuth and Elevation to be statistically dependent as they are a non-linear function of the geometric orientation of the antenna and include both Azimuth and Elevation. The standard deviation of each offset in Azimuth and Elevation was combined using the following formula:

$$\sigma_{Offset} = \sqrt{\sigma_{Az}^2 + \sigma_{El}^2 + 2cov(\sigma_{Az}, \sigma_{El})} \tag{2.3}$$

where σ_{Az}, σ_{El} are the standard deviation of the Azimuth and Elevation offsets estimated using the five-parameter function, cov is the covariance between σ_{Az} & σ_{El} and σ_{Offset} is the combined standard deviation for the offsets.

We then calculated the mean of the combined standard deviation for all the scans by individual sources. Table 2.2 (column 4 & 5) shows the average of the standard deviation corresponding to each source in ascending order (strong → weak source).

A methanol maser source G323 observed for pointing has the highest standard deviation, almost 40 times more than Taurus A, which has the lowest. For good pointing accuracy, the antenna RF axis should be able to point within 10% of the FWHM. So ideally, sources with standard deviation less than 10% (of FWHM: 0.104°) should be used for pointing. However, we shouldn't exclude too many sources, as it is also important to get good sky coverage for building a pointing database. We came up with another method to backup our source selection process.

This method takes account of the dispersion in the offsets of each individual source (in Elevation). The method described previously gives a somewhat microscopic view on the quality of the sources, since we zoom into each source to look at the standard devation of the offsets from the five-parameter function fitting (microscopic method onwards). Looking at the dispersion of the offsets for individual sources rather gives what can be described as a macroscopic view, as the criteria doesn't look at each individual offset but to all the offsets of each source (macroscopic method onwards). The argument is explained below.

The offsets from a particular source will always vary due to systematic and unsystematic pointing errors associated with the telescope and the movement of the antenna as it points at the source at different positions in the sky. The dispersion in offsets of that source, however, should not be significant, and may be explained by a linear function. Figure 2.9 shows the offsets of Taurus A, a strong source, and Pictor A, a weak source, plotted against Elevation.

Offsets estimated using strong sources would follow a strong linear trend with least dispersion when plotted against Elevation (Figure 2.9: Taurus A). As explained

in the above paragraph, the linear trend would arise due to the assumption that the offsets from individual sources should not have significant variations. The slope can take any trend (for this dataset it was negative) and will depend on the systematic error that arises possibly from mechanical misalignment. Weak sources (e.g. Figure 2.9: Pictor A), on the other hand will exhibit high dispersion in the offsets due to lower signal to noise ratio and therefore the margin of error associated in estimating each offset will be significantly higher.

We limited our dispersion analysis to just Elevation, as doing it in Azimuth raises complications for circumpolar sources (the offsets are plotted with circles). Only analyzing the dispersion in Elevation should be good enough to compare and comment on the strength of the source, as the behavior of offsets in Azimuth and Elevation are similar (i.e. sources with higher Elevation offset has higher Azimuth offset and vice-versa). Table 2.2 (column 4) shows the standard deviation of the residuals derived by fitting a linear function to Elevation offsets against Elevation.

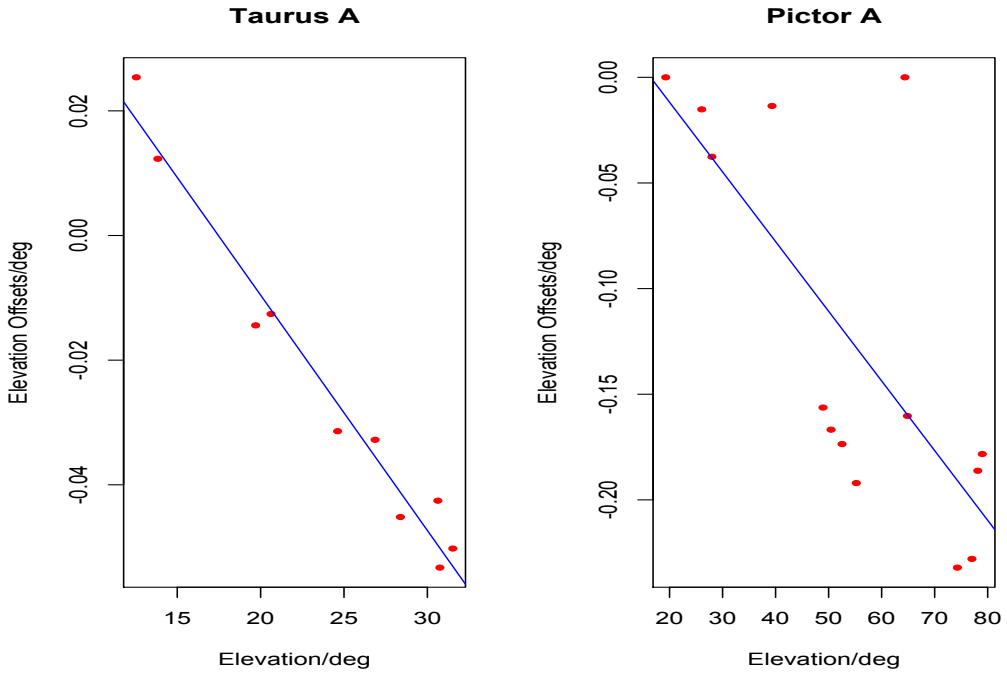

Figure 2.9: The plots shows the elevation pointing offsets of Taurus A and Pictor A plotted against Elevation. The dispersion of the offsets in Pictor A is significantly higher than Taurus A. The coefficient of determination (R^2), which measures the goodness of a linear fit, is 0.97 for Taurus A and 0.56 for Pictor A. [$0.8<R^2<1$ is strong correlation]

In Table 2.2, the sources are arranged by the standard deviation found using the microscopic method (lowest → highest) and are well supported by the standard deviation from the macroscopic method. The standard deviation from the macroscopic method increases as well in ascending order, although it differs in order of strength for a few sources with the microscopic process. For example with the microscopic method, source Sagittarius A comes before 3c84, but is the other way around with the macroscopic method. However, the differences are minimal and do not affect the source selection process.

Table 2.2: Shows the standard deviation of the offsets obtained from the microscopic and the macroscopic method. The sources are ordered according to their strength (strong → weak) using the Microscopic method. Taurus A has the best fitting by the 5 parameter function (microscopic method) and has the least standard deviation. Scan (%) shows the percentage of scan done for each source out of the total complete scans. The most number of scans was done for Sagittarius A (11.83%) and the least for Cygnus A and NGC 1275 (1.08%). The standard deviation obtained using macroscopic method are given, which also increases in ascending order (with some exception for a few sources). The relative intensity (described in Chapter 1) also agrees with the order (with a few exceptions). The methanol masers (index: 13 to 17) were too weak to measure reliably.

Index	**Source**	**Scan** (%)	**Microscopic** (σ)	**Macroscopic** (σ)	**Intensity (r.i.)**
1	Taurus A	3.58	0.00084	0.0047	45.38
2	Cygnus A	1.08	0.00117	0.0012	26.11
3	Orion A	9.68	0.00152	0.0096	25.28
4	NGC6618	9.68	0.00215	0.0155	29.40
5	CTB 031	6.09	0.00267	0.0124	18.47
6	NGC 3603	7.17	0.00380	0.0093	10.60
7	Sagittarius A	11.83	0.00399	0.0125	12.42
8	NGC 1275	1.08	0.00563	0.0085	4.47
9	Centaurus A	4.30	0.00680	0.0208	6.09
10	30 Doradus	11.46	0.00711	0.0112	2.71
11	CTB 032	5.02	0.01140	0.0201	2.67
12	Pictor A	5.03	0.01776	0.0340	1.48
13	g18895	3.94	0.02535	0.0443	0.00
14	g351	3.94	0.04151	0.0909	6.00
15	g309	6.09	0.06632	0.0968	0.05
16	g328	5.02	0.07301	0.1317	0.00
17	g323	5.02	0.07995	0.0741	0.00

It is to be noted that the macroscopic method by itself is not a good source selection process, as for sources with a small number of scans (offsets data), it is likely to produce a poor linear fitting and thus result in higher standard deviation in the residuals. For example we consider Taurus A to be a strong pointing source; however, if the pointing database only contains a few pointing scans from Taurus A, and one of them is corrupted, it can result in a poor linear fitting of the offsets. On the other hand, the microscopic method accounts for the standard deviation of each individual scans/data points, and hence would be unaffected like the macroscopic method. So the "microscopic method" is the first criteria for our source selection, and the macroscopic method is used to support the "microscopic method".

Figure 2.10 shows the standard deviation estimated using the microscopic and macroscopic method (Table 2.2, column 3 and 4) plotted against the index (strength, highest $\rightarrow$ lowest) of the source. The standard deviation (microscopic) of 10 sources (Taurus A to Centaurus A) stays within 10% of the beam. The standard deviation from the macroscopic method agrees with the order of strength for most of the sources. As mentioned earlier, the error associated with the macroscopic process can be high compared to the microscopic process, and is clearly visible from the Figure 2.10 (most of the blue points are above the red points).

The morphology of the sources (Appendix C) agrees well with the order of strength established using the methods. Sources with standard deviation (microscopic method) between 0° and 0.005° can be safely regarded as a strong pointing source, while anything within 0.005° to 0.01° is considered moderate, and anything more is weak. From the current survey, 49.38% are good sources, 16.84% are moderate, and the rest 33.77% are weak.

- **Strong Sources:** Taurus A, Cygnus A, Orion A, NGC 6618, CTB 31, Sagittarius A, NGC 3603, 3c84
- **Moderate Sources:** Centaurus A, 30 Doradus
- **Weak Sources:** CTB 32, Pictor A, g351, g18895, g309, g328, g323

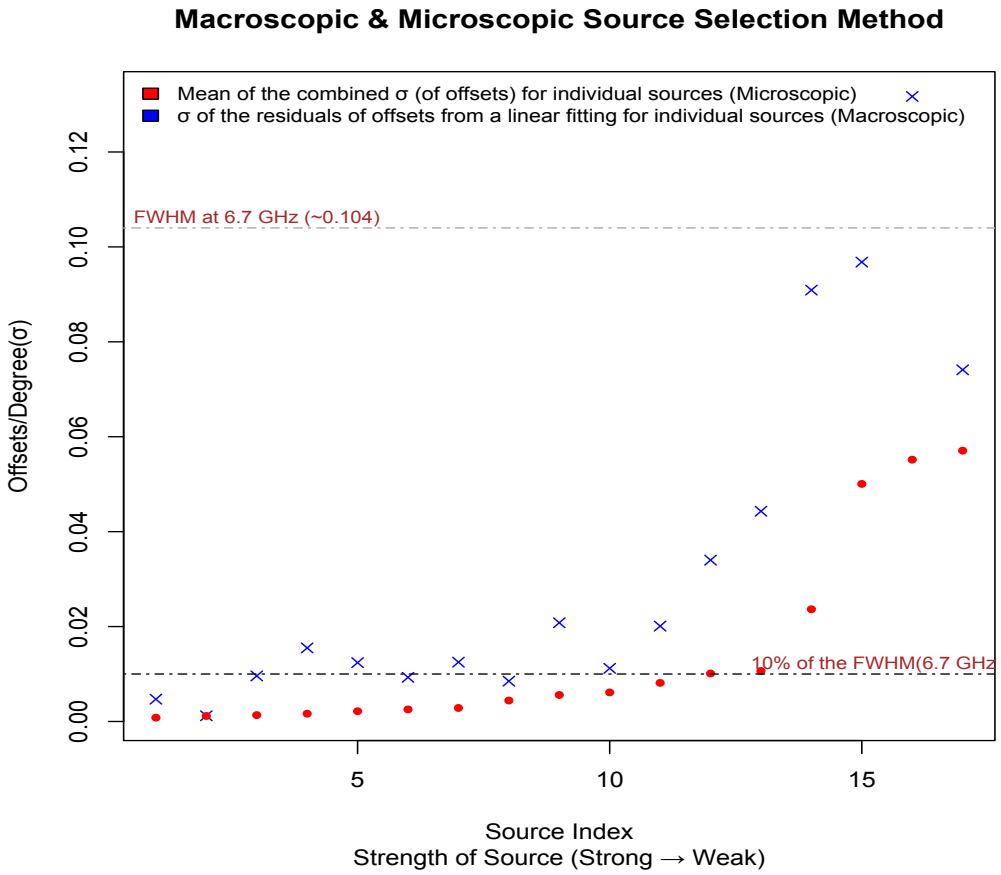

Figure 2.10: Shows the Macroscopic and Microscopic source selection method. The x-axis shows the strength of the source in descending order (from Table 2.2). Eleven sources have standard deviation (estimated using microscopic method) less than 10% of the FWHM. The standard deviation estimated for most of those eleven sources using the macroscopic method is higher than 10% of the FWHM, however, is consistent with the results from microscopic method.

Figure 2.11 shows the sky coverage of the sources. The top plot shows the coverage with all sources, whereas the bottom plot shows only the strong and moderate sources. Previously, we were concerned whether removing weak sources can affect pointing due to less sky coverage. However, as it seems from Figure 2.11 (bottom plot), even after removing the weak sources, we still get good sky coverage. So our method of source selection seems to work well. Later in the chapter, we will use offsets from all sources and offsets from only strong and moderate sources to see the effect in estimating the parameters of the pointing model.

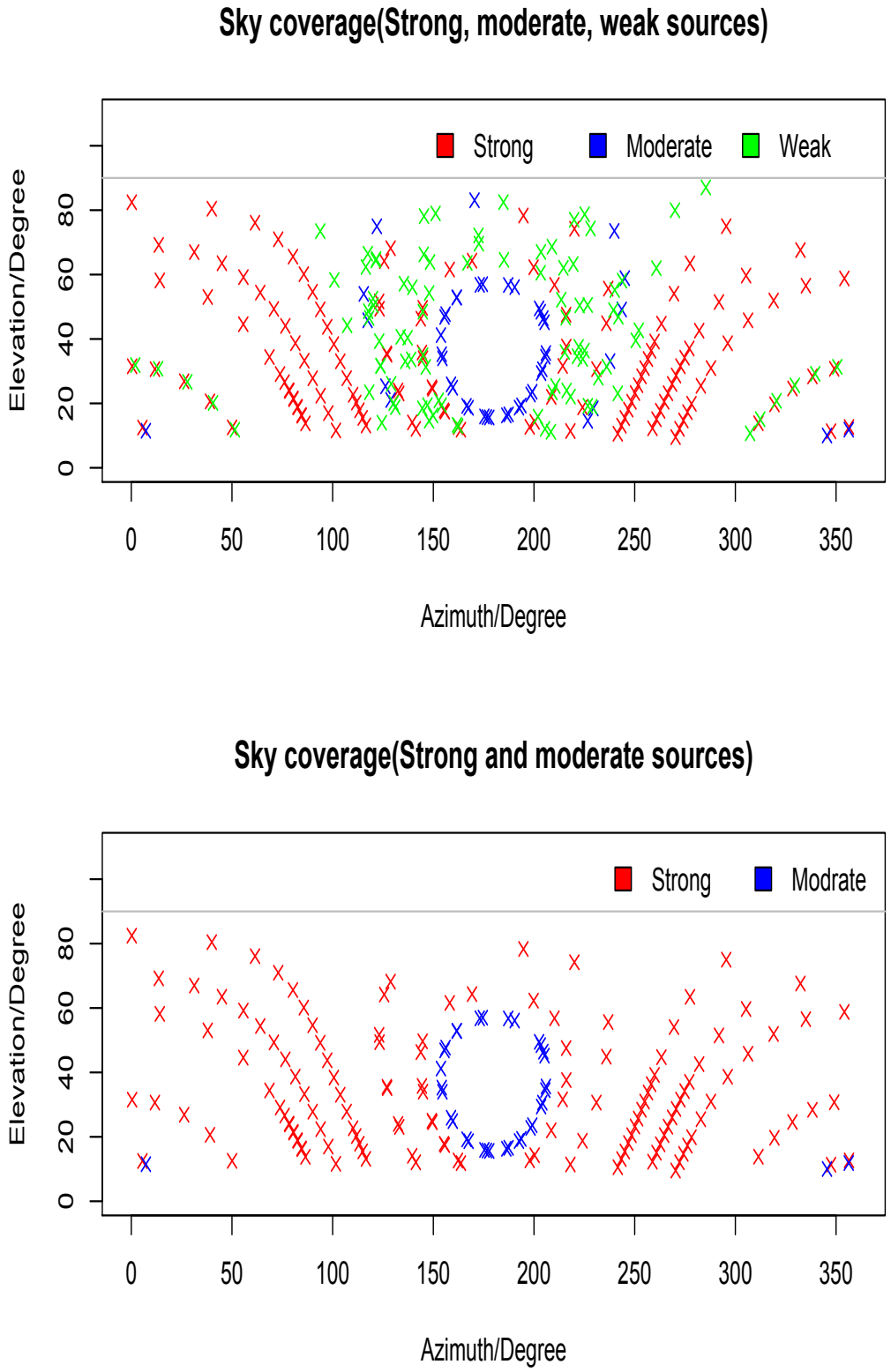

Figure 2.11: The plots shows the source distribution in the sky, in Azimuth and Elevation. The top plot includes all the sources, with the strong, moderate and weak sources represented in red, blue and green. The bottom plot excludes the weak sources for comparison. It seems that even without the weak sources, we still can get a good sky coverage.

2.2.1 Actual Offset (C-Band): Pointing Model Analysis

As mentioned earlier in the chapter, the current pointing model fails to address a sinusoidal pattern (in both Azimuth and Elevation), which adversely affects the pointing accuracy. The origin of the pattern is unknown, but with our knowledge and experience of the 30-metre antenna, we speculate the following as possible reasons:

- **Gravitational Deformation**: The 30-metre antenna was used for tracking geostationary satellites for over 30 years. Constant tracking at a fixed Elevation may have caused permanent deformation of the primary reflector. If that happens, the antenna beam will exhibit an offset of the RF axis and this will cause a systematic pattern in the offset database.

- **Tilting of the Sub-Reflector** as the dish moves in Elevation can cause a systematic pattern in the offsets. The sub-reflector with the supporting structure has significant weight and can slightly tilt as the antenna moves in Elevation. In that case, there will be a misalignment between the centres of the primary and secondary reflectors. The misalignment would be highest at low Elevation due to the weight distribution of the secondary reflector and the supporting structure on the primary reflector. This effect can create a systematic pattern in the pointing offsets with change in Elevation angle.

- **The 30-metre has a wheel on track construction.** In case of unevenness in the track at certain positions (rust, bending of structure due to age etc.), there could be a slight bump every time the telescope moves in Azimuth through that position. This can cause a slight shift in the RF-axis, and may cause a systematic pattern in both Azimuth and Elevation.

Investigating all of the above possible factors was outside the scope of our research, mostly due to time limitation. We only managed to study the surface of the main reflector to check for gravitational deformation. Our study did not find any

significant deformation of the surface. We will talk about the process (in detail) in Chapter 3.

Incidentally, we found out that the Effelsberg 100-m Radio Telescope in Germany had similar problem in Elevation [18]. They managed to successfully address the problem by using two additional terms (P_{19} and P_{20}) in the Elevation model. As discussed earlier, the FS pointing model allows up to thirty terms for various systematic pointing errors. The first nine terms (P1 to P9) are used for the common errors (discussed in Chapter 1), while the rest of the terms can be used to accommodate other systematic trends unique to individual telescopes. Since it worked for the Effelsberg telescope, we started by incorporating the two terms into the model:

$$\Delta Az = P_1 + P_3 \tan(El) - P_4 \sec(El) + P_5 \sin(Az) \tan(El) - P_6 \cos(Az) \tan(El) \tag{2.4}$$

$$\begin{aligned} \Delta El = {} & P_5 \cos(Az) + P_6 \sin(Az) + P_7 + P_8 \cos(El) \\ & + P_{19} \cos(8El) + P_{20} \sin(8El) + P_{23} \cot(El) \end{aligned} \tag{2.5}$$

Adding the two terms to our Elevation model worked for our antenna as well. The rms of the residuals in Azimuth and Elevation using the current model was 0.0154° and 0.0229°. Using our script, we processed the offsets using the new model (with P_{19} and P_{20}). The rms in Elevation offsets slightly improved from 0.0229° to 0.01949°, and the sinusoidal pattern in Elevation offset was suppressed. However, the rms in Azimuth offsets residuals virtually remained the same (0.0153°). Figure B1 to B4 (Appendix B) shows the plots produced after P_{20}, and both P_{19} and P_{20} were added to the model.

The magnitude of P_{19} and P_{20} were -0.0053 and -0.0236. Since the magnitude of P_{19} is negligible compared to P_{20} and other terms, we ran our script again without P_{19}. The sinusoidal pattern was still well addressed with only P_{20}, and the rms of the Elevation-offset residuals was 0.01950°, almost the same as when both P_{19} and P_{20} were used. It was important to limit the use of extra terms as much as possible so the model does not end up with an over fitting problem [19]. We finally settled on adding just P_{20} to the Elevation model.

As discussed in the previous section, the scatter in the offsets were significant. We processed the offsets again with the new model (i.e. with P_{20}) and only used the offsets from strong and moderate sources (discussed in section 2.2). The results improved significantly; the rms of the residuals in Elevation and Azimuth was 0.0085° (within 10% of the beam) and 0.0135°. The rms in the Azimuth offsets slightly improved, however still not within 10% of the FWHM. This was due to a sinusoidal pattern that still existed in the Azimuth residuals.

We speculate that the sinusoidal pattern in the Azimuth could be due to unevenness in the track of the 30-metre. Looking at the Azimuth residuals in Figure 2.7, the sinusoidal pattern has two periods, with a horizontal phase shift.

There are two ad-hoc (additional) terms for Azimuth in the FS to address wave like patterns in the Azimuth offsets. The terms are P_{17} (P_{17}cos(2Az)) and P_{18} (P_{18}sin(2Az)). Adding only P_{17} to the model lowers the rms to 0.0107° and adding only P_{18} lowered the rms to 0.0113°, both from 0.0135°. So adding only P_{18} gave slightly better result than P_{17}, however, the rms was still not within 10% of the FWHM. Figure B5 and B6 (Appendix B) shows the plots of the offsets in Azimuth (with residuals) with P_{17} and P_{18} added to the model.

When both P_{17} and P_{18} are added, the rms improved significantly to 0.0087°, which is within 10% of the FWHM. The combination of the two terms removed the phase offset in the residuals, which could not be resolved using a single term.

Figure 2.12 and 2.13 shows the final plots from our analysis. No visible pattern was observed in the residuals of Azimuth and Elevation offsets, and the rms of the offsets in both Azimuth and Elevation remained within 10% of the FWHM.

The final pointing model resulting from our analysis is:

$$\begin{aligned}\Delta Az = {} & P_1 + P_3\tan(El) - P_4\sec(El) + P_5\sin(Az)\tan(El) \\ & - P_6\cos(Az)\tan(El) + P_{17}\cos(2Az) + P_{18}\sin(2Az)\end{aligned} \tag{2.6}$$

$$\Delta El = P_5\cos(Az) + P_6\sin(Az) + P_7 + P_8\cos(El) + P_{20}\sin(8El) + P_{23}\cot(El) \tag{2.7}$$

where P_{17}, P_{18} and P_{20} were the three new terms added to the existing pointing model.

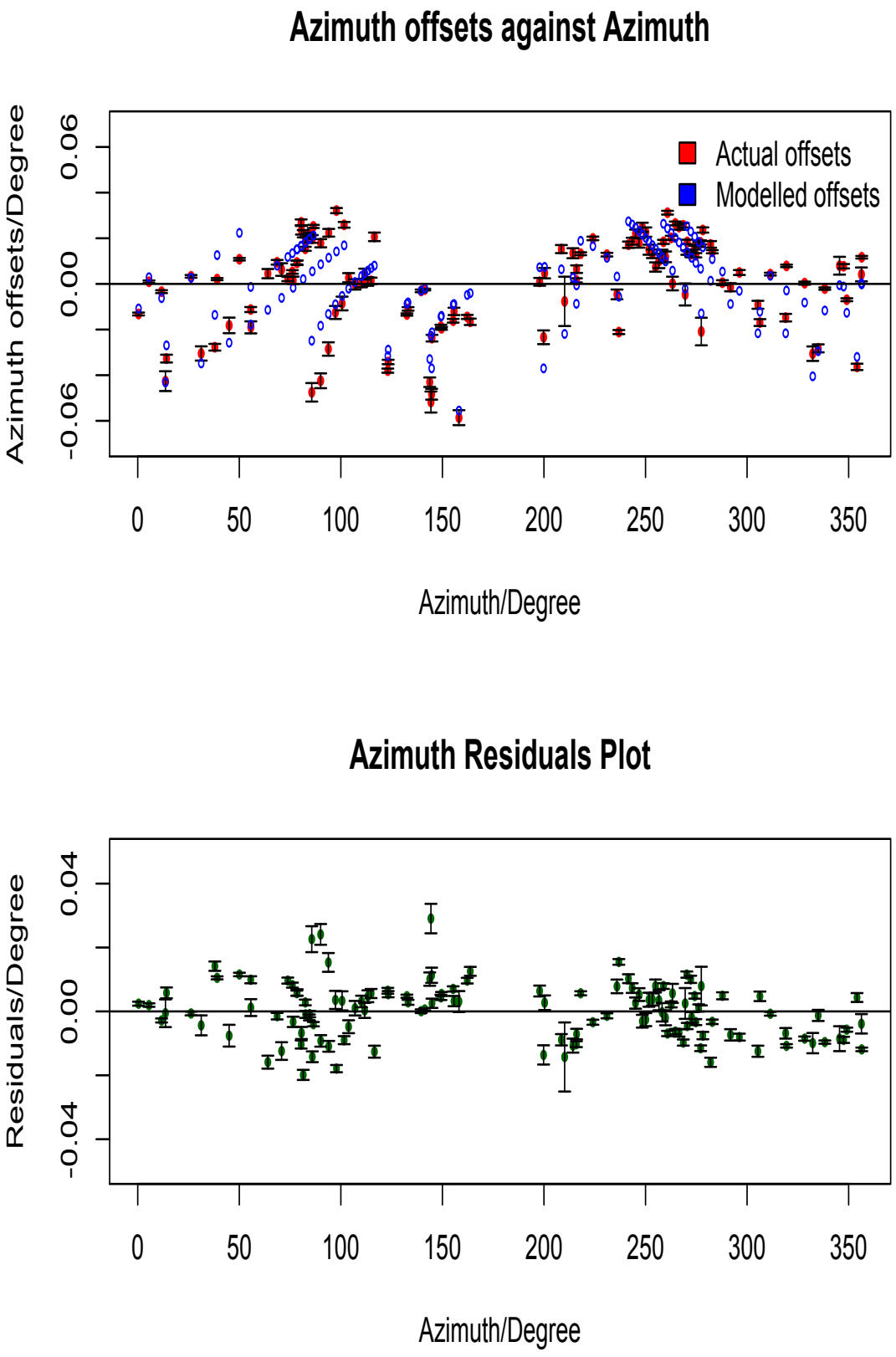

Figure 2.12: The Azimuth offsets plotted against Azimuth with the new model. After adding P_{17} and P_{18} to the Azimuth model, no sinusoidal pattern was observed in the residuals of the Azimuth offset (bottom plot) and the rms significantly decreased to 0.0087° and is within 10% of the FWHM.

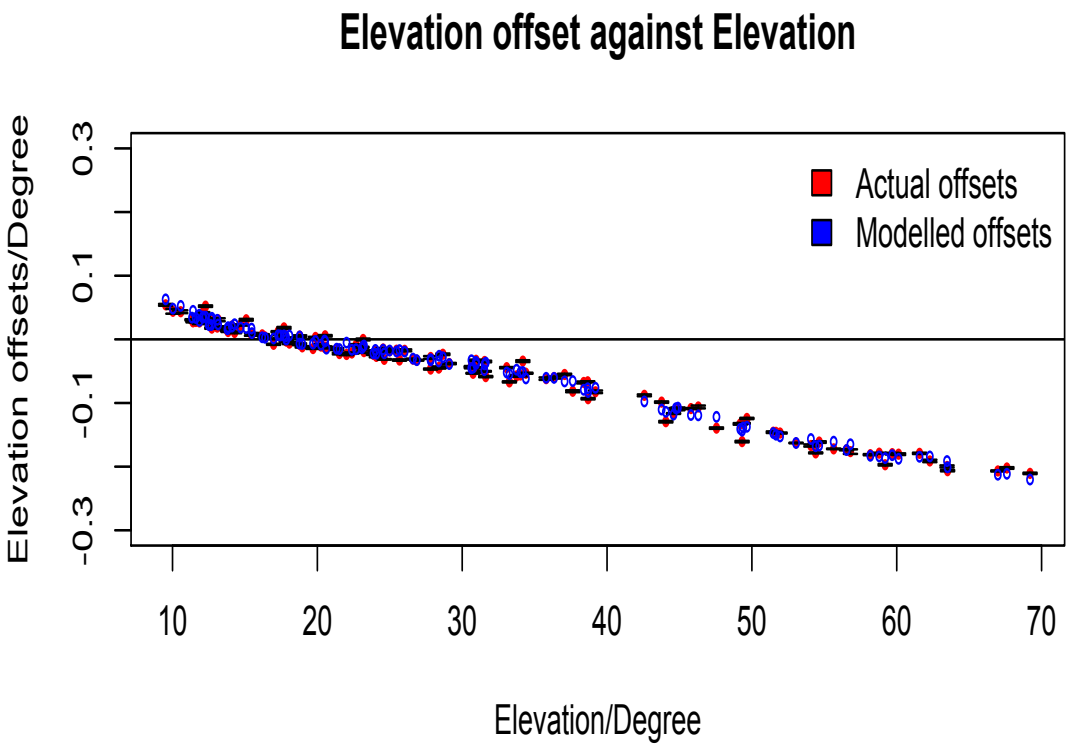

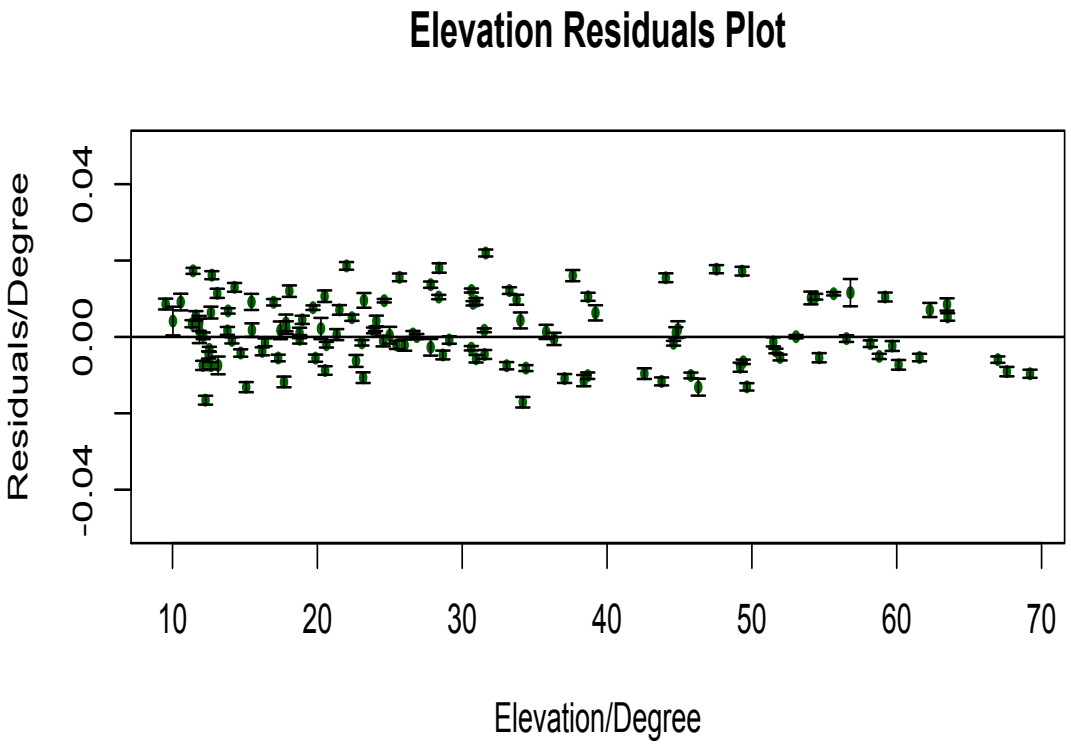

Figure 2.13: The Elevation offsets plotted against Elevation with the new model. After adding P_{20} to the Elevation model, no sinsusoidal pattern was observed in the residuals of the Elevation offset (bottom plot) and the rms significantly decreased to 0.0089° and is within 10% of the FWHM.

Table 2.3 shows the magnitude of the coefficient for each term.

Table 2.3: Table 2.3 shows the magnitude of the terms from the new model. The values from the old model is provided as well for comparison.

Terms	**Coefficient(old Model)**	**Coefficient(new model)**	(±)**Standard Error(Deg.)**
P_1	-0.042	-0.0099	0.012
P_3	-0.073	-0.0457	0.010
P_4	-0.072	-0.0305	0.149
P_5	-0.005	-0.0055	0.001
P_6	-0.002	-0.0039	0.008
P_7	-0.342	-0.3304	0.007
P_8	0.312	0.2849	0.012
P_{17}	N/A	-0.0111	0.001
P_{18}	N/A	0.0098	0.001
P_{20}	N/A	-0.0107	0.002
P_{23}	0.015	0.0202	0.002

The pointing model used for a telescope is never final, the terms must be updated from time to time by running new pointing observations using the existing model. This is mainly important for two reasons:

- To ensure that there has been no serious degradation in the pointing since last time.

- Use the offsets generated to improve the precision and reduce the overall standard error of the model.

To theoretically ensure that the new methodology works well, we tested the model with various pointing datasets. This included offsets that were collected using the existing standard 9 term model (column 2 in the above table) running in the background. Table 2.4 shows the results after the pointing methodology was applied to pointing offsets collected in C-band (6.7 GHz) and X-band (8.2 GHz). We use the term "pointing methodology" as the whole process involves the source selection, outliers removal and incorporating additional terms to the pointing model.

Table 2.4: The table shows the effect on the residual offsets rms after the new pointing model was applied to three different pointing databases. Column 2, (Background model used) states whether the offsets on which the new pointing methodology applied was collected using an existing pointing model. The results improved significantly in all cases.

Observed Frequency	**Background model used**	**RMS Before Az & El, Deg**	**RMS After Az & El, Deg**
6.7 GHz	None	0.020 & 0.090	0.008 & 0.008
6.7 GHz	Yes	0.014 & 0.014	0.009 & 0.009
8.2 GHz	Yes	0.025 & 0.022	0.006 & 0.009

Table 2.4 shows the rms of the residual offsets before and after the pointing methodology was applied. The first row shows the results from our analysis done with the actual offset throughout Chapter 2 (for comparison). The second row shows the comparison of the rms (of the residuals) before and after the new pointing methodology was applied on a pointing dataset that was collected with an existing 9 term model (running in the background) at 6.7 GHz. The rms of the offsets even after collecting with a model was more than the prescribed 10% of the beam. However, once we applied our new pointing methodology, the rms dropped significantly to 0.009° in both Azimuth and Elevation. Appendix B (Figure B.7 and B.8) shows the relevant plots to the analysis.

Similarly, the third row in Table 2.4 shows the comparison before and after the new pointing methodology was applied on a pointing dataset that was collected using an existing 9 term model in X-band (8.2 GHz, angular resolution: 0.09°). The rms of the collected offsets in Azimuth and Elevation was 0.025° and 0.022°. After applying the source selection and outlier removal procedure, the rms dropped to 0.0089° (Azimuth) and 0.0167° (Elevation). The rms further dropped to 0.0062° (in Azimuth) and 0.009° (in Elevation) after applying the modified model.

In conclusion, our new pointing methodology works well. As explained above, the new methodology has been rigorously tested under all possible conditions with various pointing datasets (only three shown in Table 2.4), and the results

significantly improved in all cases. The rms of the residual offsets stayed within 10% of the FWHM.

Chapter 3

Analysis of the Surface Quality of the Main Reflector

The surface quality of a reflector is a very important limiting factor, especially for high frequency observation [20]. Popular methods for surveying the surface include photogrammetry [21] and holography [20]. Holographic measurement often uses a reference antenna and a geostationary satellite beacon as a source to obtain samples of the complex antenna pattern. The results are processed to derive the phase components of the complex reflector surface current distribution and from this, an image of the surface deviations may be calculated.

Photogrammetry requires using camera(s) to take close-range pictures of the antenna from multiple positions to create a three-dimensional point cloud using triangulation. The physical process requires significant time and work as personnel with camera, tripod and miscellaneous equipments need to access different position on the antenna surface.

We did not have the equipment to perform holography and photogrammetry was relatively expensive and difficult to perform compared to a laser scan. Photogrammetry was tried before on the 12 m antenna in Warkworth but proved problematic

due to weather conditions. During the daytime, scattered sunlight off the reflector's surface created problems. In the evening around twilight, early dew created similar problems.

The laser scanning method to survey radio telescopes is new and to our knowledge was applied in radio astronomy on only a few occasions. However, due to rapid improvement in laser technology and the ease of using the scanner, it was heavily preferred over the other methods for this survey. The process is discussed in the following section.

As mentioned in Chapter 1, previous study suggested the overall rms of the surface of the main reflector (at 6° Elevation) was 3.5 mm. A sinusoidal pattern was also observed in the vertical cross section at 6° Elevation. In this thesis, using the same methodology previously used at 6° Elevation, we measured the surface accuracy of the main reflector at different Elevations to investigate any gravitational deformation (whether the sinusoidal pattern is observed at different Elevation) and it's effect (if any) on pointing. This chapter explains the physical surface scanning process, the data processing and presents the results from our analysis.

3.1 Surface Scanning

Synergy Positioning Systems conducted two sets of laser scanning of the 30-metre main and secondary reflectors in late February 2016 and mid May 2016. Jeremy Neilson and Cody Hughes from Synergy, along with IRASR staff (my supervisor Tim Natusch, Lewis Woodburn) and I facilitated the process. A FARO Focus 3D laser scanner was used for the scanning. The scanner weighed 5 kg, with a distance accuracy of (±) 2 mm for any single measurement and an operating range from 0.6 mm up to 120 m. The scanner is mainly used for detailing and documentation of large objects, spaces and buildings.

Once scanning parameters are set and the scanning process is initiated, the scanner steadily takes a 360° sweep and scans the surroundings (everything within it's

range). Using a laser beam, the scanner measures the distance of the object and together with the devices rotation angle data, determines the coordinates in space. Several millions of such 3D coordinates result in a complete 3D impression of the surface surroundings. The integrated high-resolution (70 mega-pixel) digital camera takes a photo realistic colour scan at the same time.

Figure 3.1: The FARO Laser Scanner used for the laser scanning

Figure 3.2: A sideview of the scanner, showing the touchscreen display

To investigate the gravitational deformation of the surface, we intended to scan the surface of the main reflector at 10° Elevation steps. The following procedures were taken to set up the physical scanning process:

- The scanner was mounted on the main reflector beside the surface access hatch, which is roughly 10 m from the centre of the main reflector.

- Access to the main reflector with the stairs is only possible when the main reflector is positioned horizontally, i.e. at 90° Elevation. Because we wanted to scan at every 10° of Elevation, we had to operate the scanner remotely.

- The scanner can be operated remotely from a laptop via a Bluetooth connection. However, the range of a typical Bluetooth connection is only up

to 10 m, far less than what was required. The closest point from which the scanner can be remotely operated was roughly 40 m.

- Two laptops were used to get around the problem. A laptop was mounted on the main reflector next to the scanner that connected to the scanner via Bluetooth. Since the observatory has no WIFI connection, the laptop on the main reflector was connected with another laptop on the ground using a long Cat5 cable running down the hatch. Using TeamViewer remote access software, the scanner was operated from the ground using the laptop.

A total of eleven scans were conducted, with nine measurements taken every 10° from 10° to 90° Elevation. Two measurements were repeated at 50° and 90° for cross checking, and another measurement was taken by placing the scanner at the centre of the main reflector (90° Elevation).

A second round of scans were also conducted from the roof of the Radio Telescope building for lower Elevation angles. While processing data from the first scans done in February 2016, we discovered a mismatch between the start and end of the scans that created discontinuity in the data. Figure 3.2 shows results of a scan that was done at an Elevation of 10° with the faulty scanner. It was an internal fault caused due to a misalignment in the rotating mirrors of that particular scanner. There was a centimetre jump in the data on the scanner x-axis (i.e. scan starting and ending position). This made the raw data unsuitable for our analysis, as we were looking for millimetre accuracy. Further details on how Figure 3.3 were produced are given in next section (Analysis).

On reporting the issue to Synergy, they applied compensation to the raw scan data, which worked well and is demonstrated in Figure 3.7, 3.8 and 3.9 where unlike Figure 3.3, no discontinuity in the contours are visible. However, we decided to conduct a couple of scans from the roof using a good scanner so we can compare the result with the previous scans at the same Elevation. This was to ensure that the compensation applied did not suppress any significant findings from the scan which otherwise would have shown if the scan was conducted with a non-faulty scanner. More details are described in analysis section.

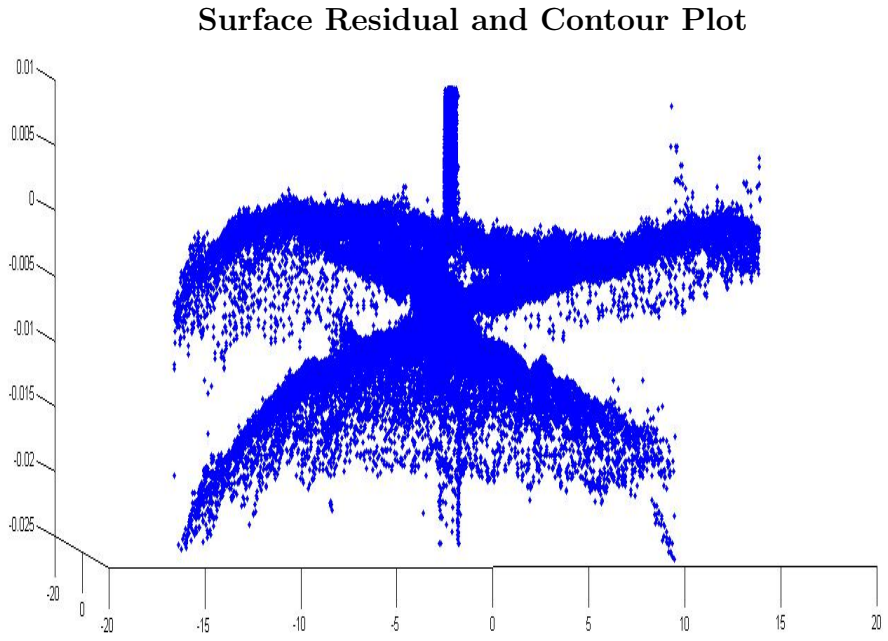

(a)

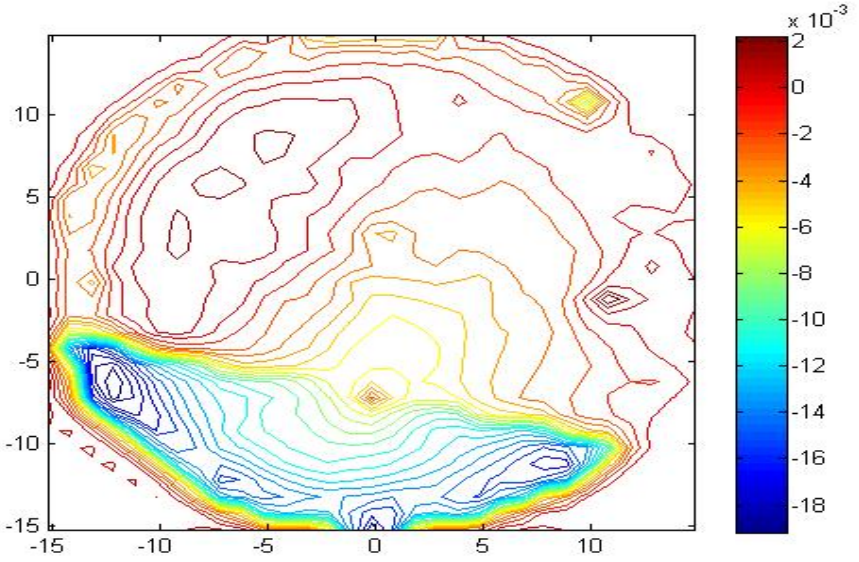

(b)

Figure 3.3: (a) Shows the discontinuity or the break in the surface residual plot. There is a significant (more than a cm) jump in the data. This is clearly visible in (b) the contour plot. The units of both plots are in metre.

Figure 3.4: Jeremy from Synergy setting up the scanner on the roof of the 30-metre telescope building. This scanner was an updated version of the previous scanner used, and had an operating range from 0.6 mm up to 320 m.

Unlike the scans done from inside of the main reflector that required setup for remote operation, the scanning conducted from the roof was done with minimal effort. Since no remote operations were required, all we had to do was mount the scanner on a tripod and level the instrument. Four scans were done at 10°, 20°, 30° and 35° Elevation. Here 35° was the highest Elevation of the full main reflector that could be covered from the edge of the roof.

3.2 Data Processing

Data collected were cleaned and processed using an industry standard data cloud processing software called SCENE (version 5.2). An external SD memory card in the scanner stores the raw scans in Faro Laser Scanner (.fls) format, and is automatically detected and imported by SCENE. The imported raw scans were

preprocessed using the "Preprocessing Scans" tool that filters and creates scan point clouds for quicker visualization (in SCENE).

Since the scanner sweeps 360° and surveys everything within its range, significant cleaning of unnecessary points and unrelated point clouds was required. Figure 3.5 shows a panoramic colour scan of the main reflector, with the scanner placed at three different positions.

For this research, we were only interested in investigating the gravitational deformation of the main reflector surface. Using the clipping tool in SCENE, the following structures were removed from the scans:

- The sub-reflector and it's supporting structures (the legs).
- The central opening of the telescope beam waveguide.
- The hatch, which was open during some scans.
- Outside structures picked up during the scan, for example trees, buildings and fences.

Figure 3.5 gives a representation of the overall data cleaning process. Since we are looking for millimetre accuracy, it was important to clean in great detail, as outliers might result in an incorrect fit to the theoretical surface. The next section discusses the analysis of the surface of the main reflector conducted with the processed data.

3.3 Analysis

For data analysis, a program written in Matlab was used that fits a theoretical shaped paraboloid to the data (point cloud) of the main reflector [Gulyaev, private communication, 2016]. Christophe Granet, currently at Lyrebird Antenna Research computed and provided the theoretical shape for the main reflector (30-metre) when the first study was done back in 2013 [11].

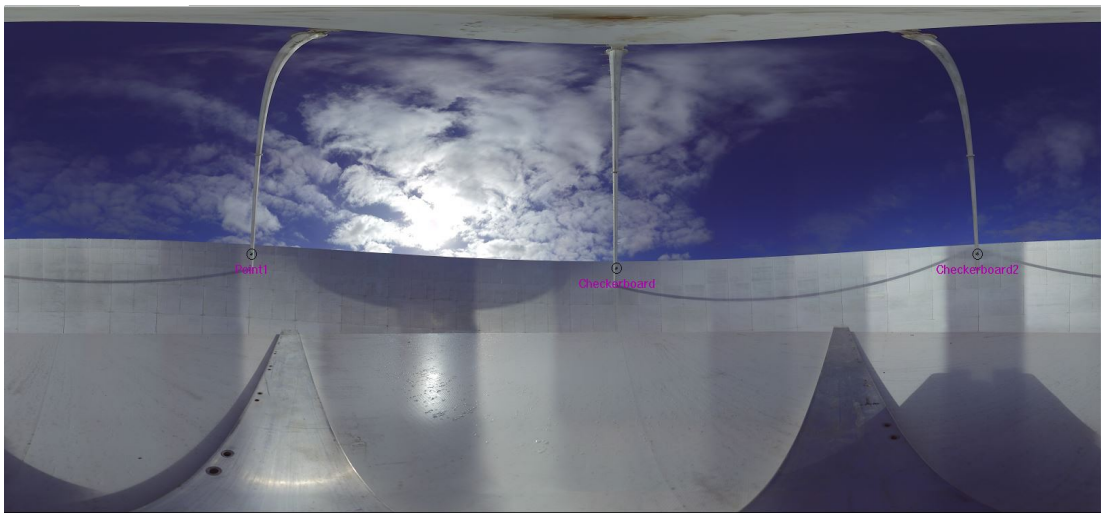

(a)

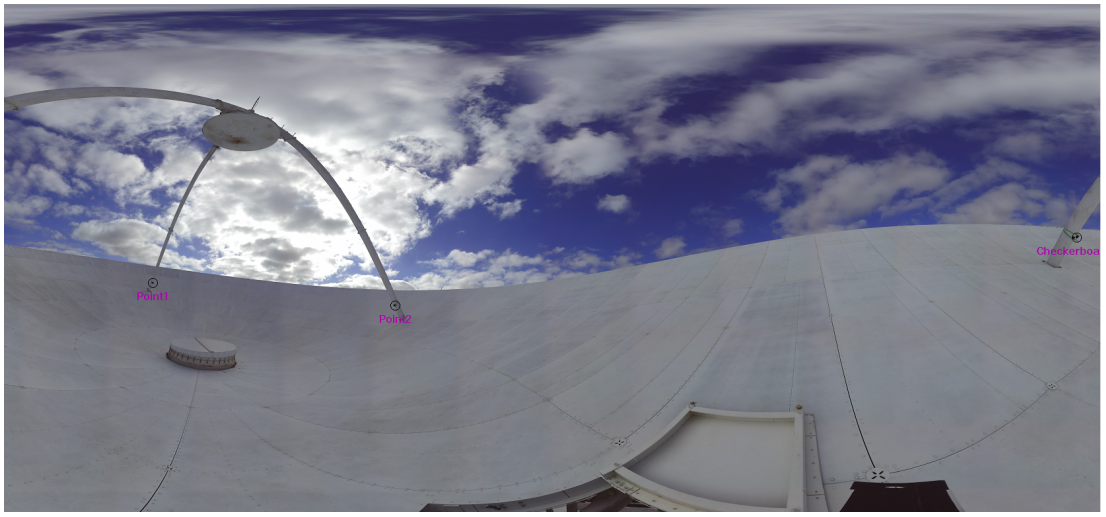

(b)

(c)

Figure 3.5: Panaroma of the scans with the scanner in three different positions: (a) from the centre of the main reflector (b) near the hatch (∼10m to the right of the centre), (c) From the roof of the building. For (a) and (b), the camera of the scanner was turned on, creating a colour scan. The position from where the scans are conducted can signficantly affect the distribution of the point cloud. Details are explained later in the chapter.

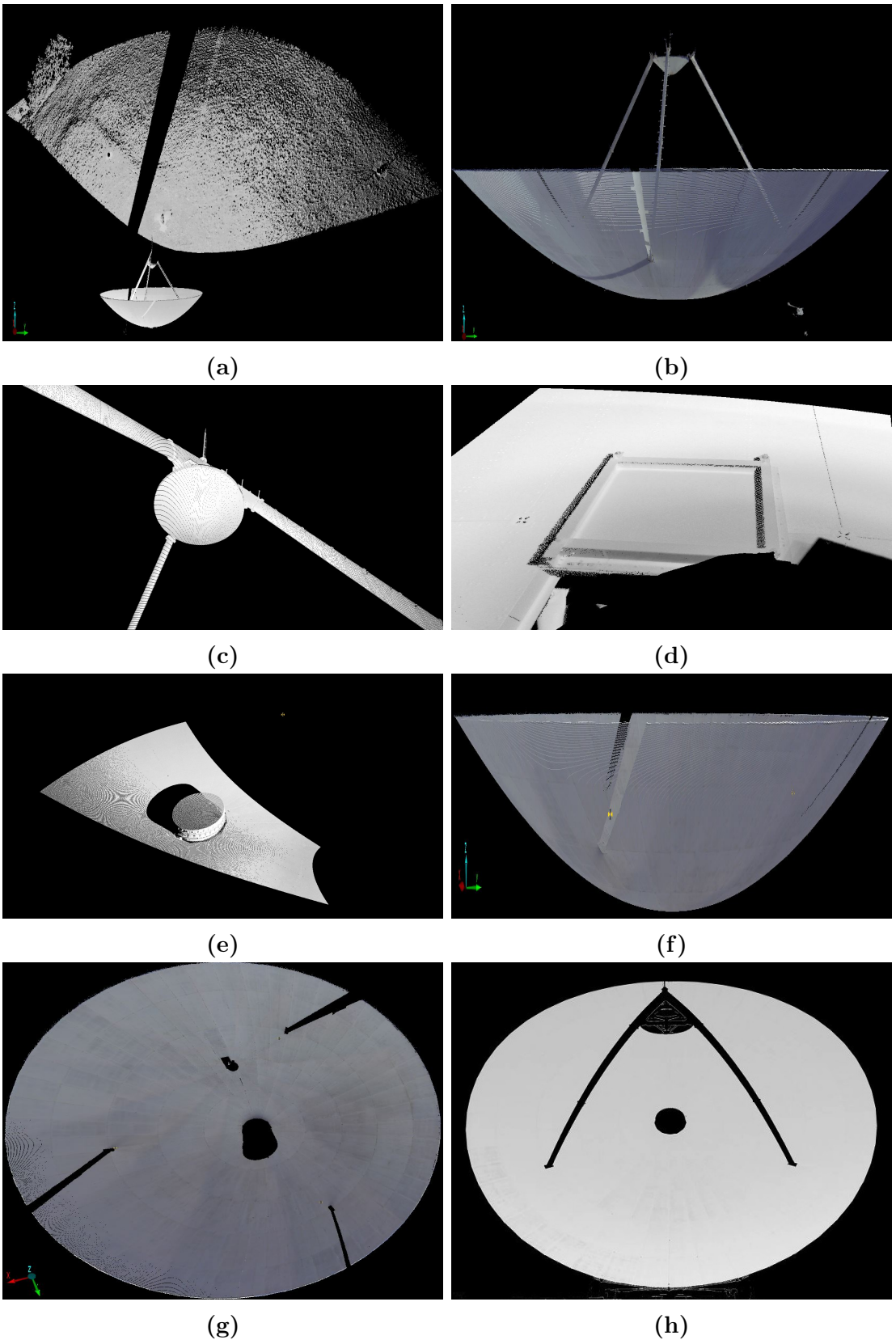

Figure 3.6: Plots representing the overall cleaning process using SCENE. (a) A raw point cloud from the main reflector: The scanner also picks up the surroundings. Figure (b), (c), (d) and (e) shows the overall cleaning process in steps. Figure (b) shows the surroundings (fields and trees) removed, (c) shows the secondary reflector inclduing its supporting structure, (d) shows the open hatch and (e) the central opening of the telescope beam waveguide, all of which was removed. Figure (f) shows the cleaned main reflector, (g) gives a top view (open hatch and the central opening of the beamguide removed) and (h) shows one of the cleaned scans done from the roof.

To ensure proper fitting, we had to translate and align the centre of the point cloud with the theoretical centre of the main reflector. The first step was to rotate the point cloud around the z-axis so that the x and y-axis of the theoretical surface and the point cloud were aligned.

The initial value of the rotation angle (around the z-axis) was estimated by looking at the orientation of the point cloud. We guessed the rotation angle by looking at the position of the hatch, which sits on the theoretical x-axis of the main reflector.

Once the main reflector point cloud was rotated and the x and y-axes were aligned, the cloud was then turned around the x-axis. The initial turning value was again estimated by taking (in to consideration) the position of the scanner. For scans done from inside the main reflector, the initial turning angle was very small. The angle does not need to be very accurate, as the program turns and adjusts the point cloud around the x-axis until the turning angle becomes very small (of the order of 5 x 10^{-7} degrees). The reason for choosing this particular value is as follows:

Since we are looking for millimetre accuracy, the angle created due to 1 mm deviation of the theoretical shape and the point cloud at a distance of 15 m (radius of the main reflector) can be approximated by:

$$\theta \approx \frac{1mm}{15000mm} \approx 7 \times 10^{-5} rad \tag{3.1}$$

Converting the value to degrees from radian gives $\sim 4 \times 10^{-3}$ degrees. For better accuracy, we artibarily chose 5 x 10^{-7} degrees, which is higher than 4×10^{-3}. We tried different values as well and as long as the threshold was more than θ (4×10^{-3} degrees), no significant changes in the results were observed.

The program then follows the same procedure, and turns the cloud around the y-axis. Like the x-axis, we need to specify the initial turning angle. The program then iterates and adjust the turning until the angle becomes of order 5 x 10^{-7}degrees.

The turning in the y-axis can create a slight shift in the previously adjusted x-axis, and adjusting the x-axis again in turn can create a slight shift in the y-axis. So the program keeps adjusting both x and y-axis until the turning angle becomes of order 5×10^{-7} degrees for both axes.

The residuals were calculated by measuring the shortest distance between each point and the theoretical surface. This was achieved by finding the derivative at each point ($\tan\theta$), and then correcting the differential in z by dividing it with $\sqrt{1 + \tan^2\theta}$. Figure 3.7 shows the deviation of the observed surface (at Elevation 90°) from the theoretical surface after performing the above procedure.

Due to the position of the scanner, there will be always some inhomogeneity in the distribution of the point cloud. Higher density of points will be observed closer to the scanner and can create a non-uniform distribution of the point cloud. Take for example the scans done from the roof; due to the tilt of the main reflector at 10° Elevation, the lower end of the main reflector will be relatively closer to the scanner than the higher end. So the density of points will be slightly higher in the lower end. For scans conducted from the centre of the main reflector, the non-uniformity will be minimized, as the density of the points will change radially with distance from the centre.

To counter this inhomogeneity (non-regular distribution), one solution could be computing the standard deviation of the surface using a regular mesh of points. The size of the mesh was varied from 1mm to 1 m and the standard deviation of the surface was computed for the scan done back in 2013 at 6° Elevation [11]. The standard deviation remained virtually unchanged (only changed at 4^{th} decimal places). So the inhomogeneity of the distribution may not after all have a significant effect on estimating the standard deviation of the surface. However, for in depth analysis of the main reflector (not conducted in this research), the effects can be significant. Further investigation is required and will be discussed in the next chapter (Further works).

Using Matlab, all the scans done at 10° Elevation steps (10° to 90°), conducted from inside the main reflector, and also from the roof (of the building) were processed. No significant deformation was observed at any Elevation. Instead of presenting the analysis and plots for all the scans (which were more or less the same), only the results from the scans conducted at 90° (from the centre), 60° (from near the hatch) and 10° (from the roof of the building) Elevation are presented. We particularly chose these three scans as they are taken from three different positions at different elevation angles, and are adequate to summarize and present the overall analysis.

Figure 3.7 presents the plots from the analysis of the surface scan at 90° Elevation, with the scanner positioned at the centre of the main reflector. The total RMS (standard deviation) of the surface residuals in x and y cross section (Figure 3.7: c & d) was 2.8 mm and 3.0 mm respectively. No significant pattern/deformation was observed, and the RMS of the overall surface was 3.25 mm.

Similar to Figure 3.7, Figure 3.8 presents the plots from the analysis of the surface scan at 60° Elevation, with the scanner positioned near the hatch of the main reflector. The hatch is approximately at (+)10 m along the x-axis of the main reflector (Figure 3.8a).

Comparing the contours in Figure 3.7 (a & b) and 3.8 (a & b) gives us some idea about the effect on the distribution of the points depending on the position of the scanner. With the scanner at the centre (Figure 3.7(a & b)), the highest variation was observed around the centre (of the main reflector) and somewhat decreased radially towards the edge. In Figure (3.8 a & b), high variation was observed on the left of the main reflector. This was due to the position of the scanner to the right from the centre of the main reflector (near the hatch), which contributes to the higher density of points in one side. However, it doesn't significantly affect the result as the RMS of the overall surface remains almost the same as in 90°, 3.23 mm. The RMS of the x and y cross-sections was 2.8 mm and 2.6 mm respectively.

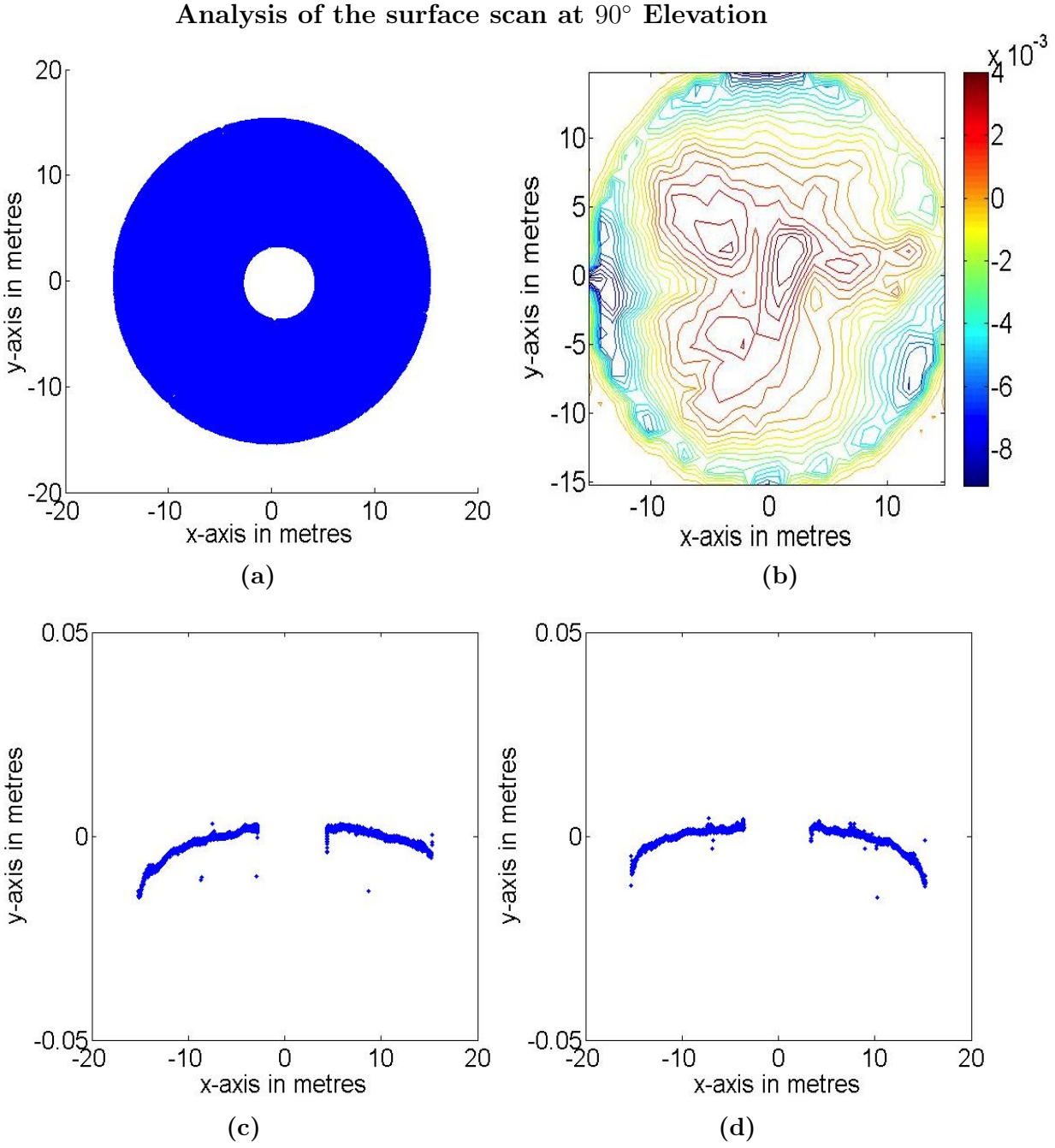

Figure 3.7: Analysis of the surface scan at 90° Elevation, with the scanner positioned at the centre of the main reflector. Figure (a) shows the orientation of the surface after the rotation was applied around z-axis and turning were applied around x and y axis. Figure (b) shows the contour map of the deviation of the observed surface from the theoretical shape. The colour bar, x and y-axis are in metre. The variation is relatively high in the centre, due to missing data (the central opening was removed), as shown in (a). The variation looked uniform, and decreases in somewhat circular manner from the centre towards the edge. No unnatural variation is observed in either x or y axis. Plot (c) and (d) shows a slice (cross section) through the antenna centre and plot for the z-x (horizontal) and z-y (vertical) axis. No significant pattern is observed. The RMS of the residuals in x and y direction of the above cross-sections were 2.8 mm and 3.0 mm. There deviation is slightly higher near edge for both cross-sections. The RMS of the whole surface was 3.25 mm. The scan that was done at 90° Elevation from the hatch also gave very similar results.

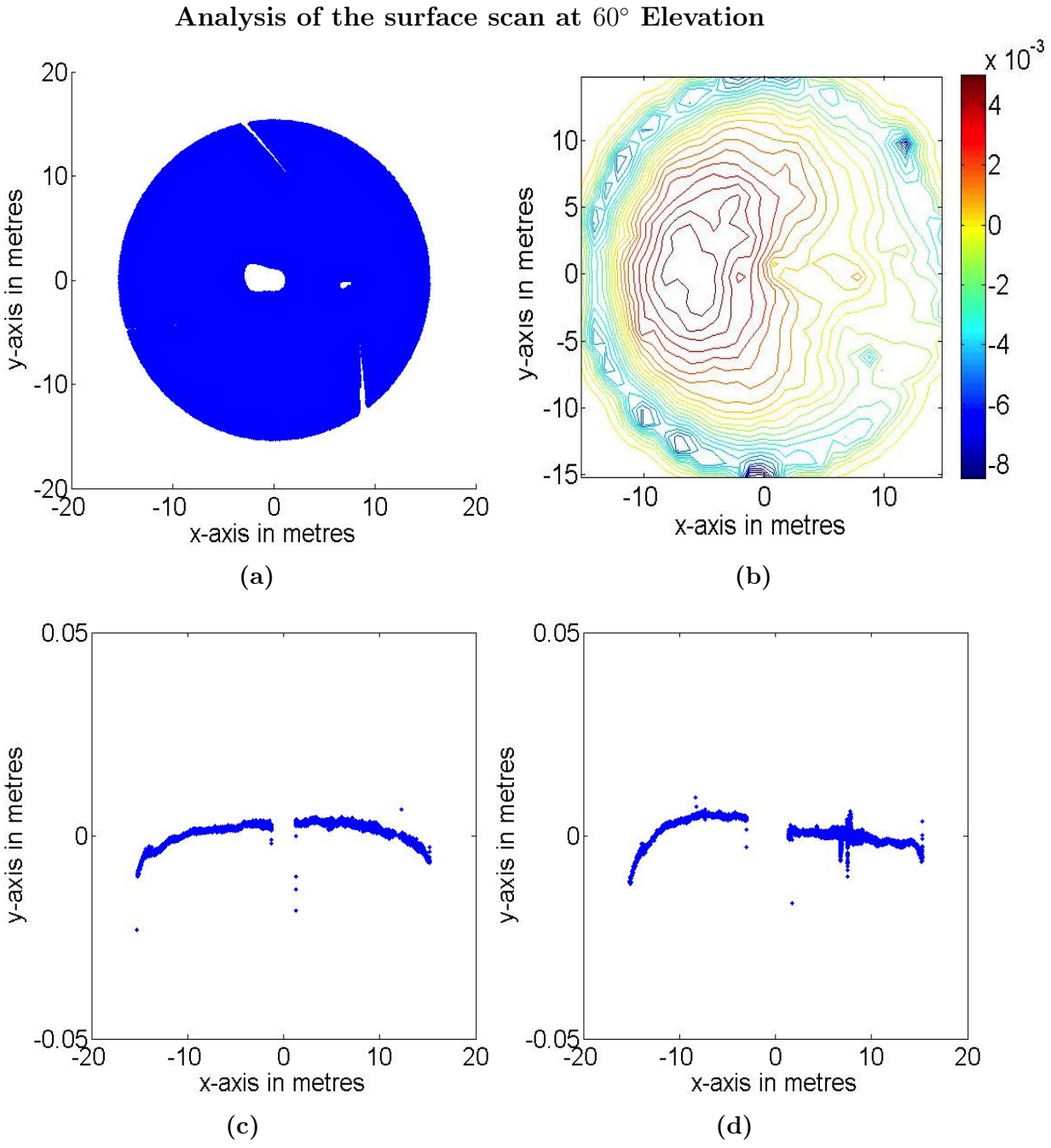

Figure 3.8: Analysis of the surface scan at 60° Elevation, with the scanner positioned near the hatch of the main reflector. Figure (a) shows the orientation of the surface after the rotation was applied around z-axis and turning were applied around x and y axis. Figure (b) shows the contour map of the deviation of the observed surface from the theoretical shape. The colour bar, x and y-axis are in metres. The variation was relatively high on the left of the main reflector, due to missing data (the central opening of the beam waveguide was removed), as shown in (a). No systematic variation is observed in either x or y axis. Plot (c) and (d) shows a slice (cross section) through the antenna centre and plot for the z-x (horizontal) and z-y (vertical) axis. The RMS of the residuals in x and y direction of the above cross-sections were 2.8 mm and 2.6 mm. The RMS of the whole surface was 3.23 mm.

Figure 3.9 presents the analysis of the surface scan at 10° Elevation conducted from the roof of the building. Results were similar to the previous analysis. The RMS of the residuals in both x and y cross-sections (Figure 3.9 c& d) was 2.6 mm.

According to the Ruze equation [22], the shortest wavelength at which a telescope works reasonably well is:

$$\sigma \approx \frac{\lambda}{16} \tag{3.2}$$

where λ is the observed wavelength and σ is the threshold above which, significant reduction in the effeciency of the reflector surface is expected.

The 30 m telescope operates at 6.7 GHz, which translates to 44.75 mm in wavelength. Using the above equation, the surface deviation threshold is ∼2.80 mm, slightly smaller than ∼3 mm estimated from our work. The surface quality seems to be reasonable, considering the standard error of the residuals for all the scans were around (±) 0.02 mm. However the surface will need improvement for higher frequency observation.

The results from our analysis did not show any gravitational deformation of the surface. For all the scans conducted between 10° and 90° Elevation, the RMS of the surface residuals virtually remained the same (∼3.00 mm). Although previous result suggested a possible gravitational deformation on the vertical cross section at 6° Elevation, our current result does not confirm this conclusion. For this research, we did not manage to repeat a scan at 6° Elevation. However as our current analysis shows, at 10° Elevation, no significant deformation is observed. It is unlikely that significant deformation will happen within 4°, so we speculate that inadequate cleaning of the point cloud at 6° Elevation from the 2013 survey might have caused improper fitting and produced the sinusoidal pattern in the vertical cross section. However, even if the deformation observed was real, it happens at a very low Elevation and is not permanent. We plan to investigate this further in the future.

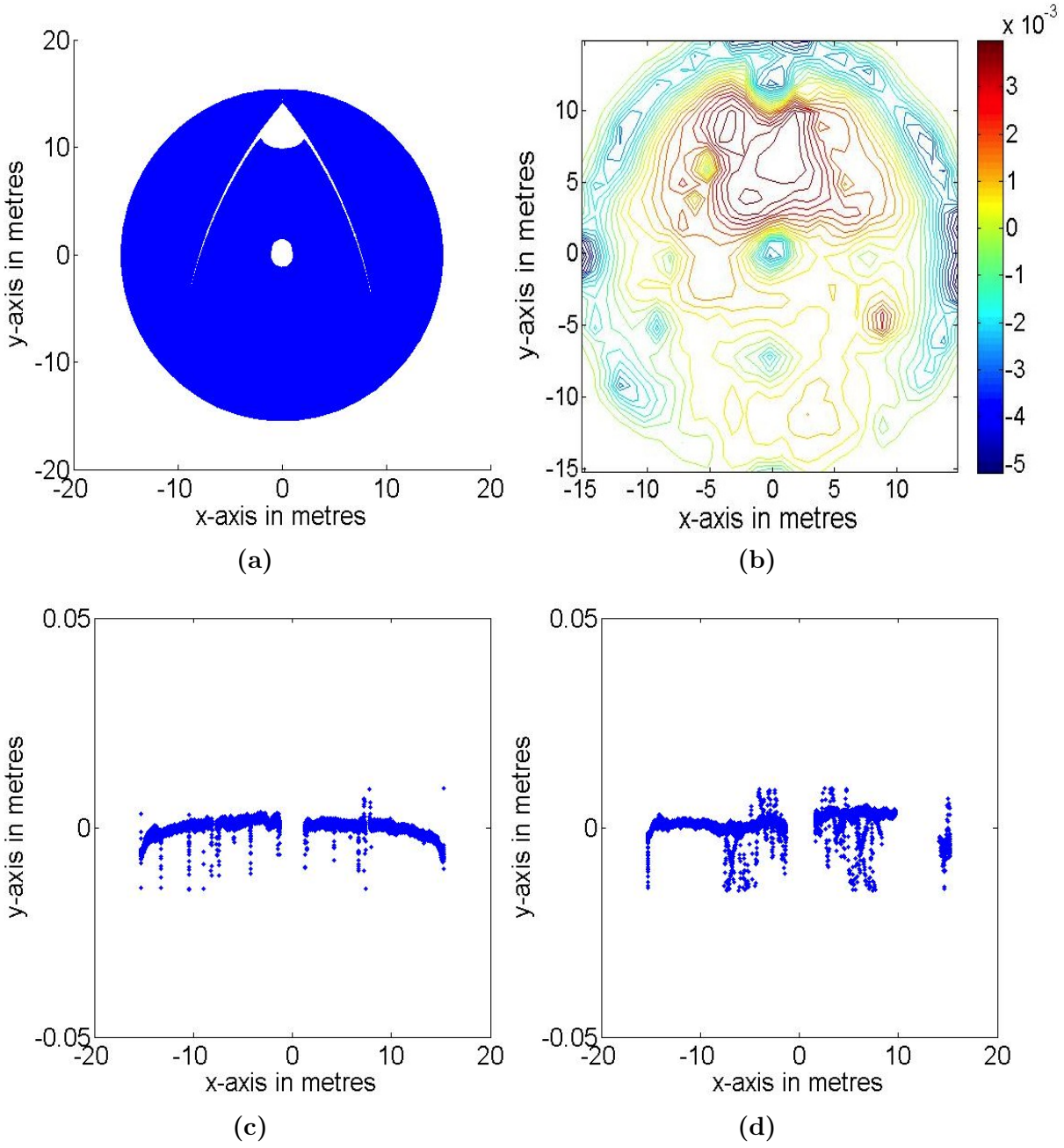

Figure 3.9: Analysis of the surface scan at 10° Elevation conducted from the roof. Figure (a) shows the orientation of the surface after the rotation was applied around z-axis and turning were applied around x and y axis. Figure (b) shows the contour map of the deviation of the observed surface from the theoretical shape. The colour bar, x and y-axis are in metres. The variation is relatively high above the centre of the main reflector. This is because of the missing data in that area due to the shadow formed by the sub-reflector and it's leg, as shown in (a). No systematic variation is observed in the contour. Plot (c) and (d) shows a slice (cross section) through the antenna centre and plot for the z-x (horizontal) and z-y (vertical) axis. No systematic pattern is observed. Significant scatter is the plot suggests that the quality of the cleaning can be improved. However it should not affect our analysis as the scatter is within a millimetre. The RMS of the residuals in both x and y direction of the above cross-sections was 2.6 mm. The RMS of the whole surface was 3.23 mm. The scan that was done at 10° Elevation from the hatch also gave similar results.

From our current analysis, we found no observational evidence of any gravitational deformation of the main reflector that could affect pointing, and the overall surface accuracy at different Elevations was satisfactory for current observation at 6.7 GHz.

Chapter 4

Discussion and Conclusion

The 30-metre radio telescope is a sensitive instrument and significantly expands New Zealand's capability in radio astronomy. With a large collecting area, the telescope is capable of significant single dish work and enhances the interferometric arrays it collaborates with, often being on the end of the longest baseline. It is very important to continually work and improve the efficiency of the instrument to be able to use it at its maximum capacity.

This research attempts to improve the current pointing efficiency of the telescope. Pointing accuracy is a very important limiting factor for successful observations. As explained in Chapter 1, a 0.1° of offset can significantly degrade the signal by 82%. Figure 4.1 shows a 13-step scan of Taurus A in Elevation, which also represents the beam of the 30-metre radio telescope. With the current 9 term pointing model, the observed source generally stays within 16% of the beam. However, with the new pointing methodology, the pointing accuracy improves significantly, and we can point the RF axis to within 10% of the beam width (FWHM).

To summarize our work with pointing, the new pointing methodology uses a script written in Bash command line to pre-process pointing offset data that we collect using the Field System pointing routine. A script written in R then removes outliers using a simple but effective (in this case) 1.5 IQR rule. We addressed

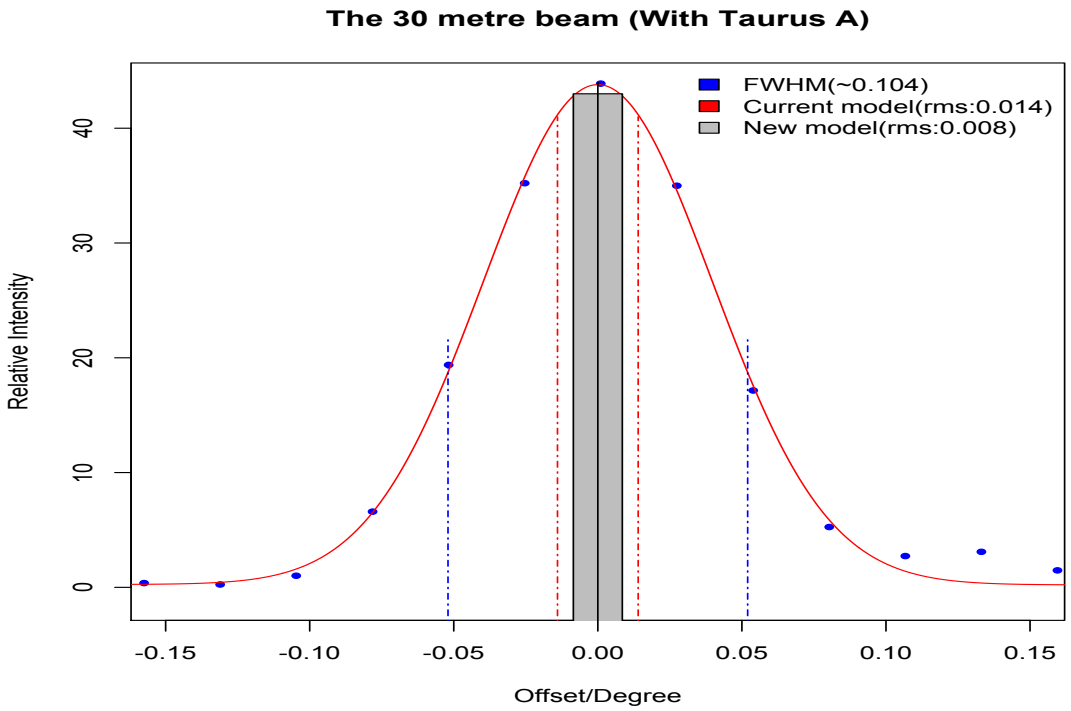

Figure 4.1: The beam of the 30-metre telescope represented using a scan of Taurus A in Elevation. The area inside the blue lines represents the FWHM at 6.7 GHz ($\sim 0.104°$). With the current pointing model, the source generally stay within ($\pm$) 0.014 (14%) of the beam, and is represented by the area bounded by the red lines. With the new model, the source will stay within ($\pm$) 0.008(7.6%) of the beam (inside the grey area).

the sinusoidal pattern (in Azimuth and Elevation) by introducing new additional terms. The pointing accuracy improved significantly, as explained in Figure 4.1.

We also introduced a source selection method that quantifies the quality of the sources by looking at the standard deviation of offsets and the overall dispersion in the offsets of the individual sources. This method can be effectively used to select suitable sources for pointing, reducing pointing observation time and the overall noise in the pointing database.

Our model has been rigorously tested with different pointing datasets and each time has shown improvement. We also compared our pointing methodology with another robust, well proven pointing methodology [17]. The same data were used to generate 8 terms using both methodologies, and the results (values of the terms) were nearly identical, also suggesting that our methodology works well.

We are yet to incorporate our new pointing model into the FS due to some technical issues. The current pointing routine by default uses some terms for pointing, and that interferes when we try to implement our model. We are in touch with Ed Himwich at NASA Goddard Space Flight Center about the issue and expect to resolve it soon.

We analyzed the surface of the main reflector using the laser scanning method to investigate gravitational deformation of the surface. We speculated that the sinusoidal pattern observed in Elevation pointing offset was due to gravitational deformation, which, we found out not to be the case from the study of the surface. Our 30-metre is not the only telescope with this problem. As discussed earlier, the 100 m Telescope in Effelsberg also observed a sinusoidal pattern in Elevation and used P_{19} and P_{20} to suppress the pattern. We contacted Uwe Bach at the Efflesberg in Germany about their investigation and solution to the problem. They haven't done any investigation for the origin of the pattern, but thought that it could be due to the weight balance on the Elevation axis that changes during the movement from zenith to horizon. A few other plausable reasons were also discussed in Chapter 2 (Sections: 2.1, Analysis).

We carried out laser scanning of the main reflector from three different positions: (i) From the centre of the main reflector, (ii) From near the hatch (10 metre on the right of the main reflector) (iii) From the roof of the building. Only one scan was possible from the centre at 90-degree Elevation, as there is no mount to hold the scanner. However, from our analysis, the best quality of data is achieved when the scanner is positioned at the centre. The scanner can then perform a radially symmetrical sweep of the main reflector, eliminating the chances of having significant bias in the point cloud distribution. The data cleaning process also becomes a lot easier as the deflection and scattering is minimal. This is reflected in Figures 3.7, 3.8 and 3.9 (c & d). When the scan was conducted from near the hatch, it needs to be left open (for the connecting Cat5 cable), and later needs to be removed from the cloud. The removal of the hatch, which contains a significant number of points, can also create significant bias in the distribution. However, as we discussed in Chapter 3, the data obtained from the

offset position of the hatch did not significantly affect our conclusion with regards to gravitational deformation. This effect would be significant for other detailed analysis, for instance to study the shift in position of the centre of the subreflector relative to the centre of the main reflector at different elevations.

We conclude the thesis by listing some potential future works that can be undertaken to further develop and enhance pointing and the surface scanning method of the 30-metre telescope.

4.1 Future Works

- The current pointing procedure is not real-time. Pointing data is gathered using the FS and then processed and analyzed using Pdplt. The values of the terms are then generated and updated in the FS. If the pointing offsets can be processed and the changes can be applied real-time in the model, the overall efficiency of the process can be improved significantly.

- A stable optical telescope mounted on the main reflector to observe point sources can be used for pointing model data acquisition. The angular resolution of an optical telescope is much smaller than that of its radio counterpart and the number of reference objects (point sources) is huge, hence more accurate measurements can be conducted. The tilt and offset for each telescope axis can be precisely measured, and other measurements such as the collimation terms and the flexure can be obtained from radio measurements. This process could enhance the accuracy of the model [23].

- The origin of the sinusoidal patterns are still to be uncovered. The current scan data, which also includes the scan of the subreflector, can be used to study the lateral shift (if any) of the subreflector with respect to the main reflector at different Elevations.

- However, as previously suggested, it would be better to use new set of scans done from the centre of the main reflector. This will also be the best position

to scan the sub reflector considering the subreflector will be right at the top of the scanner. The current scans done from near the hatch do not get a good view of the subreflector and will create some bias in the distribution.

- To scan from the centre at different Elevation, a structure with a mount has to be constructed to hold and support the scanner at the centre of the main reflector. A gimbal can be used as well to balance the movement of the scanner, providing better stability during the scan at different Elevations.

Bibliography

[1] A.R. Rasha, Auckland University of Technology. School of Computing, and Mathematical Sciences. *Statistical Analysis of the Pointing Model for AUT 30 Metre Radio Telescope: A Report Submitted in Fulfilment of the Requirements for the Degree of Bachelor of Science (Honours) in the School of Computer and Mathematical Sciences.* 2015.

[2] Aviad Agam and Ran Barkai. Not the brain alone: the nutritional potential of elephant heads in paleolithic sites. *Quaternary International*, 406:218–226, 2016.

[3] Universes in Universe, Sharjah Maritime Museum. The astrolabe, an ancient GPS, 2016. [Online; accessed March 01, 2016].

[4] W.E.Himwich. Pointing Model Derivation. In Space Geodesy Project, editor, *Pointing Model Derivation*, pages 4–5, 1993.

[5] F.Ghigo NRAO-Green Bank, WV. Karl Jansky and the Discovery of Cosmic Radio Waves. http://www.nrao.edu/whatisra/hist_jansky.shtml, 2008.

[6] NASA (original); SVG by Mysid. Electromagnetic transmittance, or opacity, of the Earth's atmosphere., 2008. [Online; accessed Jan 27, 2016].

[7] Eugene Hechet, editor. *Optics Fourth Edition.* Addison-Wesley Publishing Company, Massachusetts, 2002.

[8] Cerro-Tololo Inter American Observatory. Imaging through the turbulence, 2012. [Online; accessed June 24, 2016].

[9] Rafael C. Gonzalez and Richard E Woods, editors. *Digital Image Processing*. Addison-Wesley Publishing Company, Massachusetts, 1992.

[10] CN Guiar, FL Lansing, and R Riggs. Antenna pointing systematic error model derivations. 1986.

[11] Lewis Woodburn, Tim Natusch, Stuart Weston, Peter Thomasson, Mark Godwin, Christophe Granet, and Sergei Gulyaev. Conversion of a New Zealand 30-metre telecommunications antenna into a Radio Telescope. *Publications of the Astronomical Society of Australia*, 32:e017, 2015.

[12] E Himwich, N Vandenberg, R Gonzalez, and C Holmström. New developments in the NASA Field System. In *New technologies in VLBI*, volume 306, page 193, 2003.

[13] Ed Himwich. Automated Pointing Models Using the FS. Technical report, NASA Goddard Space Flight Center, May 2011.

[14] Richard Blum. *Linux command line and shell scripting bible*, volume 481. John Wiley & Sons, 2008.

[15] L Richard Jr et al. *Scientific data analysis: An introduction to overdetermined systems*. Springer Science & Business Media, 2012.

[16] B.P. Macfie and P.M. Nufrio. *Applied Statistics for Public Policy*. M.E. Sharpe, 2006.

[17] Sergei Gulyaev, Tim Natusch, and David Wilson. Characterisation and calibration of the 12-m antenna in Warkworth, New Zealand. In *The 5th IVS General Meeting Proc*, 2010.

[18] Bach Uwe. Effelsberg wiki: A new term for the Effelsberg pointing model. https://eff100mwiki.mpifr-bonn.mpg.de/lib/exe/fetch.php?media=information_for_astronomers:20090522_poi.pdf, 2009.

[19] Douglas M Hawkins. The problem of overfitting. *Journal of chemical information and computer sciences*, 44(1):1–12, 2004.

[20] BH Grahl, MP Godwin, and EP Schoessow. Improvement of the Effelsberg 100 meter Telescope based on holographic reflector surface measurement. *Astronomy and Astrophysics*, 167:390–394, 1986.

[21] Kenneth Edmundson and Lynn Baker. Photogrammetric Measurement Of The Arecibo Primary Reflector Surface. 2001.

[22] J Ruze. Antenna Cost, Efficiency, and System Noise. *IEEE Transactions on Antennas and Propagation*, 14(2):249–250, 1966.

[23] Stephen Padin Sidhi Assawaworrarit. An optical pointing Telescope for Radio Astronomy. *Publications of the Astronomical Society of the Pacific*, 124(913):242–246, 2012.

[24] Sergei Gulyaev, Tim Natusch, Stuart Weston, Neville Palmer, and David Collett. Warkworth 12 m VLBI station: Wark12m. *arXiv preprint arXiv:1103.2830*, 2011.

[25] Jim Lovell. Antenna pointing solutions :reduction of observation and producing a model. http://auscope.phys.utas.edu.au/opswiki/doku.php?id=operations:pointing, 2014.

[26] Leonid Petrov, Tim Natusch, Stuart Weston, Jamie McCallum, Simon Ellingsen, and Sergei Gulyaev. First scientific vlbi observations using New Zealand 30 metre Radio Telescope wark30m. *arXiv preprint arXiv:1502.06802*, 2015.

[27] Antenna Measurement and Consultant Services. Integrated Antenna Controller for the Cornell University 12 m Antenna at the Arecibo Observatory. Technical report, MP Godwin Limited, May 2010.

[28] Christoph Holst and Heiner Kuhlmann. Challenges and present fields of action at laser scanner based deformation analyses. *Journal of Applied Geodesy*, 10(1):17–25, 2016.

[29] Arthur Berry. *A Short History of Astronomy: From Earliest Times Through the Nineteenth Ventury*. Dover, 1961.

[30] Pierguido Sarti, Luca Vittuari, and Claudio Abbondanza. Laser scanner and terrestrial surveying applied to gravitational deformation monitoring of large VLBI Telescopes' primary reflector. *Journal of Surveying Engineering*, 135(4):136–148, 2009.

[31] Christoph Holst, Philipp Zeimetz, Axel Nothnagel, Wolfgang Schauerte, and Heiner Kuhlmann. Estimation of focal length variations of a 100-m radio telescope's main reflector by laser scanner measurements. *Journal of Surveying Engineering*, 138(3):126–135, 2012.

[32] AL Berman and ST Rockwell. New Optical And Radio Frequency Angular Tropospheric Refraction Models For Deep Space Applications. 1976.

Appendix A

Field System Commands

To log into field system using command line:

ssh oper@152.62.231.136

password: *******

Then type the command *fs* in the field system terminal

Some useful field system commands:

Operator Input:

> kill (stops all current process)

> source= stow

> proc = sscpoint

> initp (to initialise the current FS setup)

> ifa

> acquire

* proc=sscpoint initiates the pointing file. * acquire save the updated log file after the observation is completed

A.1 Screenshot of a part of the log file

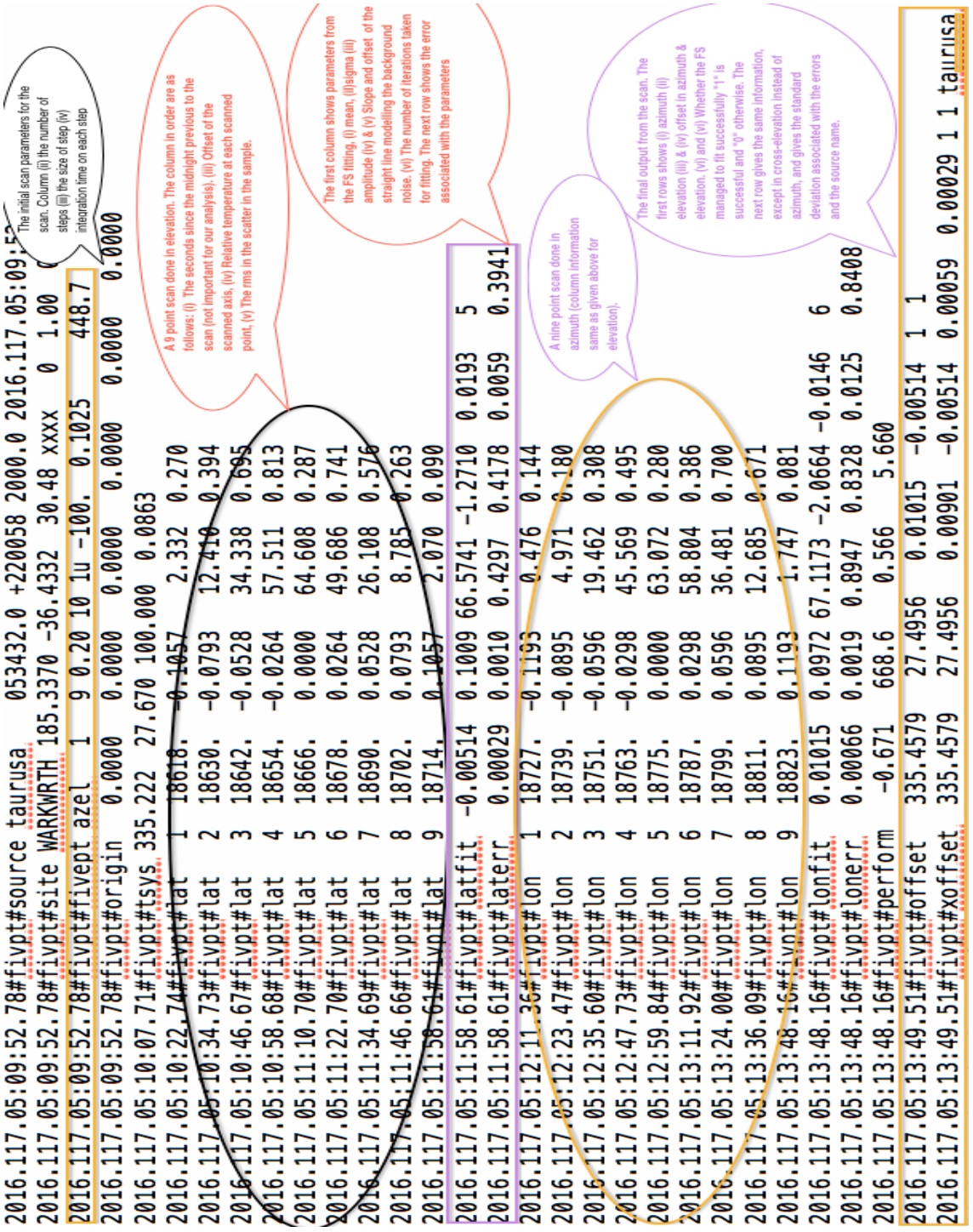

Figure A.1: A screenshot of part of the logfile, with explanation.

A.2 Terms in the Field System Pointing Model

P1 = X-angle Encoder Offset

P2 = X-angle Sag

P3 = Axis SKew

P4 = Box Offset

P5 = Tilt Out (tilt of Y=+90 toward X,Y=0,0)

P6 = Tilt Over (tilt of Y=+90 toward X,Y=90,0)

P7 = Y-Angle Encoder Offset

P8 = Y-Angle Sag

P9 = ad hoc Y-angle slope (degrees/radian)

P10 = ad hoc Y-angle cos(Y) term

P11 = ad hoc Y-angle sin(Y) term

P12 = ad hoc X-angle slope (degrees/radian)

P13 = ad hoc X-angle cos(X) term

P14 = ad hoc X-angle sin(X) term

P15 = ad hoc Y-angle cos(2*X) term

P16 = ad hoc Y-angle sin(2*X) term

P17 = ad hoc X-angle cos(2*X) term

P18 = ad hoc X-angle sin(2*X) term

P19 = ad hoc Y-angle cos(8*Y) term

P20 = ad hoc Y-angle sin(8*Y) term

P21 = ad hoc Y-angle cos(X) term

P22 = ad hoc Y-angle sin(X) term

*collected from the FS manual

Appendix B

Additional Plots

Azimuth plot after adding P19 and P20 to the model

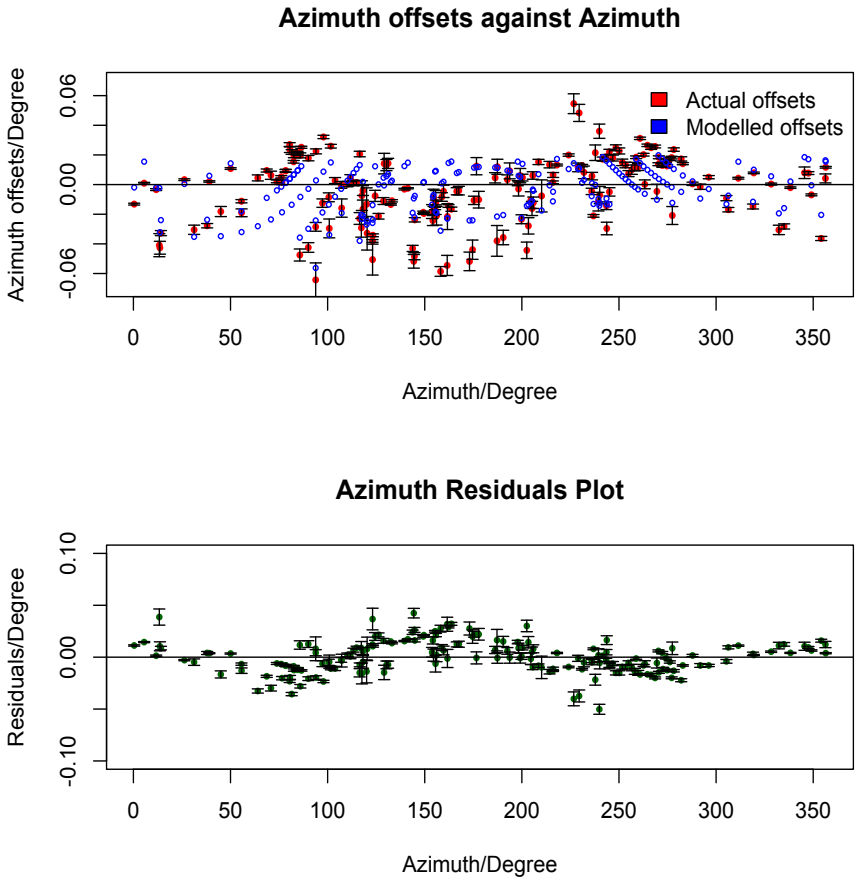

Figure B.1: The azimuth offset plot after adding P19 and P20 to the model. The sinusoidal pattern is still observed in azimuth, and the rms of the residual is still quiet high (0.0153°).

Elevation plot after adding P19 and P20 to the model

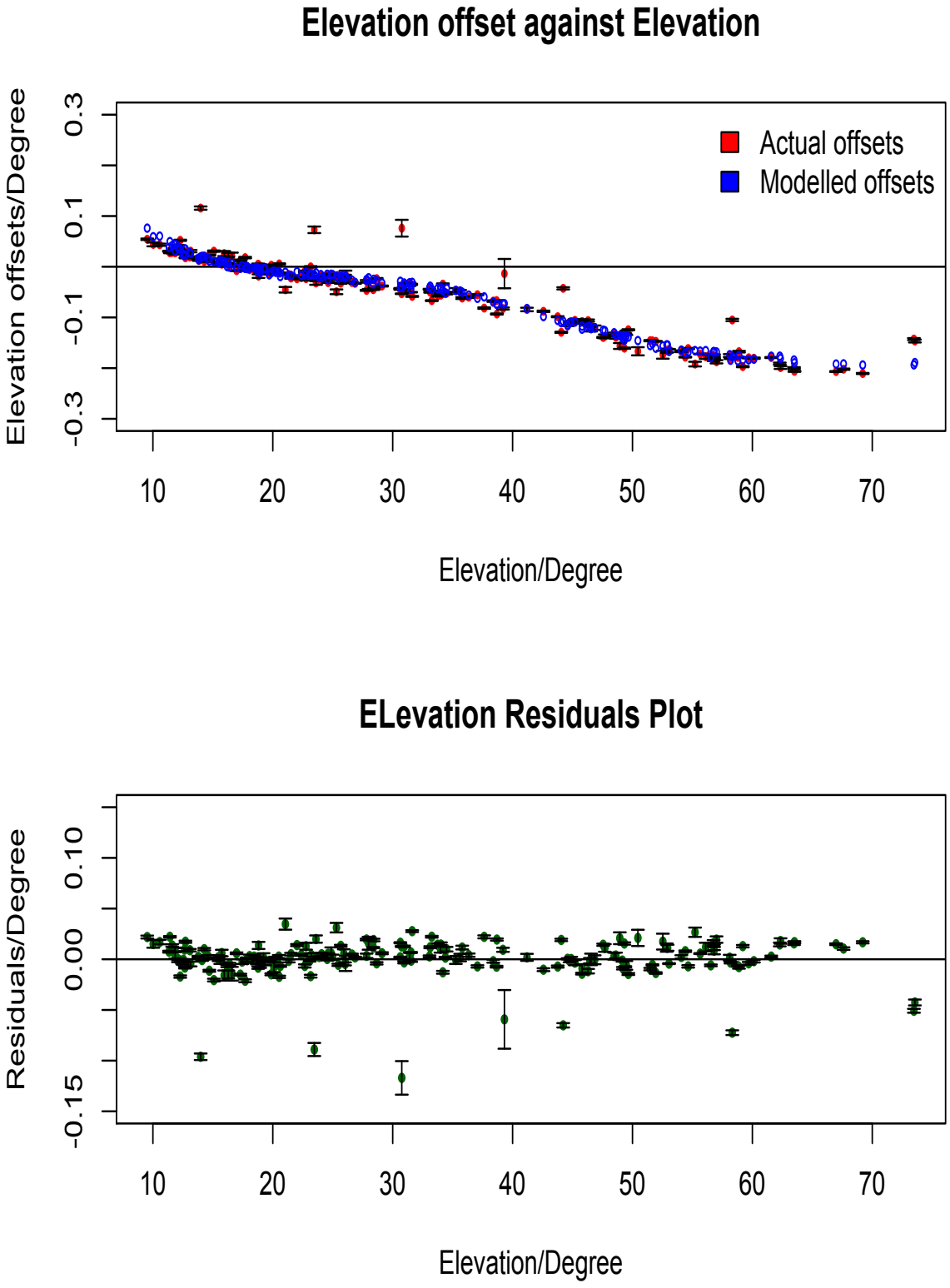

Figure B.2: The elevation offset plot after adding P19 and P20 to the elevation model. The model effectively eliminates the sinusoidal pattern in the elevation offsets, and the rms improved to 0.01949° (from 0.0229°). The scatter in the residual is still quiet high due to the strength of the sources used.

Azimuth plot using updated sources and P20

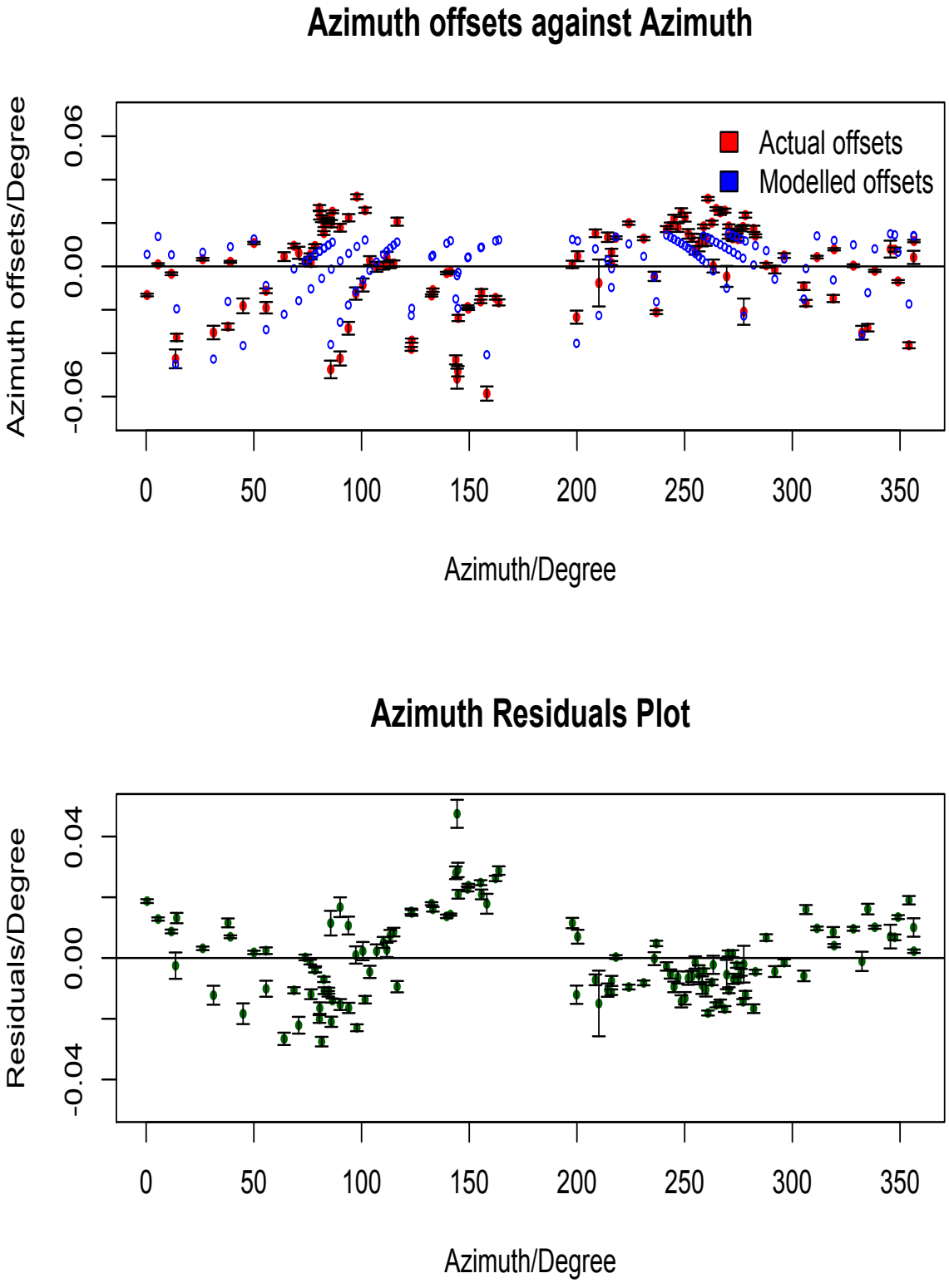

Figure B.3: The azimuth offset plot with only strong and moderate strength sources (used for analysis). The rms of the residual decreases to 0.0135° (from 0.0153°). A sinusoidal pattern still exists in the residuals of the azimuth offsets.

Elevation plot using updated sources and P20

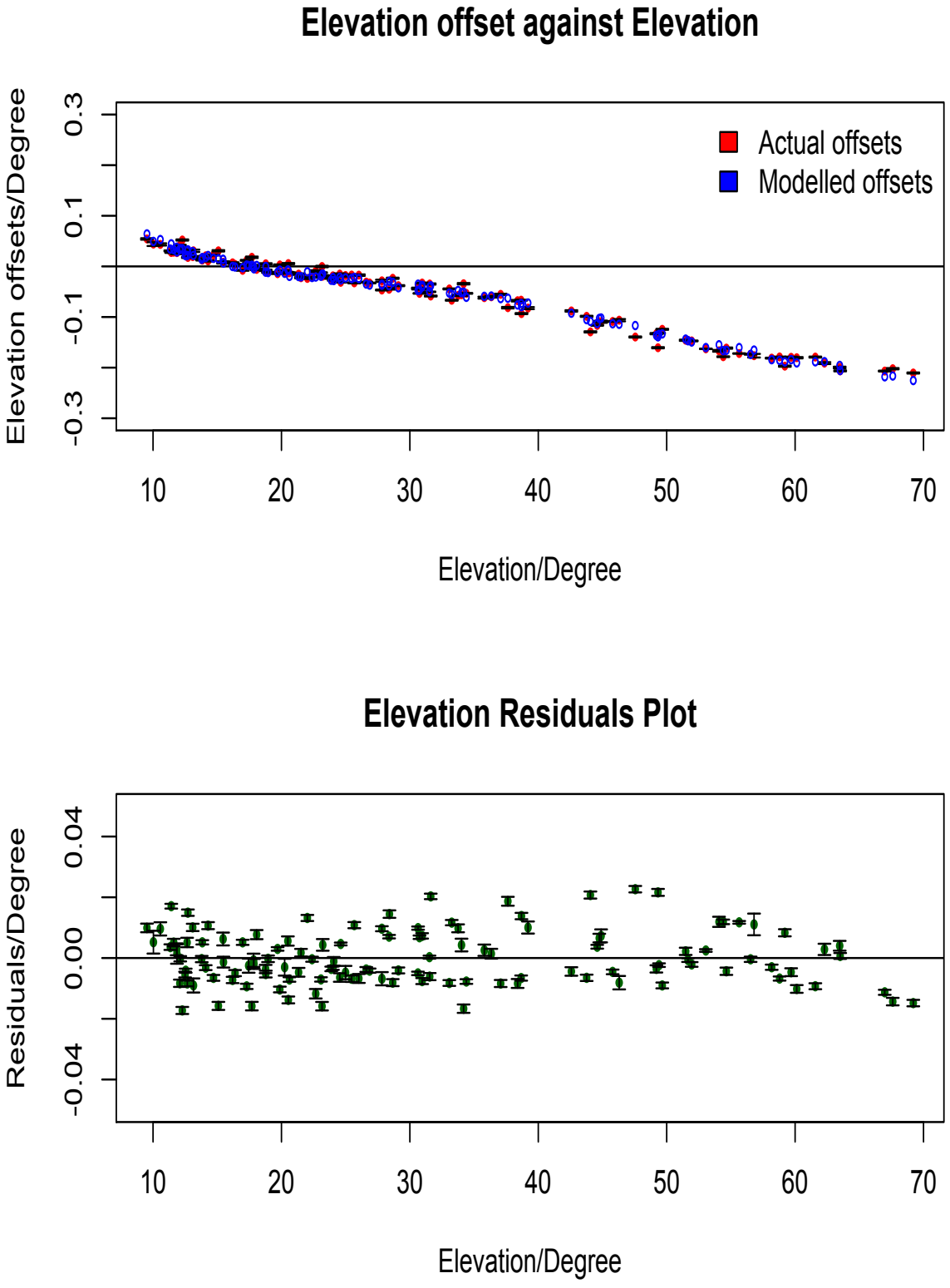

Figure B.4: The elevation offset plot with only strong and moderate strength sources (used for analysis). The rms of the residuals decreases significantly to 0.0085°, which is just within 10% of the beam.

Azimuth plot using updated sources and P17

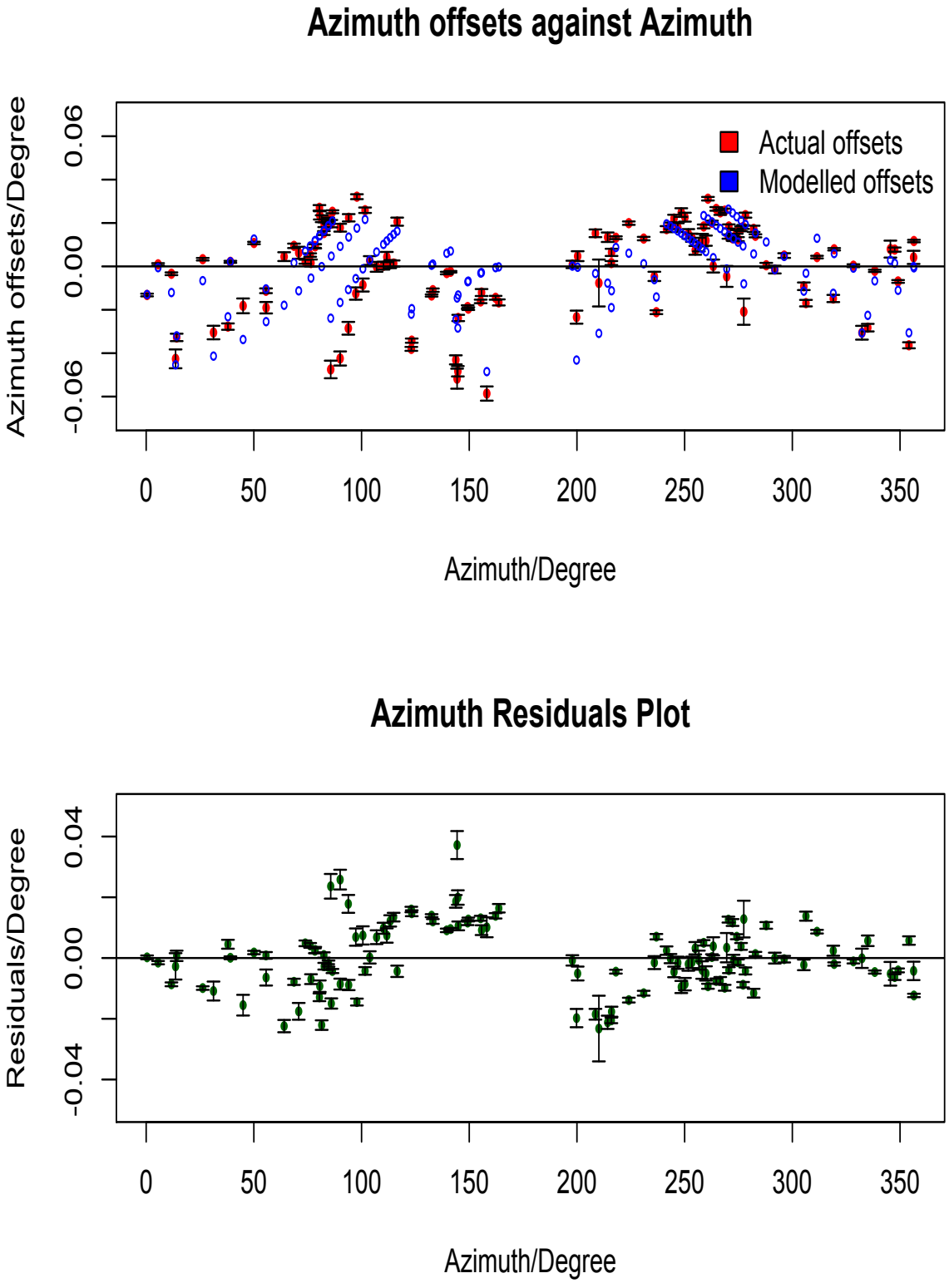

Figure B.5: The azimuth offset plot after adding P17 to the azimuth equation in the model. The sinusoidal pattern is somewhat suppressed. The dispersion is relatively high between 100 and 150 degree, possibly due to some phase offset in the sinusoidal which can't be modelled by only P17. The rms of the offset residuals was 0.0107°.

Azimuth plot using updated sources and P18

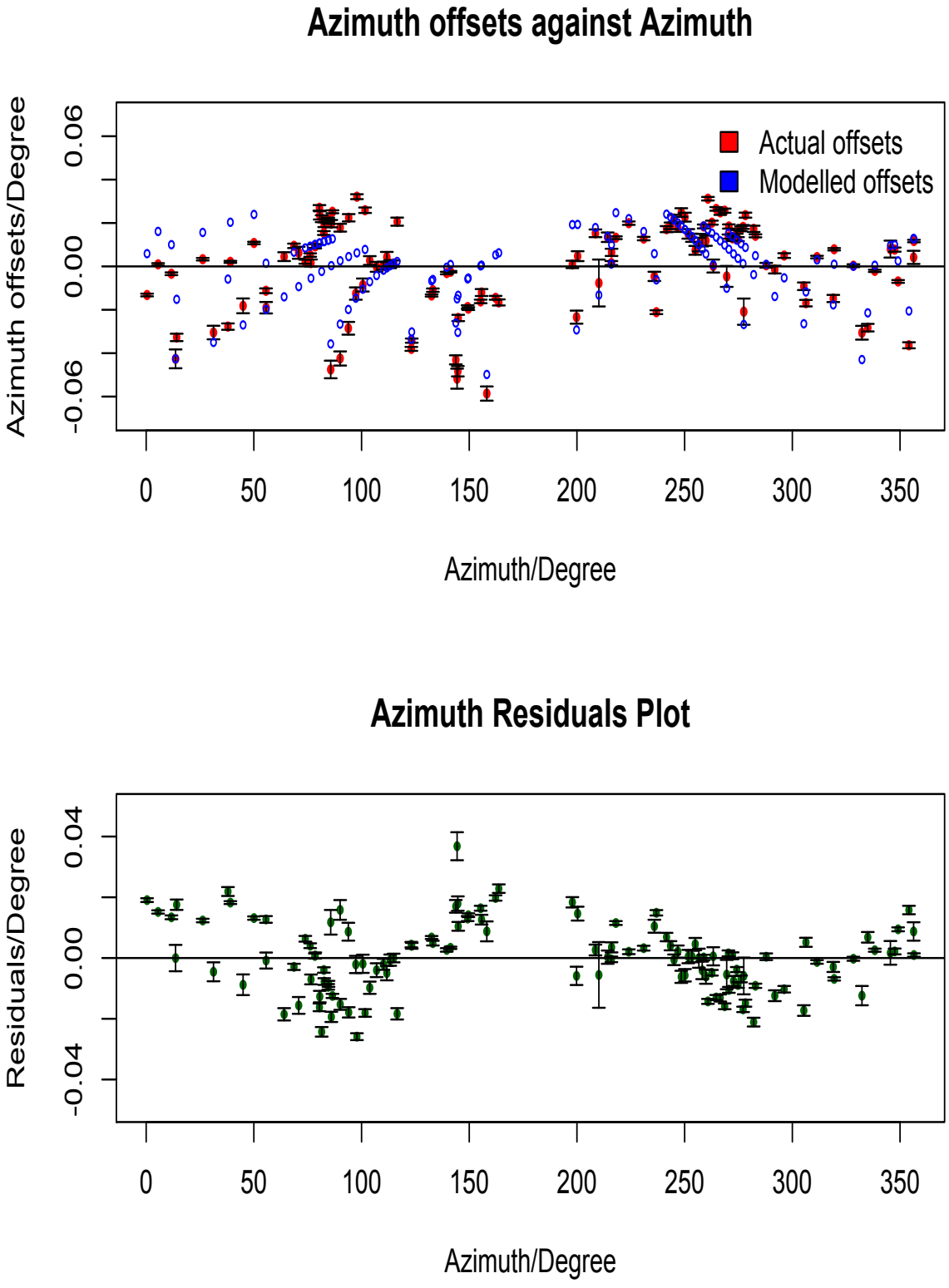

Figure B.6: The azimuth offset plot after adding P18 to the model. The sinusoidal pattern is still observed. The rms of the azimuth offset residuals was 0.0113°.

B.0.1 Analysis plots of pointing database: Collected with an existing model at 6.7 GHz

Azimuth plot for a pointing dataset with new model applied

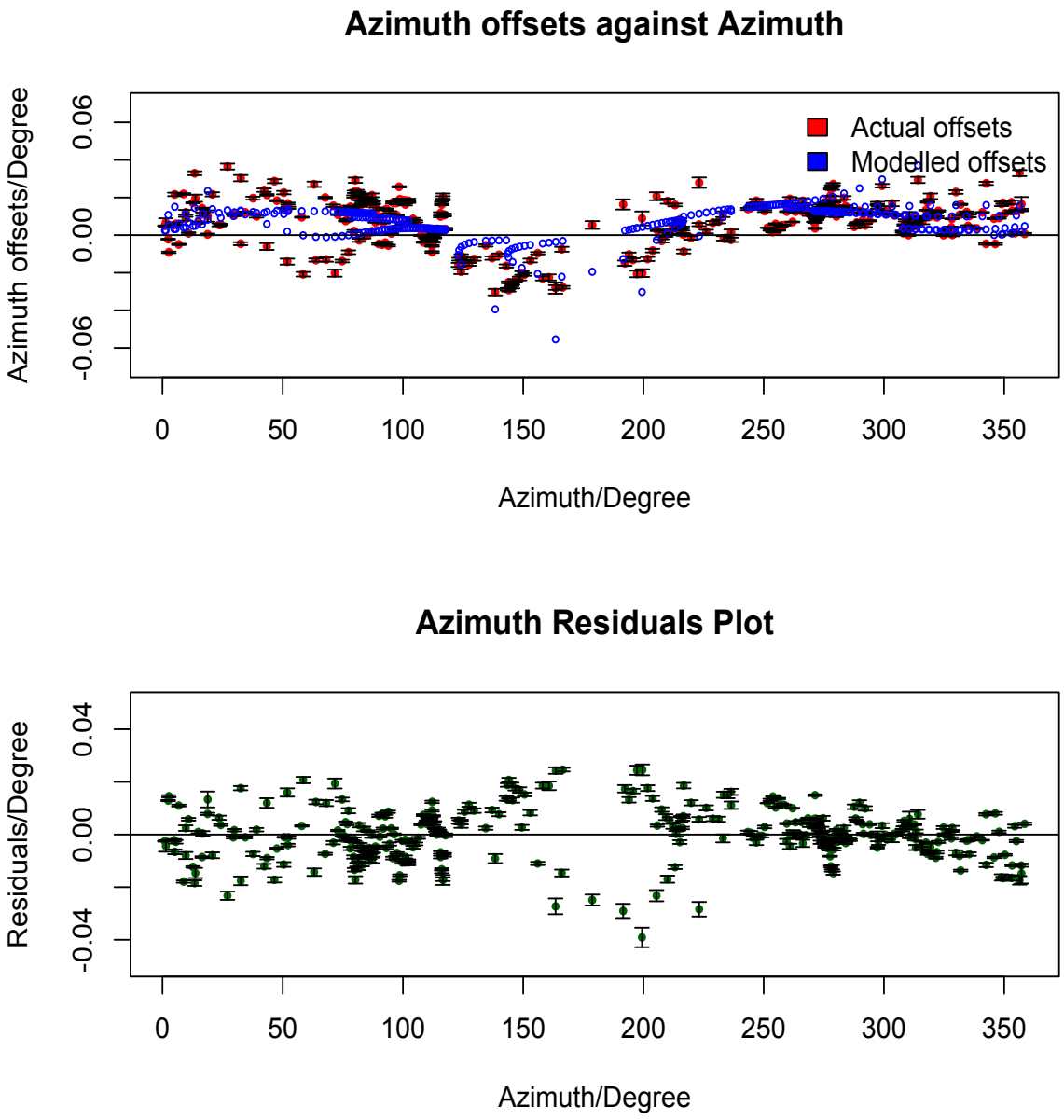

Figure B.7: Azimuth plot of pointing offsets that was collected with an existing model running in background. The rms of the offsets in both azimuth was ∼0.0143°. The rms after applying the new model in both azimuth was ∼0.009°.

Elevation plot for a pointing dataset collected using new model applied

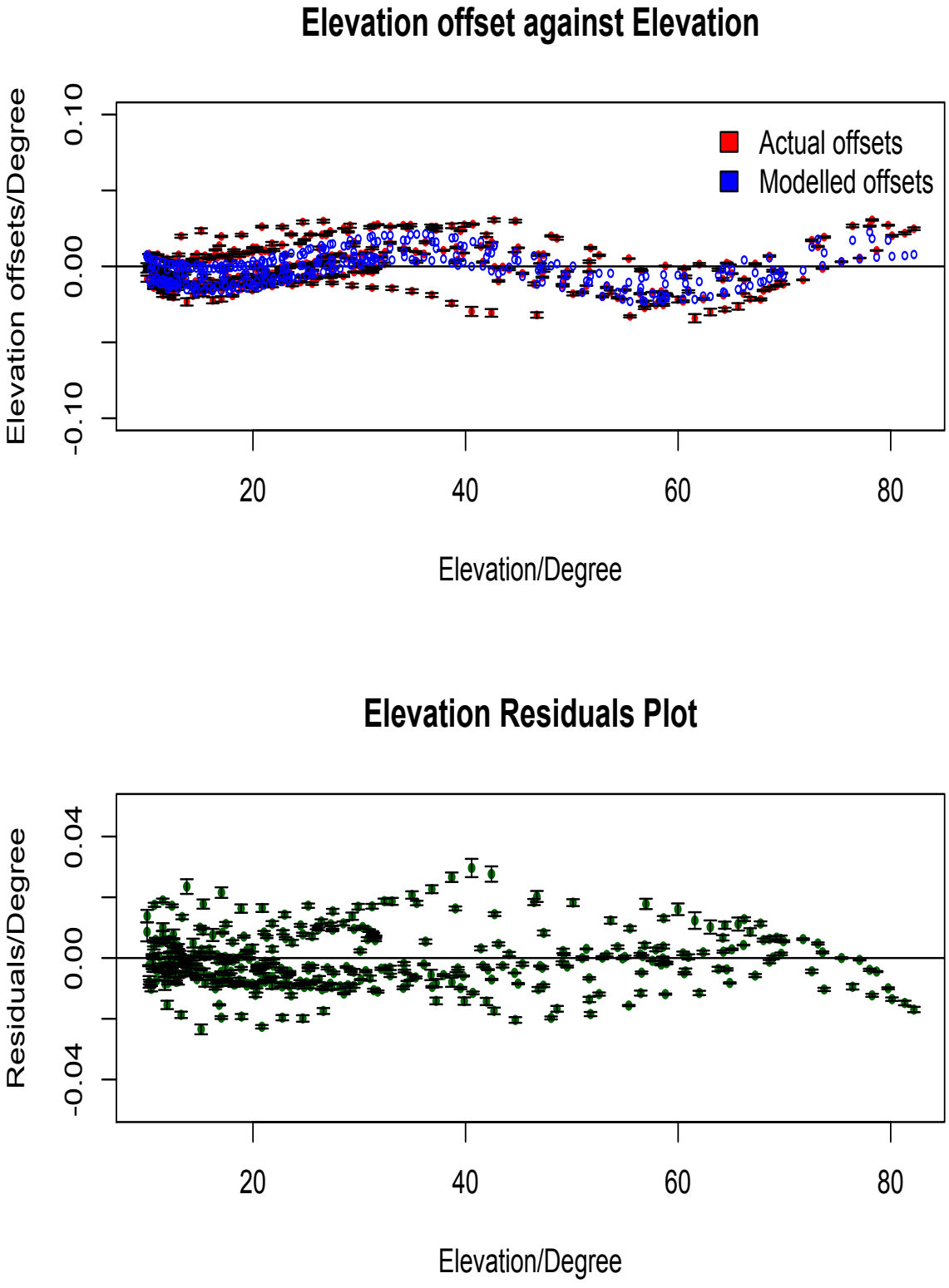

Figure B.8: Elevation plot of pointing offsets that was collected with an existing model running in background. The rms of the offsets in both elevation was ∼0.0143°. The rms after applying the new model in both elevation was ∼0.009°.

B.0.2 Analysis plots of pointing database: Collected with an existing model at 8.2 GHz

Azimuth plot for a pointing dataset collected using existing model at 8.2 GHz

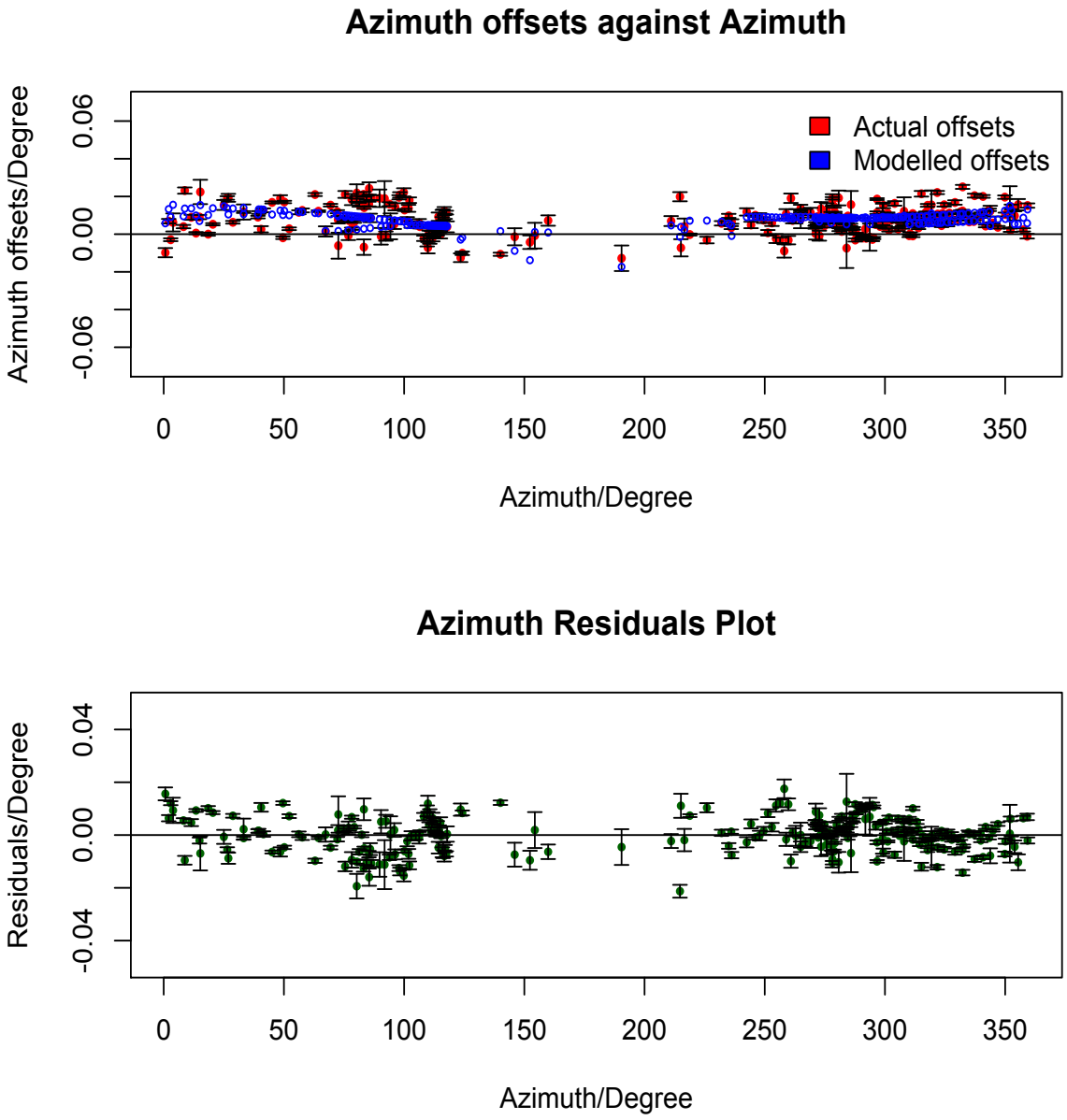

Figure B.9: Azimuth plot of pointing offsets at 8.2 GHz that was collected with an existing model running in background. The rms of the collected offsets in azimuth was ∼0.025°. After applying source selection and outlier removal process, the rms of the residuals went down to ∼0.0089°. After applying the new model, the rms of the elevation residual further went down to ∼0.0062°.

Elevation plot for a pointing dataset collected using existing model at 8.2 GHz

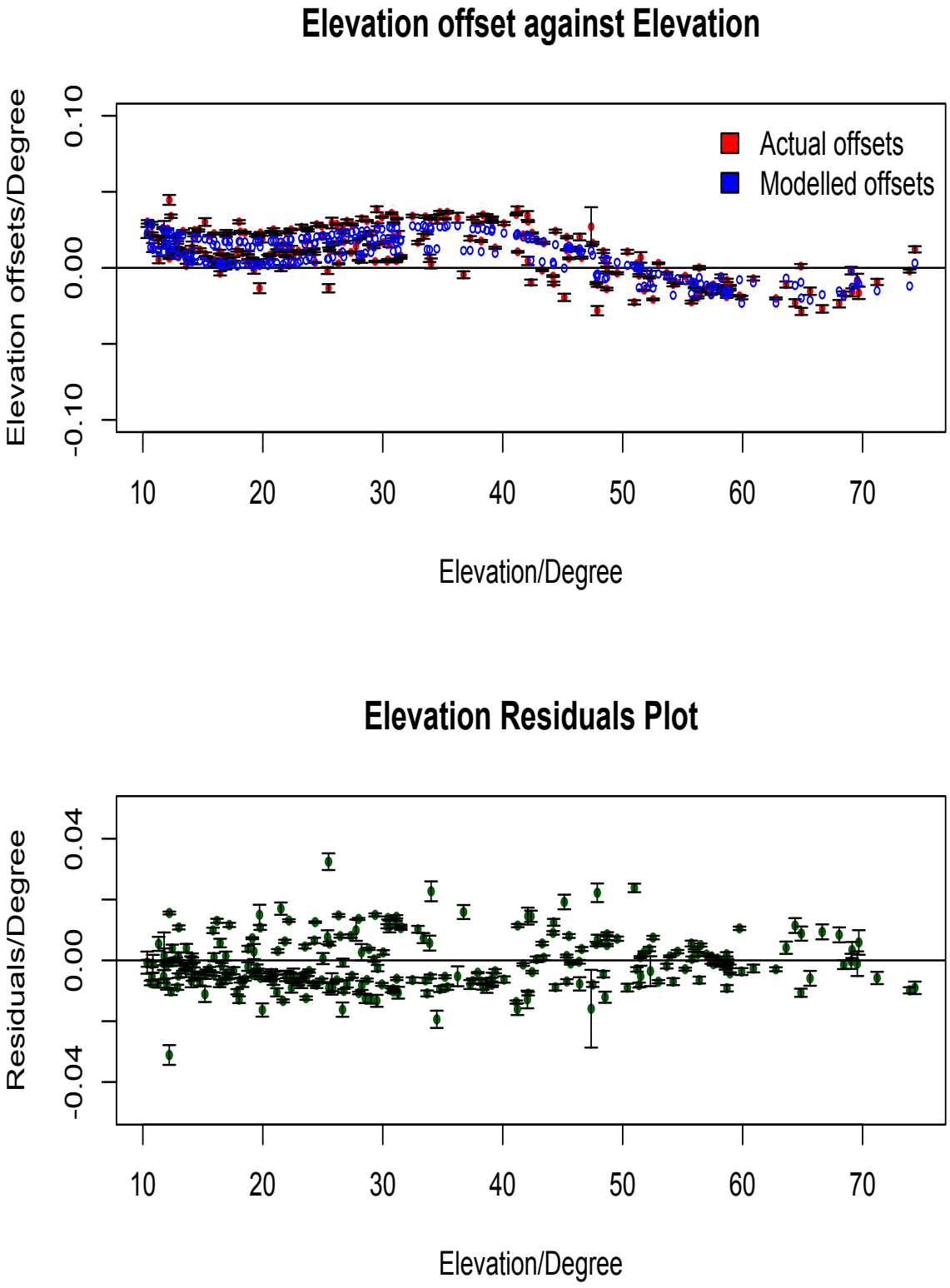

Figure B.10: Elevation plot of pointing offsets at 8.2 GHz that was collected with an existing model running in background. The rms of the offsets in elevation was ∼0.022°. After applying source selection and outlier removal process, the rms of the residuals went down to ∼0.0167°. After applying the new model, the rms of the elevation residual further went down to ∼0.009°.

B.1 31-step scan of sources used for pointing

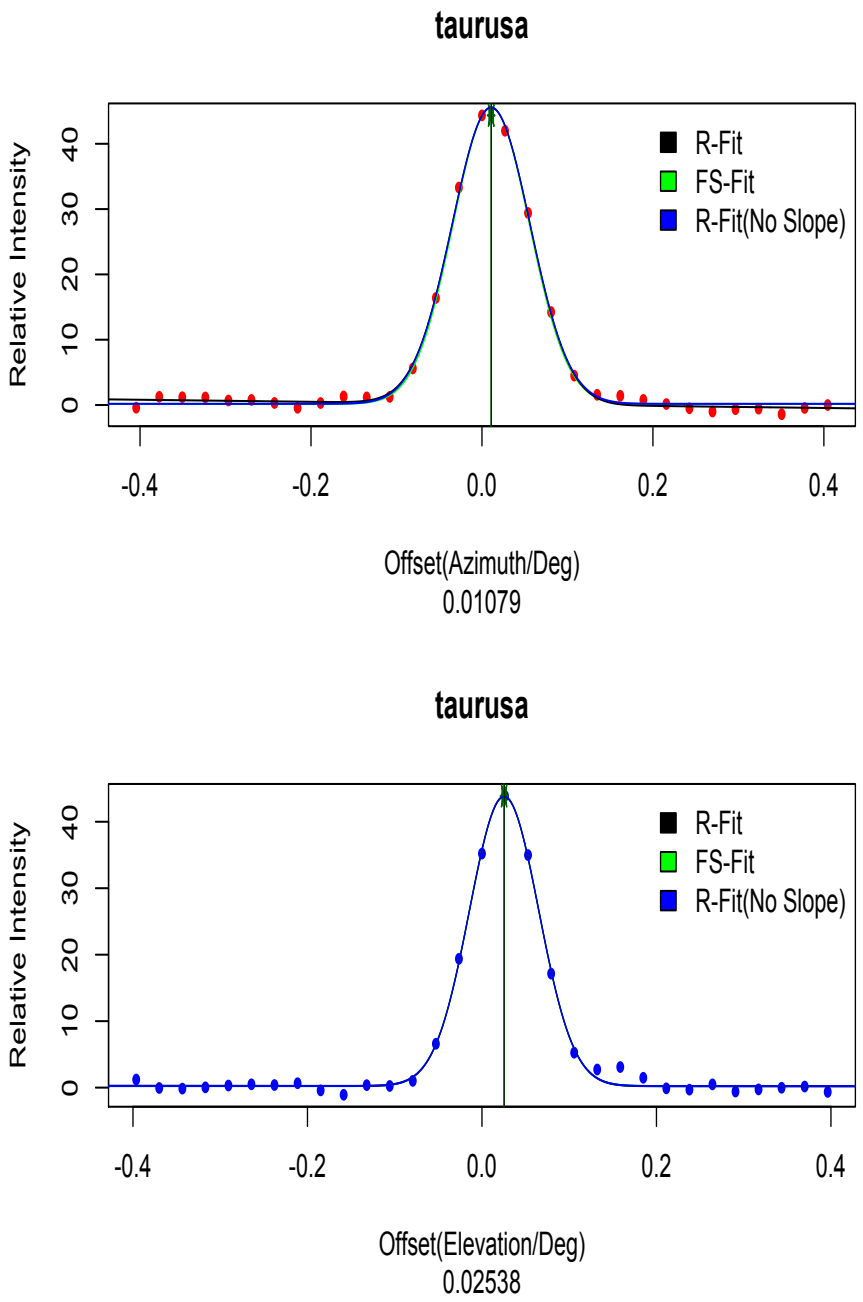

Figure B.11: 31-Step Scan plot of Taurus A

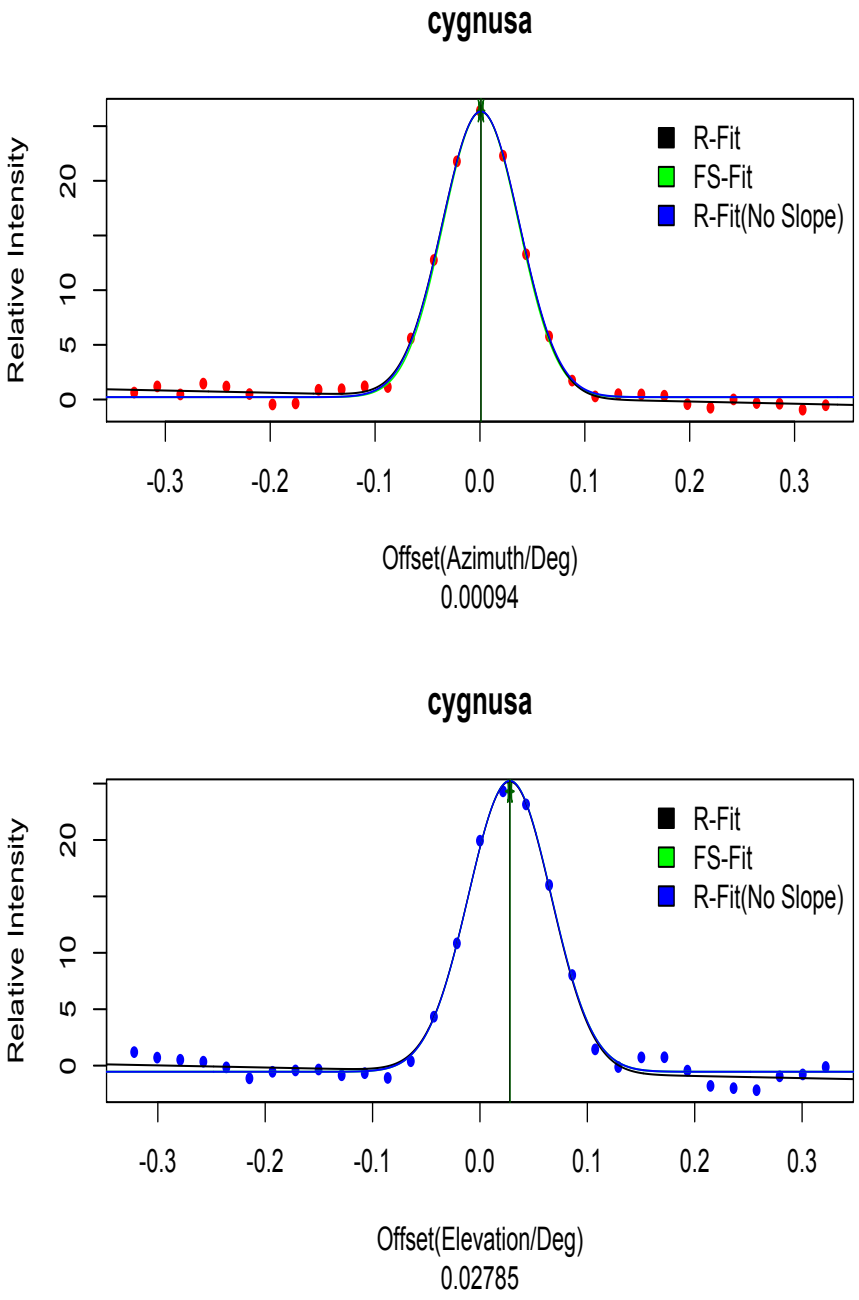

Figure B.12: 31-Step Scan plot of Cygnus A

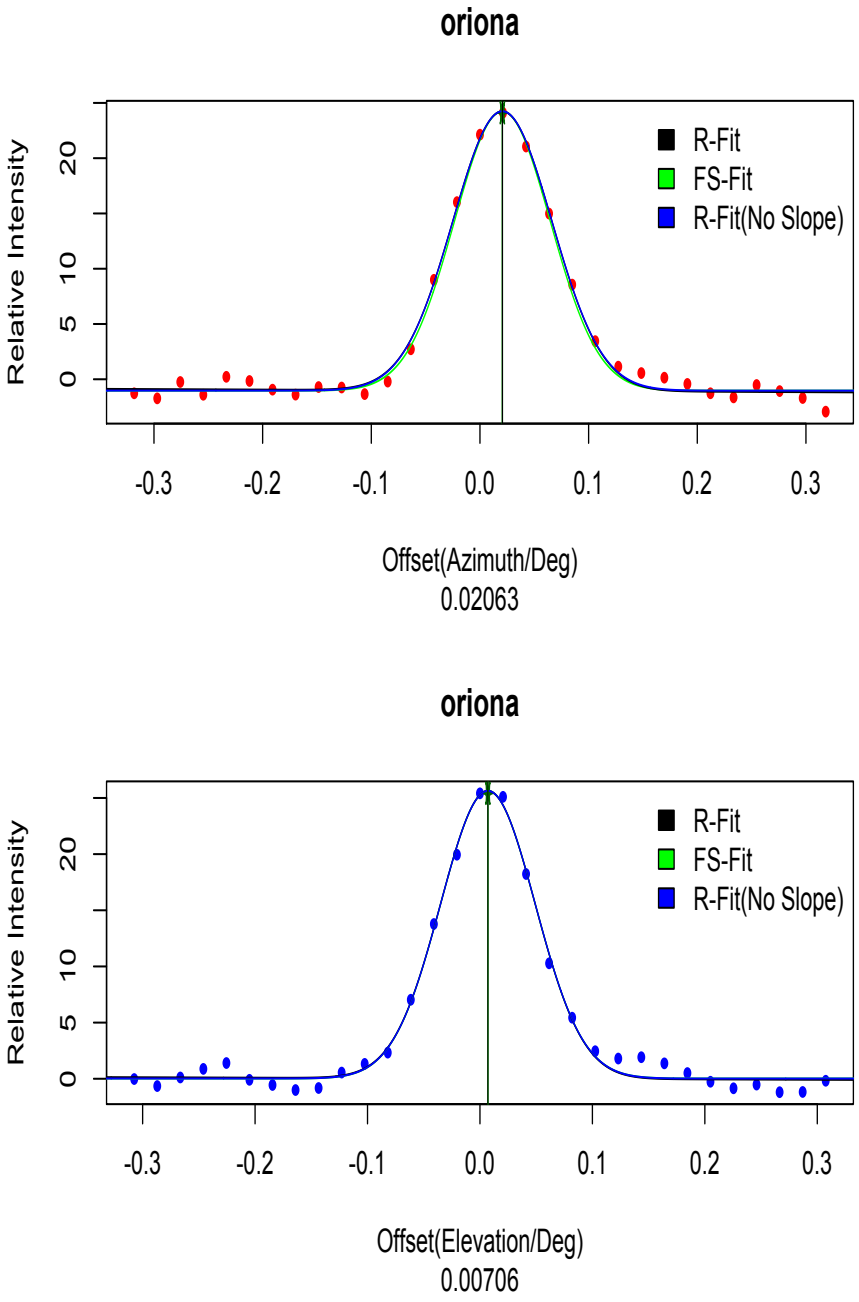

Figure B.13: 31-Step Scan plot of Orion A

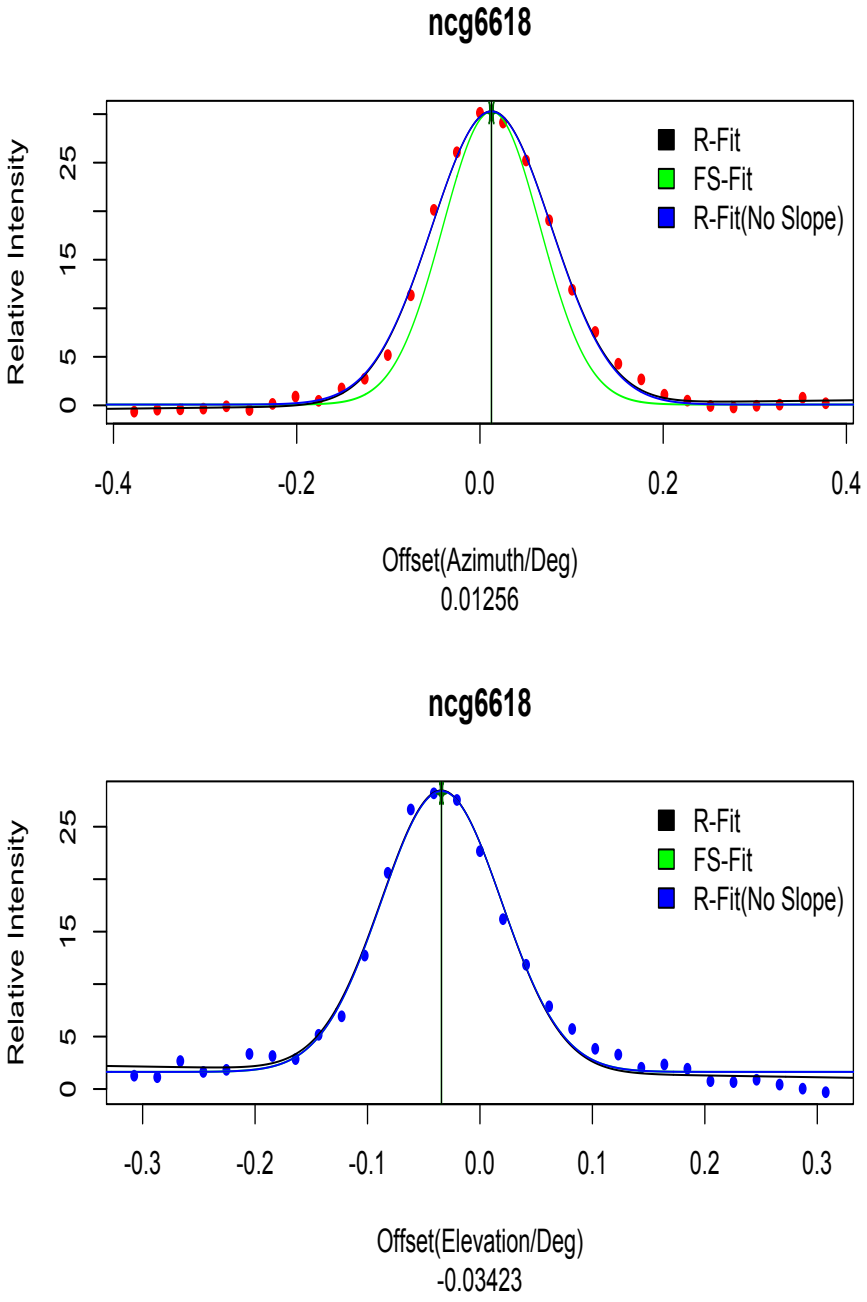

Figure B.14: 31-Step Scan plot of NGC 6618

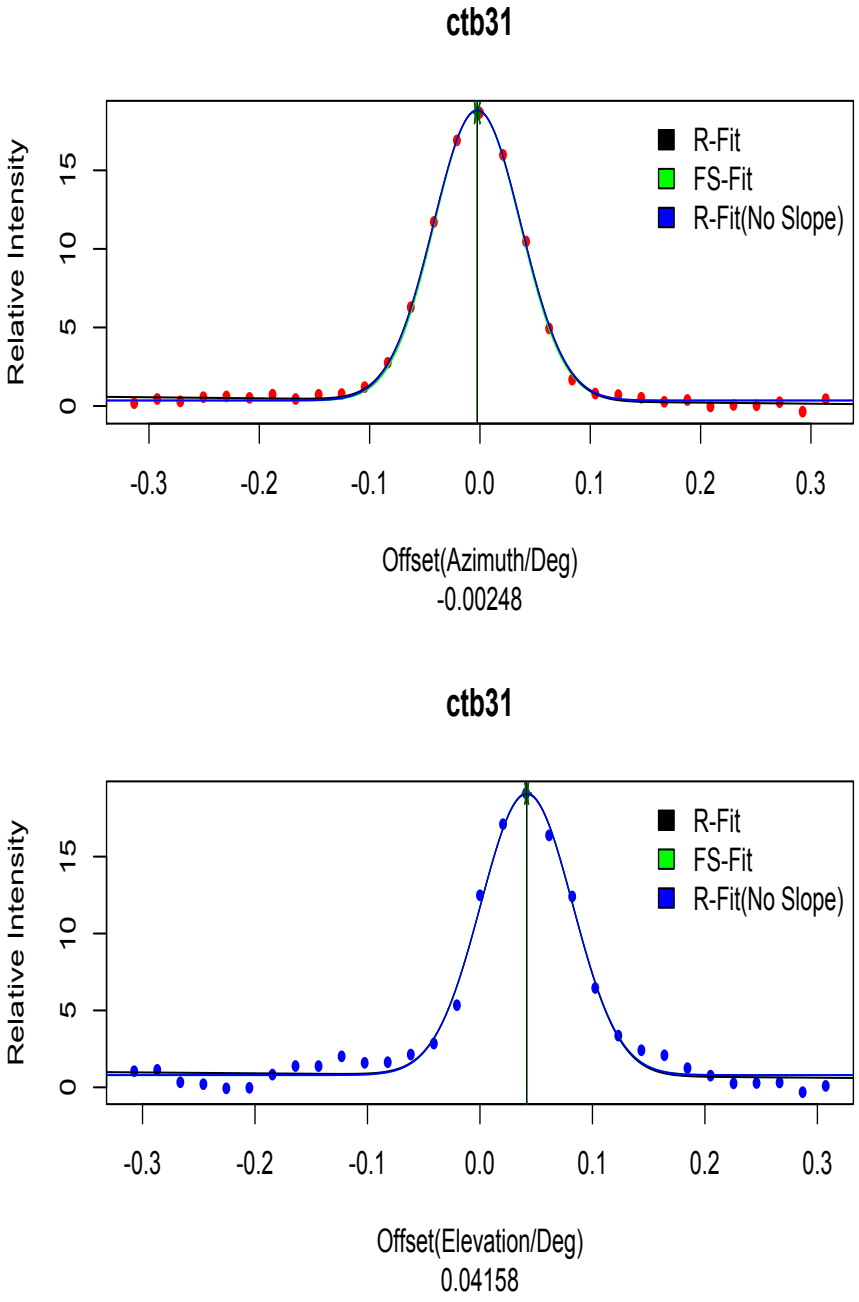

Figure B.15: 31-Step Scan plot of CTB 031

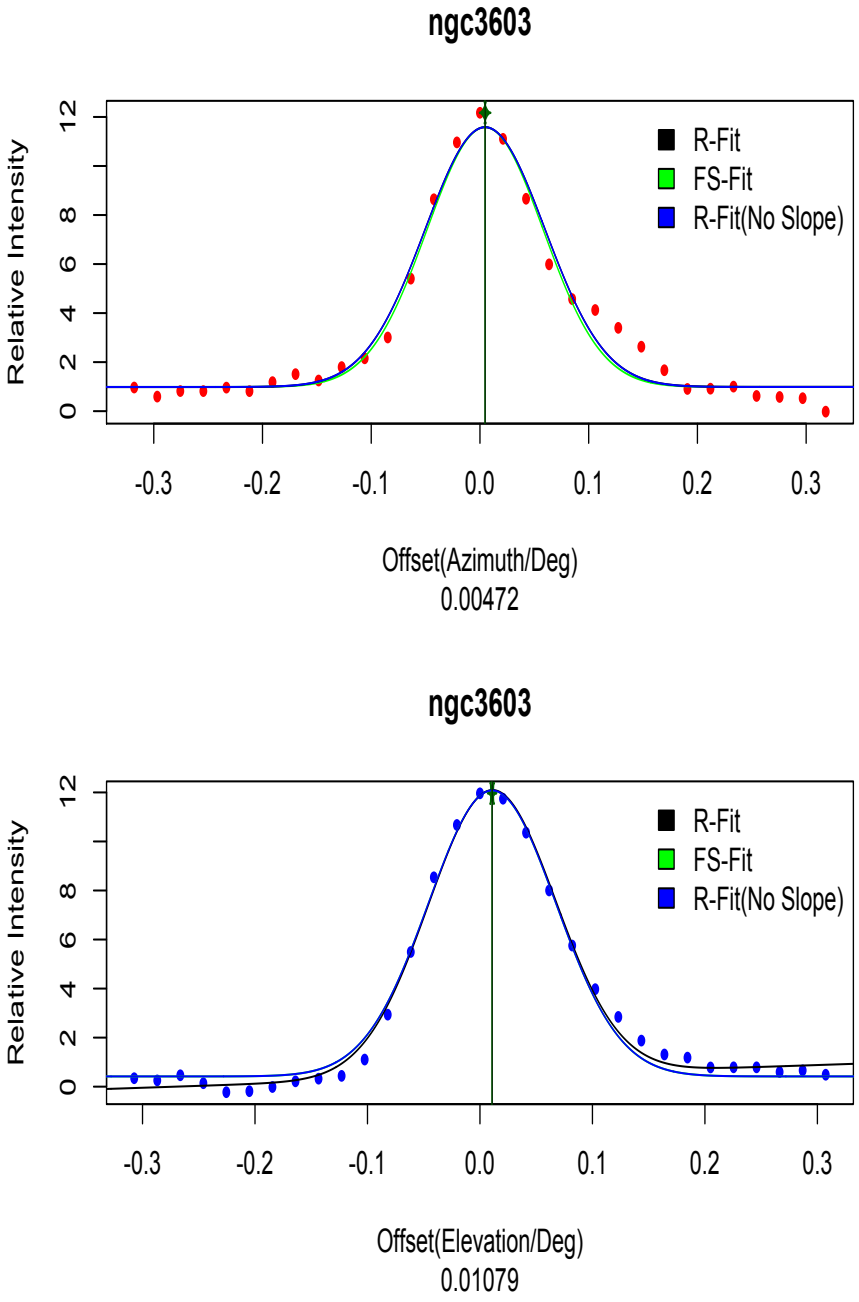

Figure B.16: 31-Step Scan plot of NGC 3603

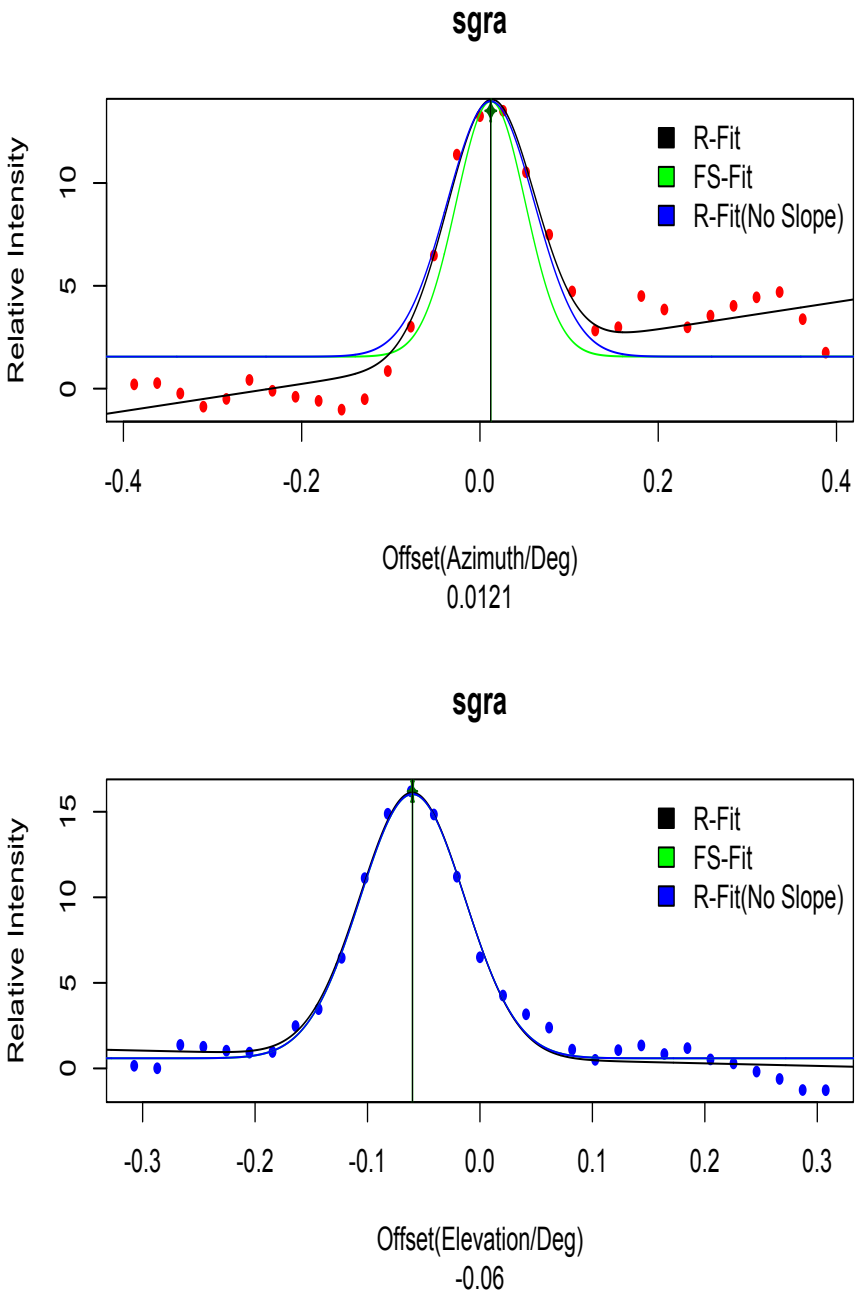

Figure B.17: 31-Step Scan plot of Sagittarius A

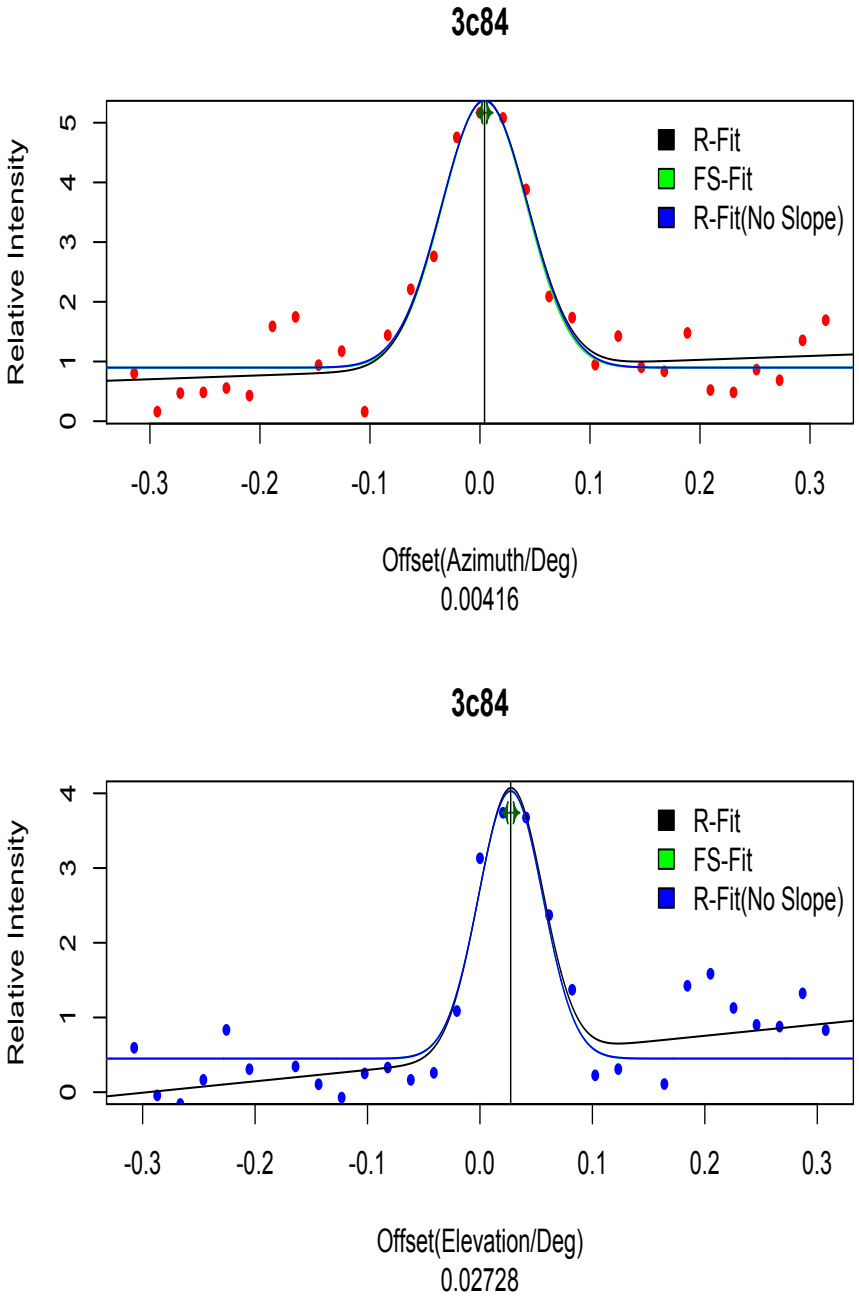

Figure B.18: 31-Step Scan plot of NGC 1275

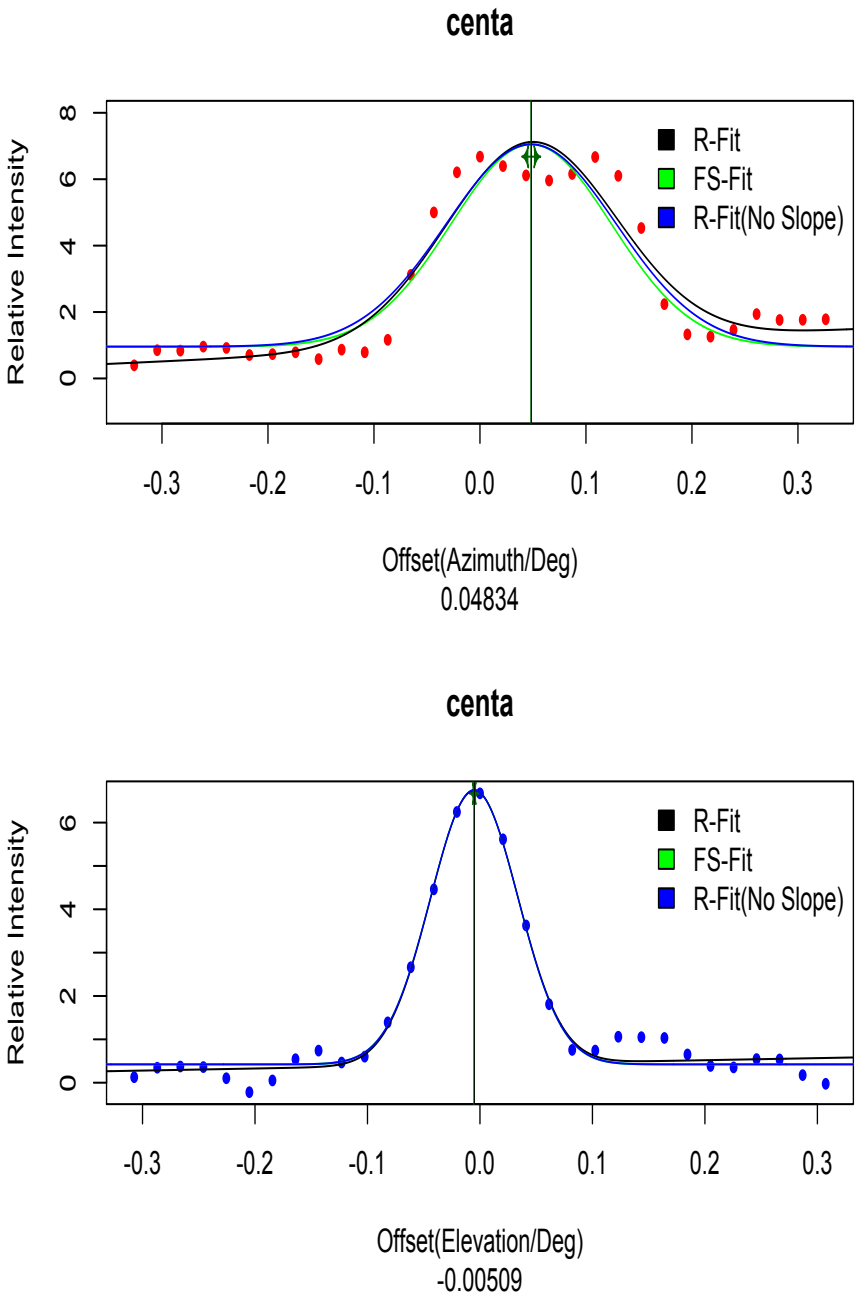

Figure B.19: 31-Step Scan plot of Centaurus A

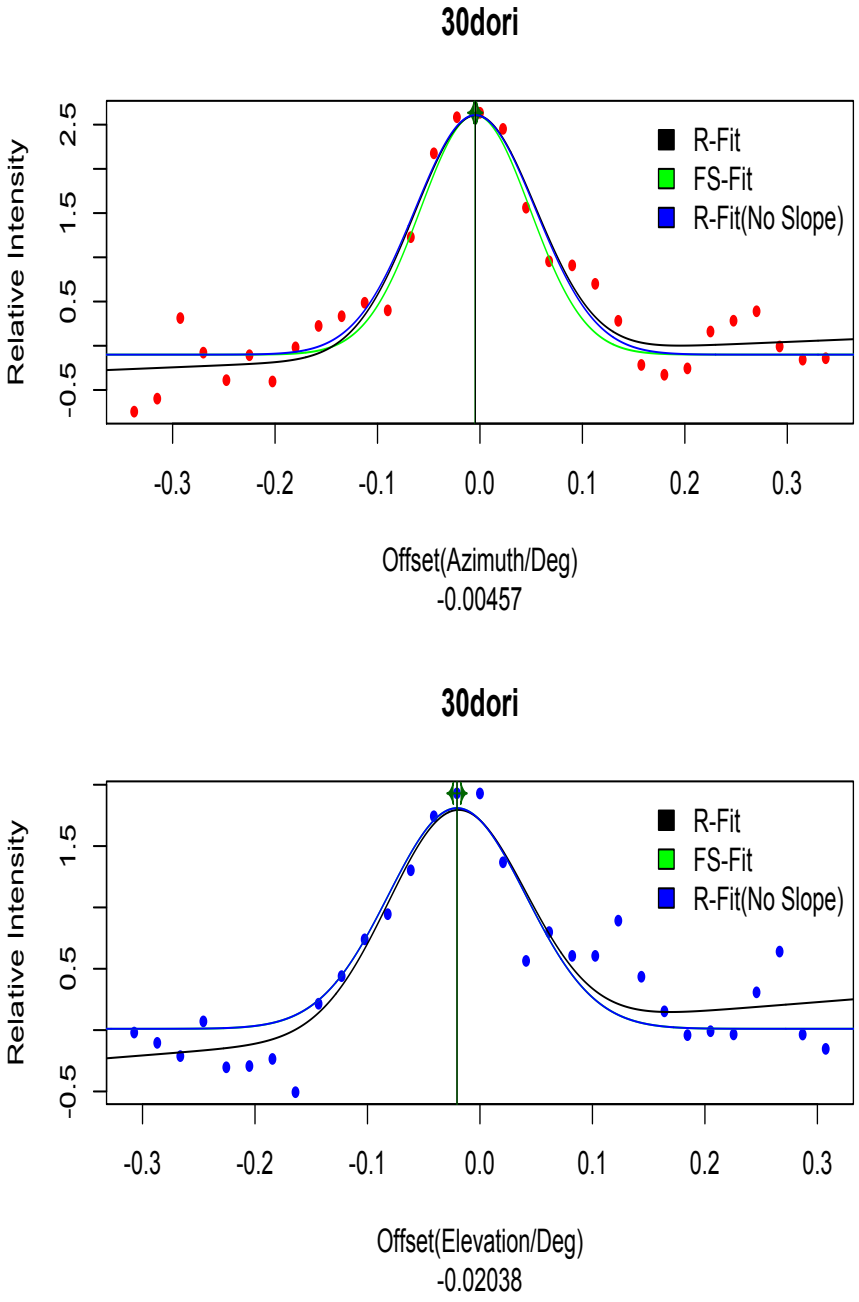

Figure B.20: 31-Step Scan plot of 30 Doradus

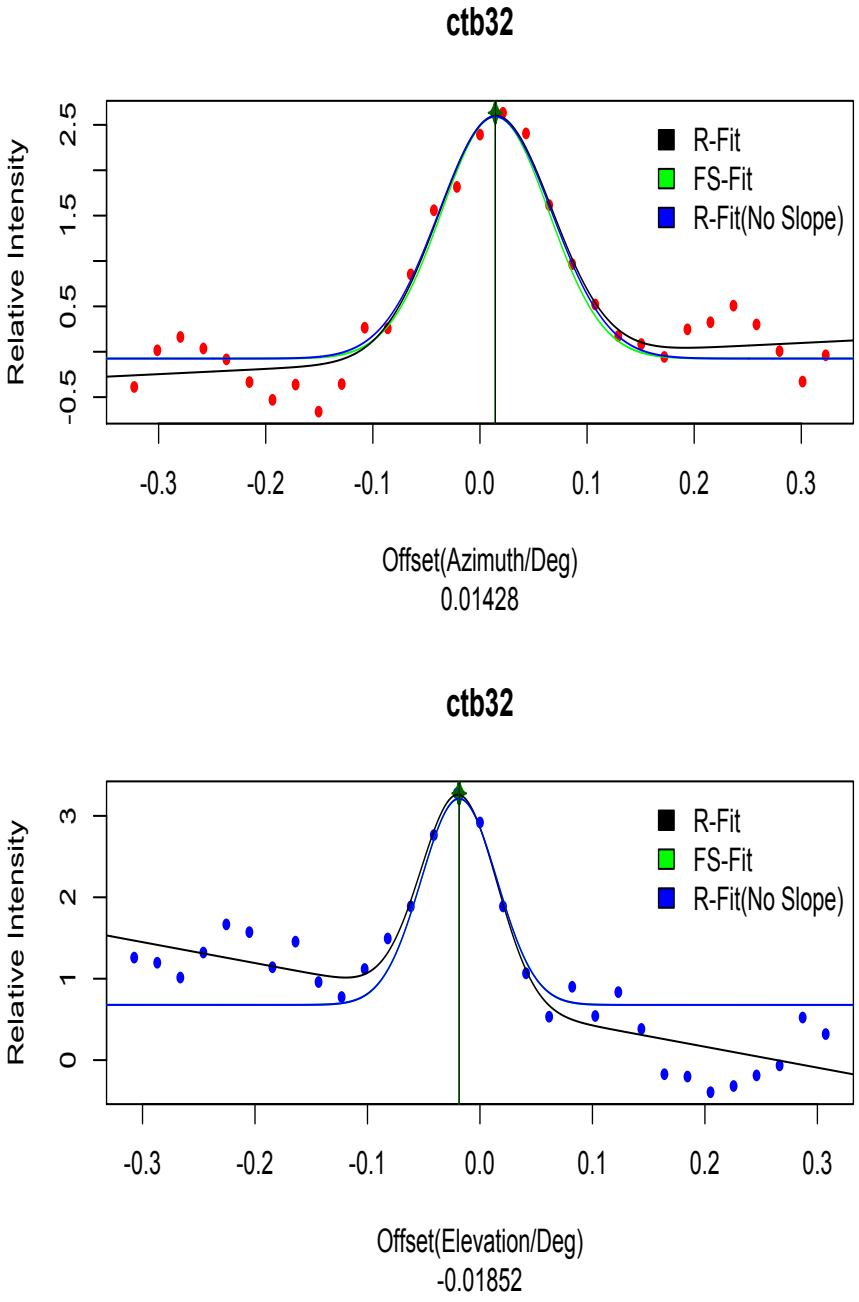

Figure B.21: 31-Step Scan plot of CTB 32

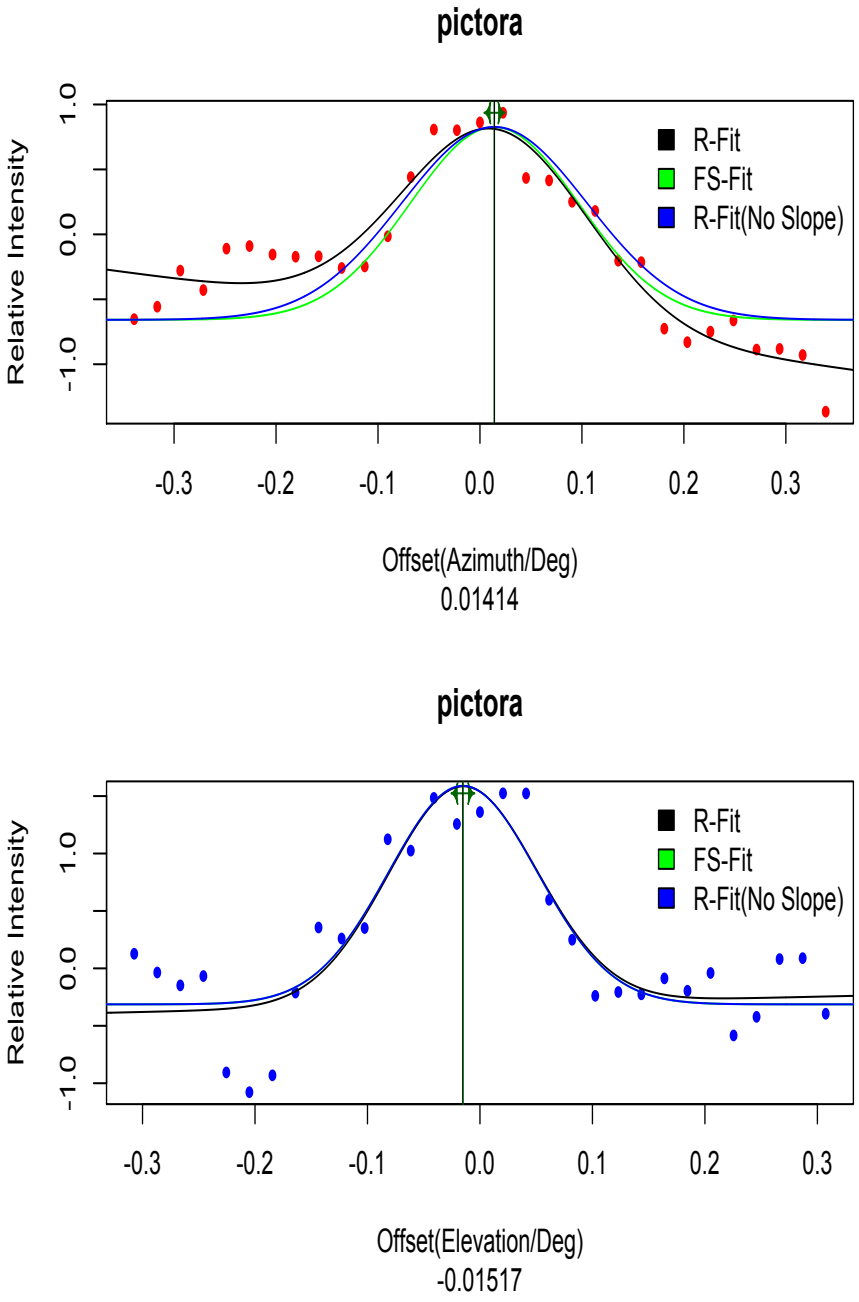

Figure B.22: 31-Step Scan plot of Pictor A

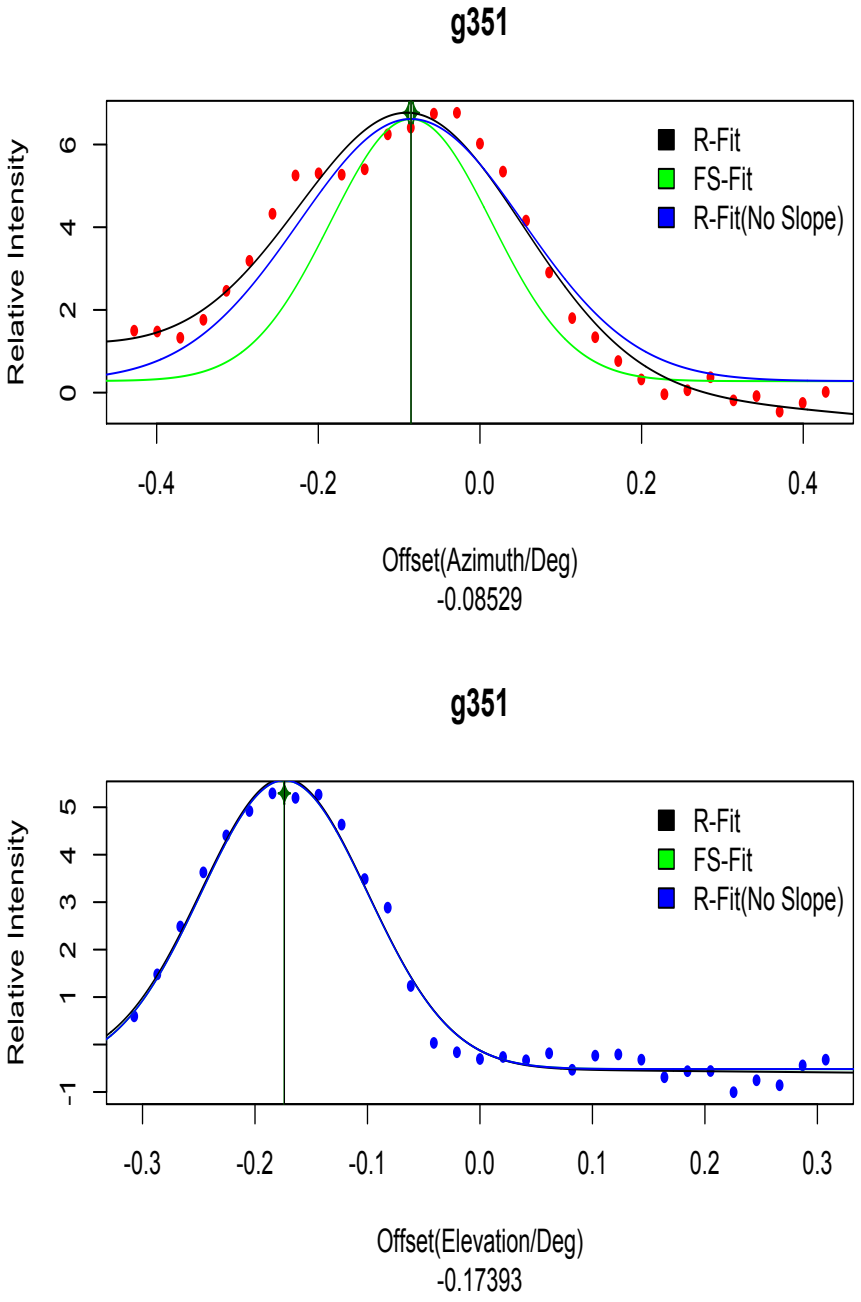

Figure B.23: 31-Step Scan plot of methanol maser G351

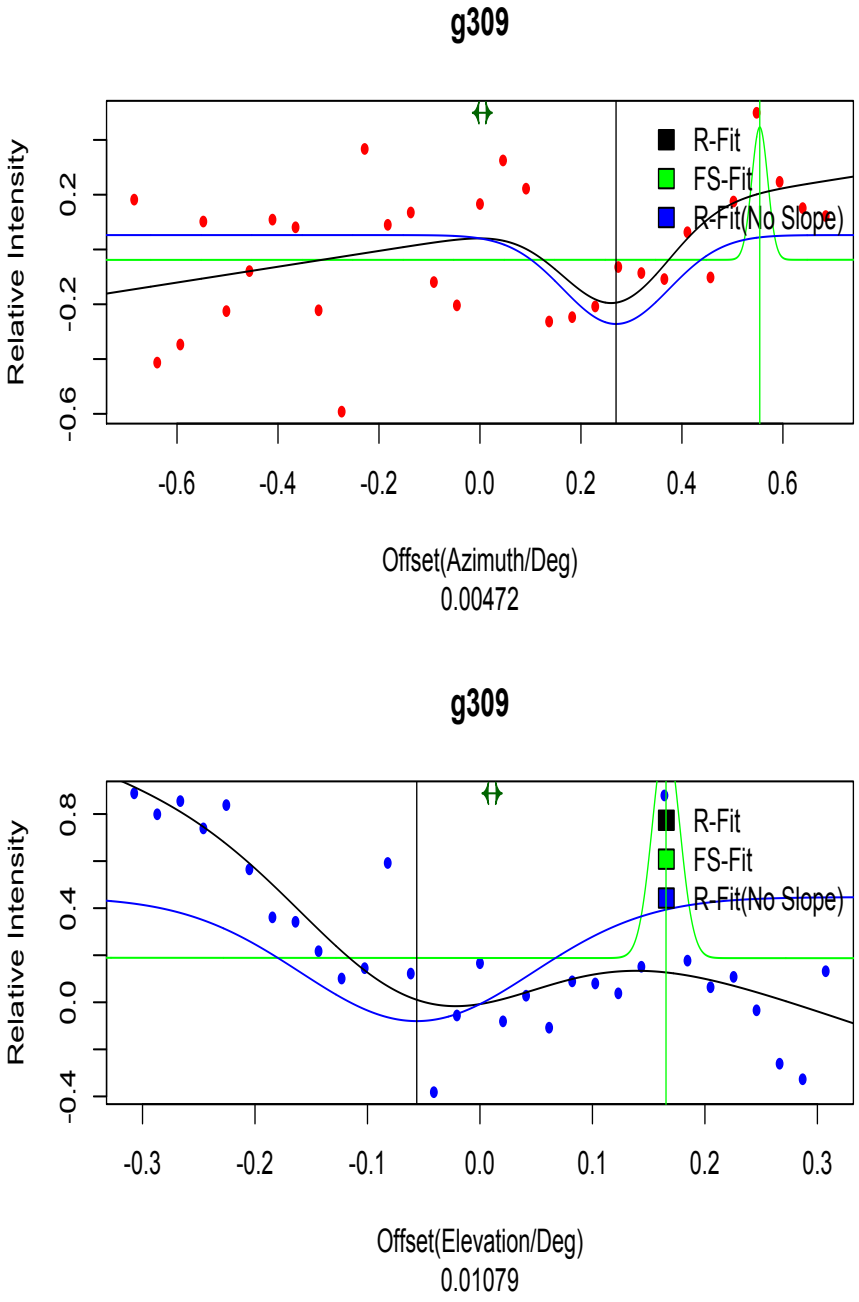

Figure B.24: 31-Step Scan plot of methanol maser G309

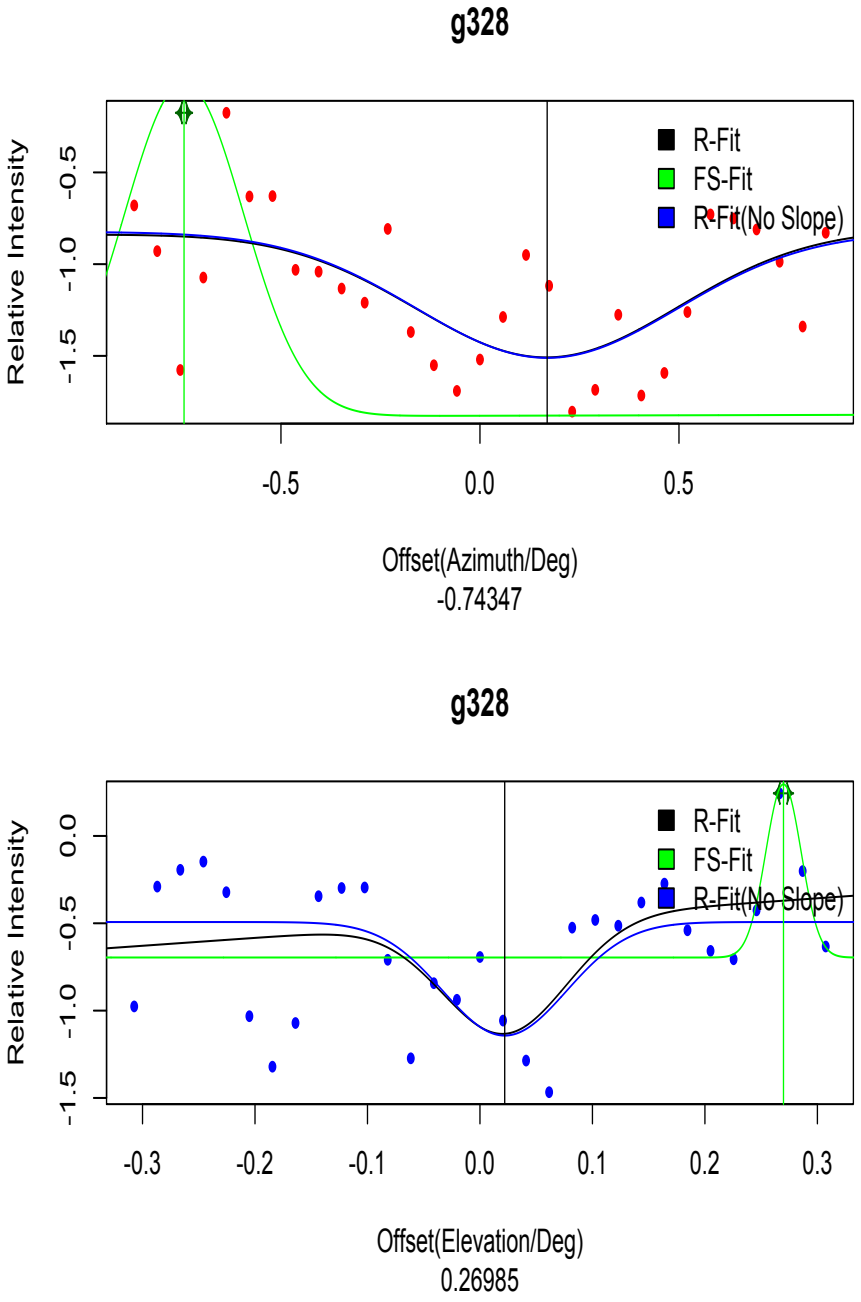

Figure B.25: 31-Step Scan plot of methanol maser G328

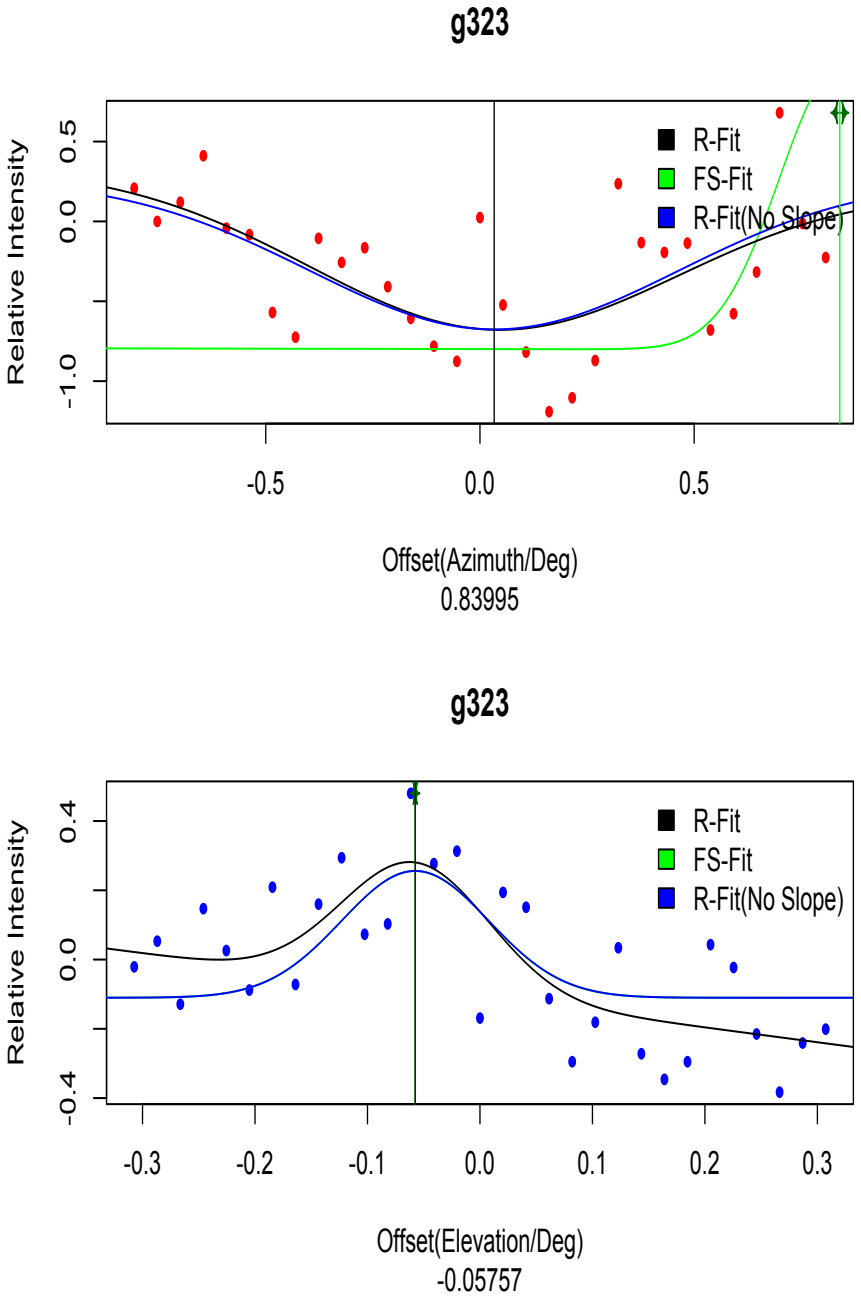

Figure B.26: 31-Step Scan plot of methanol maser G323

Appendix C

Bash and R code

C.1 Bash code

```
#########Lat scan file ###################################
grep -w fivpt#lat* log.txt >> PwrReadLat1.txt
grep -v  fivpt#latfit* PwrReadLat1.txt >> PwrReadLat2.txt
grep -v fivpt#laterr* PwrReadLat2.txt >> PwrReadLatF.txt
cat PwrReadLatF.txt | awk '{print $2,$3,$4,$5,$6}' >> Latscan.txt

#######Lon scan file ######################################

grep -e fivpt#lon* log.txt >> PwrReadLon1.txt
grep -v fivpt#lonfit* PwrReadLon1.txt >> PwrReadLon2.txt
grep -v fivpt#lonerr* PwrReadLon2.txt >> PwrReadLonF.txt
cat PwrReadLonF.txt | awk '{print $2,$3,$4,$5,$6}' >> Lonscan.txt

###########################################################
```

```
########### Lat fit, lat Err, lonfit, lon_err, source#######
########### offset, xoffset,source ########################

grep fivpt#offset* log.txt  >> offset1.txt
cat offset1.txt | awk '{print $2,$3,$4,$5,$6,$7}' >> offset.txt

grep fivpt#xoffset* log.txt >> xoffset1.txt
cat xoffset1.txt | awk '{print $2,$3,$4,$5,$6, $7, $8, $9,$10}' >> xoffset.txt

grep fivpt#latfit* log.txt >> latfit1.txt
cat latfit1.txt | awk '{print $2, $3, $4, $5, $6, $7}' >> latfit.txt

grep fivpt#laterr* log.txt >> laterr1.txt
cat laterr1.txt | awk '{print $2, $3, $4, $5, $6}' >> laterr.txt


grep fivpt#lonfit* log.txt >> lonfit1.txt
cat lonfit1.txt | awk '{print $2, $3, $4, $5, $6, $7}' >> lonfit.txt

grep fivpt#lonerr* log.txt >> lonerr1.txt
cat lonerr1.txt | awk '{print $2, $3, $4, $5, $6}' >> lonerr.txt

grep fivept#source log.txt >> source1.txt
cat source1.txt | awk '{print $2, $3, $4, $5, $6}' >> source.txt

### Removing Unneccessary file#######

rm PwrReadLat1.txt
rm PwrReadLat2.txt
rm PwrReadLon1.txt
rm PwrReadLon2.txt
```

```
rm PwrReadLatF.txt

rm PwrReadLonF.txt

rm offset1.txt

rm xoffset1.txt

rm latfit1.txt

rm laterr1.txt

rm lonfit1.txt

rm lonerr1.txt

rm source1.txt


#end

#########################################################################
```

C.2 R code

```
######## Pointing Data Import ################

library(aspace)
library(minpack.lm)
library(zoom)

########Importing Data############

LonScan <- read.table(file.choose())
colnames(LonScan) <- c("LonPointNo", "LonTime",
"LonOffset", "LonTemp", "LonRMS")
head(LonScan)
dim(LonScan)
table(LonScan$LonPointNo)

LatScan <- read.table(file.choose())
colnames(LatScan) <- c("LatPointNo", "LatTime",
"LatOffset", "LatTemp", "LatRMS")
head(LatScan)
dim(LatScan)
table(LatScan$LatPointNo)


#Importing the FS fitting parameter Files

LonFit <- read.table(file.choose())
colnames(LonFit) <- c("LonGPeakOffset", "LonFWHM",
"LonPeakTemp", "LonOffset", "LonSlope", "LonGoodFit")
```

```
head(LonFit)
dim(LonFit)

LatFit <- read.table(file.choose())
colnames(LatFit) <- c("LatGPeakOffset",
 "LatFWHM", "LatPeakTemp", "Latoffset", "LatSlope", "LatGoodFit")
dim(LatFit)

## Source is extracted from the final XElevation scan file

XElvOffset <- read.table(file.choose())
colnames(XElvOffset) <- c("AZM", "ELV",
"ERR_XELV", "ERR_ELV", "RMSXELV", "RMSELV",
"AZFIT","ELVFIT","Source")
head(XElvOffset)
dim(XElvOffset)


#Extracting Source name from XELVoffset

Source <- XElvOffsetSource

#Concatinating Lon Scan, Lat scan, source and good Fit (both Lon and Lat)

######################
#Enter No of Points###
##
Points = 9 ##
##
######################
```

```
Source4Scan <- rep(Source, each = Points)
LonGoodFit <- rep(LonFit$LonGoodFit, Points)
LatGoodFit <- rep(LatFit$LatGoodFit, Points)
PwrScan <- cbind(LonScan, LatScan, Source4Scan,
 LonGoodFit, LatGoodFit)

#Concatinating LonFit (FS), LatFit(FS) and source

FSFitPar <- cbind(LonFit,LatFit,Source)



##### Functions ############


############################################################
#Writing RMS function                          ############
rms <- function (x) {                          ############
sqrt(mean(x^2))                              ############
}                                              ############
############################################################


############################################################
############################################################
Fit <- function(ms,cs,ag,xg,bg,cg) {(ms*offset + cs) + ##
(ag * exp(-(offset-bg)^2/(2*cg^2)))}              ##
############################################################
############################################################
```

```
###Plotting Algorithm

#Source
################################################################################
30dori, 3c84, centa, ctb31, ctb32, cygnusa, g309, g323, g328, g351, ngc3603
ngc6618, oriona, pictora, sgra, taurusa
################################################################################

###############################
#Enter Source Name            #
PlotSource = "taurusa"         #
###############################

#########################
#Observation Number      #
  o = 1              #
#########################

SourceSubset <- subset(PwrScan, Source4Scan == PlotSource)

SourceScan <- subset(SourceSubset, LonGoodFit > 0 & LatGoodFit > 0 )

#####################################################################
    #Enable to look at failed (termed by FS) plots)

#SourceScan <- subset(SourceSubset, LonGoodFit < 0 | LatGoodFit < 0 )

#####################################################################
#Enter Step to plot

nrow(SourceScan)/Points
```

```
obs<- seq(1,1000,by=Points)


n = obs[o]
m = n + (Points-1)
z=o

#Fitting with the FS estimated parameter

FSFitSubset <- subset(FSFitPar, FSFitPar$Source == PlotSource)
FSFitSource <- subset(FSFitSubset, LonGoodFit >0 & LatGoodFit >0 )


#################################################################
    Enable to look at failed (termed by FS) plots)
FSFitSource <- subset(FSFitSubset, LonGoodFit <0 | LatGoodFit <0 )
#################################################################


#Extracting FS parameters
SlopeLonFS <- FSFitSource[z,5];  SlopeLatFS <- FSFitSource[z,11]
CLonFS <- FSFitSource[z,4];
CLatFS <-as.numeric(paste(FSFitSource[z,10]));
AmpLonFS <- FSFitSource[z,3];
AmpLatFS <- as.numeric(paste(FSFitSource[z,9]))
MeanLonFS <- FSFitSource[z,1];
MeanLatFS <-as.numeric(paste(FSFitSource[z,7]))
SdvLonFS <- as.numeric(paste(FSFitSource[z,2]))/2.35482
SdvLatFS <- as.numeric(paste(FSFitSource[z,8]))/2.35482
```

```
#Fitting with my own estimated parameter

#Fitting for Longitude/Azimuth

SlopeLonEs <- (SourceScan[m,4]
- SourceScan[n,4])/(SourceScan[m,3]-SourceScan[n,3])
CLonEs <- SourceScan[n,4] - (SlopeLonEs * SourceScan[n,3])
AmpLonEs <- max(SourceScan[n:m,4])
offset <- seq(-1,1,0.001)
MeanLonEs <- mean(SourceScan[n:m,3])
SdvLonEs <- sd(SourceScan[n:m,3])

#NLS on Longitude/Azimuth

xLn <- SourceScan[n:m,3]
yLn <- SourceScan[n:m,4]

fitLn <- yLn~((ms*xLn +c)+(ag * exp(-(xLn-bg)^2/(2*cg^2))))

library(minpack.lm)
EsCoefLon <-nlsLM(fitLn,start=list(ms=SlopeLonEs,c=CLonEs
                  ,ag=AmpLonEs,bg=0,cg=SdvLonEs),trace=TRUE)
summary(EsCoefLon)

msLonls <- coef(EsCoefLon)[1]
csLonls <- coef(EsCoefLon)[2]
agLonls <- coef(EsCoefLon)[3]
xgLonls <- offset
bgLonls <- coef(EsCoefLon)[4]
cgLonls <- coef(EsCoefLon)[5]
```

```
#Fitting for Latitude/Elevation

SlopeLatEs <- (SourceScan[m,9] - SourceScan[n,9])/(SourceScan[m,8]-
               SourceScan[n,8])
CLatEs <- SourceScan[n,9] - SlopeLatEs * SourceScan[n,8]
AmpLatEs <- max(SourceScan[n:m,9])
MeanLatEs <- median(SourceScan[n:m,8])
SdvLatEs <- sd(SourceScan[n:m,8])

#NLS on Lat/Elevation



xLt <- SourceScan[n:m,8]
yLt <- SourceScan[n:m,9]

fitLt <- yLt~((ms*xLt +c)+(ag * exp(-(xLt-bg)^2/(2*cg^2))))

EsCoefLat <-nlsLM(fitLt,start=list(ms=SlopeLatEs,c=CLatEs,
            ag=AmpLatEs,bg=MeanLatEs,cg=SdvLatEs), trace=TRUE)
summary(EsCoefLat)

msLatls <- coef(EsCoefLat)[1]
csLatls <- coef(EsCoefLat)[2]
agLatls <- coef(EsCoefLat)[3]
xgLatls <- offset
bgLatls <- coef(EsCoefLat)[4]
cgLatls <- coef(EsCoefLat)[5]
```

```
#Plotting scan in Longitude/Azimuth and Latitude /Elevation
dev.new()
par(mfrow=c(2,1))

#Azimuth/longitude

plot(SourceScan$LonOffset[n:m], SourceScan$LonTemp[n:m],
      xlab="Offset(Azimuth)", ylab="Temperature",main = PlotSource,
      sub=FSOffset_AZM, col="red", pch=20)

#identify(SourceScan$LonOffset[n:m], SourceScan$LonTemp[n:m])

#FS Parameter
lines(offset, Fit(SlopeLonFS,CLonFS,
      AmpLonFS,offset,MeanLonFS,SdvLonFS), col="green")

#R estimated Parameter

lines(offset, Fit(msLonls,csLonls,agLonls,xgLonls,bgLonls,cgLonls))



lines(offset, Fit(msLonls,csLonls,agLonls,
       xgLonls,bgLonls,cgLonls)-(msLonls*offset), col="blue")
legend("topright", c("R-Fit", "FS-Fit", "R-Fit(No Slope)"), fill=c("black",
       "green","blue"), , box.lty=0)



FSOffset_AZM <-  MeanLonFS
ESOffset_AZM <-  bgLonls

print (FSOffset_AZM)
```

```
print(ESOffset_AZM)


abline(v=FSOffset_AZM, col="green")
abline(v=ESOffset_AZM)



#Elevation/Latitude

plot(SourceScan$LatOffset[n:m], SourceScan$LatTemp[n:m],
     xlab="Offset(Elevation)", ylab="Temperature",
     main = PlotSource,sub = FSOffset_ELV , col="blue", pch=20)

lines(offset, Fit(SlopeLatFS,CLatFS,AmpLatFS,offset,MeanLatFS,SdvLatFS),
      col="green")

lines(offset, Fit(msLatls,csLatls,agLatls,xgLatls,bgLatls,cgLatls))

lines(offset, Fit(msLatls,csLatls,agLatls,
      xgLatls,bgLatls,cgLatls)-(msLatls*offset), col="blue")
legend("topright", c("R-Fit", "FS-Fit",
       "R-Fit(No Slope)"), fill=c("black", "green","blue"), box.lty=0)



FSOffset_ELV <-  MeanLatFS
ESOffset_ELV <-  bgLatls


abline(v = FSOffset_ELV, col="green")
abline ( v = ESOffset_ELV)
```

```
#########################################################################
#########################################################################
#########################################################################
#########################################################################

## Need to add the azimuth error in the XElvOffsetCB
as in only contains XELV Error

library(aspace)
ERR_AZM <- XElvOffset$ERR_XELV/cos_d(XElvOffset$ELV)
ErrorG <- cbind(XElvOffset, ERR_AZM)
ErrorF <- subset(ErrorG,  AZFIT==1 & ELVFIT==1)


#########################################################################
##Plotting Historgram of Raw Offsets
dev.new()
par(mfrow=c(2,2))

hist(ErrorF$ERR_AZM, nclass=20, xlab="Azimuth Offsets",
     main="Histogram(Azimuth Offsets)", col="blue", prob=TRUE
     , ylim=c(0,9))
hist(ErrorF$ERR_ELV, nclass=20, xlab="Elevation Offsets",
     main="Histogram(Elevation Offsets)", col="blue",
     prob="TRUE", ylim=c(0,9))

#### Boxplot to detect outliers

boxplot(ErrorF$ERR_AZM, col="red", ylab="Azimuth Offsets",
        main="Boxplot(Azimuth Offsets)")
```

```
boxplot(ErrorF$ERR_ELV, col="red", ylab="Elevation Offsets",
        main="Boxplot(Elevation Offsets)")

summary(ErrorF$ERR_AZM)
summary(ErrorF$ERR_ELV)

###Sperating the dataset from outliers using IQR

library(fGarch)
library(timeDate)
library(timeSeries)
snormFit(ErrorF$ERR_AZM)

AzmUpLimIQR <- median(ErrorF$ERR_AZM) + 1.5* IQR(ErrorF$ERR_AZM)
AzmLoLimIQR <- median(ErrorF$ERR_AZM) - 1.5* IQR(ErrorF$ERR_AZM)

ElvUpLimIQR = median(ErrorF$ERR_ELV) + 1.5 * IQR(ErrorF$ERR_ELV)
ElvLoLimIQR = median(ErrorF$ERR_ELV) - 1.5 * IQR(ErrorF$ERR_ELV)


Error <- subset(ErrorF,  ERR_AZM > AzmLoLimIQR & ERR_AZM < AzmUpLimIQR &
                ERR_ELV > ElvLoLimIQR & ERR_ELV < ElvUpLimIQR
                & Source !="centa" & Source !="30dori" & Source
                != "ctb32" & Source !="pictora" & Source !="g351"
                & Source !="g18895")# & Source !="centa")

dev.new()

par(mfrow=c(2,2))

hist(Error$ERR_AZM, nclas=20, prob=TRUE, col="blue",
```

```
     xlab="Azimuth Offsets (outliers removed)",
     main="Histogram(Azimuth Offsets)")

array <- seq(-0.30,0.30,by=0.001)
lines(array,dnorm(array,median(Error$ERR_AZM), sd(Error$ERR_AZM)),
      col="red")
lines(array,dnorm(array,mean(Error$ERR_AZM), sd(Error$ERR_AZM)),
      col="green")
legend("topright", c("Mean", "Median"), fill=c("green", "red"), box.lty=0)


hist(Error$ERR_ELV, nclas=20, prob=TRUE, col="blue",
     xlab="Elevation Offsets (outliers removed)",
     main="Histogram(Elevation Offsets)")
lines(array,dnorm(array,median(Error$ERR_ELV), sd(Error$ERR_ELV)),
      col="red")
lines(array,dnorm(array,mean(Error$ERR_ELV), sd(Error$ERR_ELV)),
      col="green")
legend("topright", c("Mean", "Median"), fill=c("green", "red"),
      box.lty=0)


boxplot(Error$ERR_AZM, col="red", ylab="Azimuth Offsets",
        xlab="outliers removed", main="Boxplot(Azimuth Offsets)")
boxplot(Error$ERR_ELV, col="red", ylab="Elevation Offsets",
        xlab="outliers removed", main="Boxplot(Elevation Offsets)")

###Test for Normality#####
par(mfrow=c(1,2))
qqnorm(Error$ERR_AZM, col="red", sub="Azimuth Offsets")
qqline(Error$ERR_AZM, col="blue")
```

```
qqnorm(Error$ERR_ELV, col="red", sub="Elevation Offsets")
qqline(Error$ERR_ELV, col="blue")



########################################################################
VONDERMONDE MATRIX TO CALCULATE THE COEFFICIENTS
########################################################################
#### Vandermonde Matrix############



## Creating Azimuth Matrix

P1 <- rep.int(1, length(Error$AZM))
X1 <- rep.int(0, length(Error$AZM))
X2 <- rep.int(0, length(Error$AZM))
X3 <- rep.int(0, length(Error$AZM))
X4 <- rep.int(0, length(Error$AZM))
X5 <- rep.int(0, length(Error$AZM))

library(aspace)
AzimVal <- c(P1, tan_d(Error$ELV), - 1/cos_d(Error$ELV),
             sin_d(Error$AZM) * tan_d(Error$ELV),
             -(cos_d(Error$AZM) * tan_d(Error$ELV)),
              X1, X2, X3, X4, X5)


AzmMatrix <- matrix(data = AzimVal, nrow=length(Error$AZM), ncol= 10)
```

```
## Creating Elevation Matrix


P7 <- rep.int(1,length(Error$AZM))
Y1 <- rep.int(0, length(Error$AZM))
Y2 <- rep.int(0, length(Error$AZM))
Y3 <- rep.int(0, length(Error$AZM))

ElvVal <-  c(Y1,Y2,Y3,cos_d(Error$AZM),
          sin_d(Error$AZM), P7, cos_d(Error
           $ELV), cos_d(8 * Error$ELV), sin_d(8*Error$ELV),
           1/tan_d(Error$ELV))


ElvMatrix <- matrix(data=ElvVal, nrow = length(Error$ELV), ncol = 10 )


##Joining the two Matrix Together

VonMat <- rbind(AzmMatrix, ElvMatrix)

## Creating a single Matrix of both Azimuth and Elevation Errors

AzmError <- Error$ERR_AZM
ElvError <- Error$ERR_ELV
Offset <- c(AzmError,ElvError)

####Creating Weights for LS Fit#######################

WeightAz <- Error$RMSXELV/cos_d(Error$ERR_ELV)
WeightEl <- Error$RMSELV
Weight <- c(WeightAz, WeightEl)
```

```
##Least Square Fitting

LSFIT <- lsfit(VonMat,Offset, intercept = FALSE)
LSREG <- lm(Offset~VonMat)

P1  <- LSFIT$coef[1]
P3  <- LSFIT$coef[2]
P4  <- LSFIT$coef[3]
P5  <- LSFIT$coef[4]
P6  <- LSFIT$coef[5]
P7  <- LSFIT$coef[6]
P8  <- LSFIT$coef[7]
P19 <- LSFIT$coef[8]
P20 <- LSFIT$coef[9]
P23 <- LSFIT$coef[10]

##Azimuth Error Plots



#Projecting Azimuth Errors using the coefficient:

DelAzErrors <- P1 + P3 * tan_d(Error$ELV)  - P4 * 1/cos_d(Error$ELV) + P5*
sin_d(Error$AZM) * tan_d(Error$ELV) - P6 * cos_d(Error$AZM)
* tan_d(Error$ELV)

dev.new()
par(mfrow=c(2,1))

#Plots
```

```
plot(Error$AZM, DelAzErrors, col="blue", ylim=c(-0.15,0.15),main="Azimuth
offsets against Azimuth", xlab="Azimuth/Degree", ylab="Azimuth offsets/
Degree") #Projected Error Plots
points(Error$AZM, Error$ERR_AZM, col="red", pch=20) # Actual error plots
abline(h=0)
legend("topright", c("Actual offsets", "Modelled offsets"), fill=c("red",
 "blue"),, box.lty=0)

residualAz <- DelAzErrors - AzmError
plot(Error$AZM, residualAz, pch=20, col="darkgreen", xlab="Azimuth/Degree",
ylab="Residuals/Degree", main="Azimuth Residuals Plot", ylim=c(-0.15, 0.15))

abline(h=0)

# Projecting Elevation Errors using the coefficient:

DelElvErrors<- P5 * cos_d(Error$AZM) + P6 * sin_d(Error$AZM)+
P7 + P8 * cos_d(Error$ELV) + P19 * cos_d(8*Error$ELV) +
P20 * sin_d(8*Error$ELV) + P23 * 1/tan_d(Error$ELV)

dev.new()
par(mfrow=c(2,1))

##Plottng elevation error against elevation:

plot(Error$ELV, DelElvErrors ,ylim=c(-0.3,0.3),
xlab="Elevation/Degree", ylab="Elevation offsets/Degree",
col="blue", main = "Elevation offset against Elevation")
points(Error$ELV, Error$ERR_ELV, col="red", pch=20)# Actual error plots
abline(h=0)
legend("topright", c("Actual offsets", "Modelled offsets"),
```

```
fill=c("red", "blue"), box.lty=0)

residualEl <- DelElvErrors - Error$ERR_ELV

#Residuals
plot(Error$ELV,residualEl, pch=20, col="darkgreen", ylim=c(-0.15,0.15),
     xlab="Elevation/Degree", ylab="Residuals/Degree",
      main="ELevation Residuals Plot") # Residuals
abline(h=0)
##########################################################################
##########################################################################
##########################################################################
Plotting Azimuth errors against elevation and
elevation errors against Azimuth
##########################################################################
##########################################################################
##########################################################################

dev.new()

par(mfrow=c(2,1))
### Azimuth Errors against ELevation
plot(Error$ELV, DelAzErrors, col="blue", ylim=c(-0.30,0.30),
main="Azimuth offsets against Elevation(My Coeff)",
      xlab="Elevation/Degree", ylab="Azimuth offsets/Degree")
       #Projected Error Plots
points(Error$ELV, Error$ERR_AZM, col="red", pch=20) #
Actual error plots
abline(h=0)
legend("topright", c("Actual Errors", "Modelled Errors"),
fill=c("red", "blue"),, box.lty=0)
```

```
residualAz <- DelAzErrors - AzmError
plot(Error$ELV, residualAz, pch=20, col="darkgreen",
main="Azimuth Residuals Plot", xlab="Elevation/Degree",
       ylab="Residuals/Degree", ylim=c(-0.15,0.15) )
abline(h=0)



dev.new()
par(mfrow=c(2,1))
###Elevation Errors against Azimith
plot(Error$AZM, DelElvErrors ,ylim=c(-0.3,0.3),
xlab="Azimuth/Degree", ylab="Elevation offsets/Degree",
col="blue", main = "Elevation offsets against Azimuth(My Coeff)")
points(Error$AZM, Error$ERR_ELV, col="red", pch=20) # Actual error plots
abline(h=0)
residualEl <- DelElvErrors - Error$ERR_ELV
legend("topright", c("Actual Errors", "Modelled Errors"),
       fill=c("red", "blue"), box.lty=0)

plot(Error$AZM,residualEl, pch=20, col="darkgreen",
main="Elevation Residual Plot", xlab="Azimuth/Degree",
 ylab="Residuals/Degree", ylim=c(-0.15,0.15))
abline(h=0)
print(P1)
print(P3)
print(P4)
print(P5)
print(P6)
print(P7)
```

```
print(P8)
print(P19)
print(P20)
print(P23)

rms(Error$ERR_AZM)
rms(Error$ERR_ELV)



rms(residualEl)
rms(residualAz)




#y <- residualAz
#x <- Error$AZM
#dev.new()
#model <- lm(y~cos_d(2*x))

#xx <- seq(0,360,1)
#yy <-  coef(model)[2]*cos_d(2*x)

#plot(x,y)
#points(x,yy)

#rms(yy-y)

#pp <- data.frame(x,y)

#write.table(pp, file="AzOffset")
```

```
###################################
Codes used for Figure 1.4
###################################

plot(SourceScan$LatOffset[n:m]-0.02538, SourceScan$LatTemp[n:m],
     xlab="Offset/Degree", ylab="Relative Temperature",
    main = "The 30 metre beam (With Taurus A)" ,
    col="blue", pch=20, xlim=c(-0.15,0.15))

lines(offset-0.02538, Fit(msLatls,csLatls,agLatls,
      xgLatls,bgLatls,cgLatls), col="red")

b <- mean(SourceScan$LatOffset[n:m]-0.02538)
a <- max(SourceScan$LatTemp[n:m])
c <- sd(SourceScan$LatOffset[n:m]-0.02538)

abline(h=21.943, lty=4, col="grey")
abline(v=-0.047, lty=4, col="grey")
abline(v= 0.047, lty=4, col="grey")

###################################
Codes used for Figure 4.1
###################################

plot(SourceScan$LatOffset[n:m]-0.02538, SourceScan$LatTemp[n:m],
     xlab="Offset/Degree", ylab="Relative Temperature",
     main = "The 30 metre beam (With Taurus A)" ,
     col="blue", pch=20, xlim=c(-0.15,0.15))
```

```
lines(offset-0.02538, Fit(msLatls,csLatls,agLatls,
      xgLatls,bgLatls,cgLatls), col="red")



segments(x0=0.052,y0=-3,x1=0.052,y1=21.943, col="blue", lty=4)
segments(x0=-0.052,y0=-3,x1=-0.052,y1=21.943, col="blue", lty=4)
segments(x0=-0.014,y0=-3,x1=-0.014,y1=41, col="red", lty=4)
segments(x0=0.014,y0=-3,x1=0.014,y1=41, col="red", lty=4)
legend("topright", c("FWHM(~0.085)",
        "Current model(rms:0.014)","New model(rms:0.008)"),
        fill=c("blue","red","grey"),box.lty=0)


cord.x <- c(-0.0085)
cord.y <- c(-5)

#2nd Vertices

cord.x <- c(cord.x,-0.0085)
cord.y <- c(cord.y,43)

#3rd Vertices

cord.x <- c(cord.x,0.0085,0.0085)
cord.y <- c(cord.y,43,-5)

polygon(cord.x,cord.y,col="grey")
segments(x0=0,y0=-3,x1=0,y1=44)
```

```
###################################
Codes used for Source Analysis
###################################



par(mfrow=c(2,1))
par(bg="darkgrey")
plot(ErrorG$AZM, ErrorG$ELV, col=c("blue","blue",
     "blue", "red",  "green","red","green","green","green",
     "green","green","red","red","red",
     "green","red","red") [ErrorG$Source], xlab="Azimuth/Degree",
     ylab="Elevation/Degree", pch=4)


##SUbsetting Strong and Moderate Sources


goodSource <- subset(ErrorG, ErrorG$Source == "taurusa"
                     | ErrorG$Source == "cygnusa"
                     | ErrorG$Source =="oriona" |
                     ErrorG$Source == "ngc6618" |
                     Source =="ctb31" | Source =="sgra" |
                     Source =="ngc3603" & Source == "centa" |
                     Source == "3c84" | Source == "30dori")
```

```
plot(goodSource$AZM, goodSource$ELV, col=c("blue","blue","blue", "red",
      "red","red","red","red","red","red") [ErrorG$Source],
      xlab="Azimuth/Degree", ylab="Elevation/Degree", pch=4)

##Strong Sources

taurusa <- subset(ErrorG, Source == "taurusa")
cygnusa <- subset(ErrorG, Source == "cygnusa")
oriona <- subset(ErrorG, Source == "oriona")
ngc6618 <- subset(ErrorG, Source == "ngc6618")
ctb31 <- subset(ErrorG, Source == "ctb31")
sgra <- subset(ErrorG, Source == "sgra")
ngc3603 <- subset(ErrorG, Source == "ngc3603")

##Moderate Sources

centa <- subset(ErrorG, Source == "centa")
s3c84 <- subset(ErrorG, Source == "3c84")
s30dori <- subset(ErrorG, Source == "30dori")



##Weak Source
ctb32 <- subset(ErrorG, Source == "ctb32")
pictora <- subset(ErrorG, Source == "pictora")
g351 <- subset(ErrorG, Source == "g351")
g18895 <- subset(ErrorG, Source == "g18895")
g328 <- subset(ErrorG, Source == "g328")
g323 <- subset(ErrorG, Source == "g323")
g309 <- subset(ErrorG, Source == "g309")
```

```
##Plotting the Sources
par(mfrow=c(2,1))


##Strong Source
plot(taurusa$AZM, taurusa$ELV, pch=4, col="red",
     xlab="Azimuth/Degree", ylab="Elevation/Degree",
      xlim=c(0,360), ylim=c(0,110),
      main="Sky coverage(Strong, moderate, weak sources)")

abline(h=90, col="grey")
points(cygnusa$AZM, cygnusa$ELV, pch=4, col="red",
        xlab="Azimuth/Degrees", ylab="Elevation/Degrees")
points(oriona$AZM, oriona$ELV, pch=4, col="red",
       xlab="Azimuth/Degrees", ylab="Elevation/Degrees")
points(ngc6618$AZM, ngc6618$ELV, pch=4, col="red",
       xlab="Azimuth/Degrees", ylab="Elevation/Degrees")
points(ctb31$AZM,  ctb31$ELV, pch=4, col="red",
       xlab="Azimuth/Degrees", ylab="Elevation/Degrees")
points(sgra$AZM, sgra$ELV, pch=4, col="red",
       xlab="Azimuth/Degrees", ylab="Elevation/Degrees")
points(ngc3603$AZM, ngc3603$ELV, pch=4, col="red",
        xlab="Azimuth/Degree", ylab="Elevation/Degree")

##Moderate Source

points(centa$AZM, centa$ELV, pch=4, col="blue",
       xlab="Azimuth/Degrees", ylab="Elevation/Degrees")
points(s3c84$AZM, s3c84$ELV, pch=4, col="blue",
```

```
       xlab="Azimuth/Degrees", ylab="Elevation/Degrees")
points(s30dori$AZM, s30dori$ELV, pch=4, col="blue",
       xlab="Azimuth/Degrees", ylab="Elevation/Degrees")
##Weak Source

points(ctb32$AZM, ctb32$ELV, pch=4, col="green",
        xlab="Azimuth/Degrees", ylab="Elevation/Degrees")
points(pictora$AZM, pictora$ELV, pch=4, col="green",
        xlab="Azimuth/Degrees", ylab="Elevation/Degrees")
points(g351$AZM, g351$ELV, pch=4, col="green",
        xlab="Azimuth/Degrees", ylab="Elevation/Degrees")
points(g18895$AZM, g18895$ELV, pch=4, col="green",
        xlab="Azimuth/Degrees", ylab="Elevation/Degrees")
points(g309$AZM, g309$ELV, pch=4, col="green",
        xlab="Azimuth/Degrees", ylab="Elevation/Degrees")
points(g328$AZM, g328$ELV, pch=4, col="green",
        xlab="Azimuth/Degrees", ylab="Elevation/Degrees")
points(g323$AZM, g323$ELV, pch=4, col="green",
        xlab="Azimuth/Degree", ylab="Elevation/Degree")
legend("topright", c("Strong", "Moderate", "Weak"),
       fill=c("red", "blue","green"), box.lty=0, horiz=TRUE)



##Plotting Strong and Moderate Sources

plot(taurusa$AZM, taurusa$ELV, pch=4, col="red",
      xlab="Azimuth/Degree", ylab="Elevation/Degree",
      xlim=c(0,360), ylim=c(0,110),
       main="Sky coverage(Strong and moderate sources)")
points(cygnusa$AZM, cygnusa$ELV, pch=4, col="red",
```

```
      xlab="Azimuth/Degrees", ylab="Elevation/Degrees")

points(oriona$AZM, oriona$ELV, pch=4, col="red",
      xlab="Azimuth/Degrees", ylab="Elevation/Degrees")
points(ngc6618$AZM, ngc6618$ELV, pch=4, col="red",
      xlab="Azimuth/Degrees", ylab="Elevation/Degrees")
points(ctb31$AZM,  ctb31$ELV, pch=4, col="red",
      xlab="Azimuth/Degrees", ylab="Elevation/Degrees")
points(sgra$AZM, sgra$ELV, pch=4, col="red",
      xlab="Azimuth/Degrees", ylab="Elevation/Degrees")
points(ngc3603$AZM, ngc3603$ELV, pch=4, col="red",
      xlab="Azimuth/Degrees", ylab="Elevation/Degrees")

##Moderate Source

#points(centa$AZM, centa$ELV, pch=4, col="blue",
       xlab="Azimuth/Degrees", ylab="Elevation/Degrees")
points(s3c84$AZM, s3c84$ELV, pch=4, col="blue",
       xlab="Azimuth/Degrees", ylab="Elevation/Degrees")
points(s30dori$AZM, s30dori$ELV, pch=4, col="blue",
       xlab="Azimuth/Degree", ylab="Elevation/Degree")
abline(h=90, col="grey")
legend("topright", c("Strong", "Modrate"),
      fill=c("red", "blue"), box.lty=0, xpd=TRUE, horiz=TRUE)



###Scaling the Azimuth of the Sources from -180 to 180

ErrorSortAzm <- Error[order(Error$AZM),]
AZMScaled <- c(ErrorSortAzm$AZM[1:79],(ErrorSortAzm$AZM[80:156] - 360)
```

```
OffsetSort <- data.frame(ErrorSortAzm, AZMScaled)

### Checking the residuals of the offsets with respect to a quadratic fit

##Strong Sources
taurusa <- subset(ErrorG, Source == "taurusa")
cygnusa <- subset(ErrorG, Source == "cygnusa")
oriona <- subset(ErrorG, Source == "oriona")
ngc6618 <- subset(ErrorG, Source == "ngc6618")
ctb31 <- subset(ErrorF, Source == "ctb31")
sgra <- subset(ErrorG, Source == "sgra")
ngc3603 <- subset(ErrorG, Source == "ngc3603")

##Moderate Sources

centa <- subset(ErrorF, Source == "centa")
s3c84 <- subset(ErrorG, Source == "3c84")
s30dori <- subset(ErrorF, Source == "30dori")

##Weak Source
ctb32 <- subset(ErrorF, Source == "ctb32")
pictora <- subset(ErrorF, Source == "pictora")
g351 <- subset(ErrorG, Source == "g351")
g18895 <- subset(ErrorG, Source == "g18895")
g328 <- subset(ErrorG, Source == "g328")
g323 <- subset(ErrorG, Source == "g323")
g309 <- subset(ErrorG, Source == "g309")


##Fitting Algorithm
```

```
Source = pictora

par(mfrow=c(1,2))

plot(Source$ELV, Source$ERR_ELV, pch=20, col="red",
 xlab="Elevation/deg", ylab="Elevation Offsets/deg", main="Pictor A")

model <- lm(Source$ERR_ELV~Source$ELV)

abline(model, col="blue")

model
Rsquared=summary(model)$r.squared
Rsquared
sd(model$residuals)
```